

Novel Microfluidic Platforms
Incorporating Photonic Ring Resonator Sensors

Innovatieve microfluidische platformen
gebaseerd op fotonische ringresonatorsensoren

Cristina Lerma Arce

Promotoren: prof. dr. ir. P. Bienstman, prof. dr. ir. J. Lammertyn
Proefschrift ingediend tot het behalen van de graad van
Doctor in de Ingenieurswetenschappen: Fotonica

Vakgroep Informatietechnologie
Voorzitter: prof. dr. ir. D. De Zutter
Faculteit Ingenieurswetenschappen en Architectuur
Academiejaar 2013 - 2014



ISBN 978-90-8578-659-7
NUR 954
Wettelijk depot: D/2014/10.500/5

Table of Contents

Acknowledgements	i
Nederlandse samenvatting	xxiii
English summary	xxix
1 Introduction	1
1.1 Labeled biosensing	2
1.2 Label-free biosensing	4
1.3 Lab-on-a-chip	5
1.4 Three novel integrated platforms proposed in this thesis	8
1.5 Thesis outline	10
1.6 Publications	11
References	13
2 Label-free biosensors	17
2.1 Mechanical biosensors	17
2.2 Electrical biosensors	20
2.3 Optical biosensors	21
2.3.1 Surface plasmon resonators	22
2.3.2 Interferometer-based biosensors	24
2.3.3 Photonic crystals	27
2.3.4 Ring resonators	29
2.4 Silicon photonic ring resonators label-free biosensors	30
2.4.1 Lorentzian approximation of resonances	35
2.4.2 Coupling section	35
2.4.3 Silicon ring resonator for biosensing	36
2.4.4 Vernier ring resonators	39
2.5 Conclusions	41
References	42

3	SOI microring resonator sensor integrated on the fiber facet	51
3.1	Optical fiber sensors	52
3.1.1	Fiber Bragg gratings	54
3.1.2	Long-period gratings	58
3.1.3	SPR fiber sensors	58
3.2	Design of the optical circuit to be transferred on the fiber facet . .	60
3.2.1	Grating couplers	60
3.2.2	Sensing circuit	62
3.3	Transfer of the photonic chip to the fiber facet	64
3.3.1	Route 1: failed	64
3.3.2	Route 2: successful	68
3.4	Characterization of the fiber probe sensor	71
3.5	Conclusions	75
	References	76
4	Digital microfluidic platform for photonic biosensors	81
4.1	Digital microfluidics	82
4.1.1	Basic concepts	82
4.1.1.1	Surface tension	82
4.1.1.2	Contact angle	83
4.1.2	Electrowetting principle	85
4.1.3	Electrowetting-on-dielectric	87
4.2	Electrowetting-on dielectric platform for photonic biosensors . .	90
4.2.1	Digital microfluidic system	91
4.3	Photonic biosensors	92
4.4	Integration of both technologies: digital microfluidic platform and photonic biosensors	94
4.5	Experiments	95
4.6	Results	99
4.7	Conclusions	102
	References	103
5	Reaction tubes as a platform for photonic sensors	107
5.1	Motivation	107
5.2	The device: photonic ring resonator sensors integrated at the bot- tom of a reaction tube	110
5.2.1	Photonic chip and reaction tubes	110
5.2.2	Integration	110
5.2.3	Embedded microfluidic system	110
5.2.3.1	Fabrication	110
5.2.3.2	Simulations	113

5.3 Experiments	116
5.3.1 Setup	116
5.3.2 Results	118
5.4 Conclusions	121
References	122
6 Conclusions and Perspectives	123
6.1 Conclusions	123
6.2 Perspectives	125

List of Figures

1	Labelvrije ringresonator biosensor	xxv
2	Integratie van SOI ringresonator sensoren in een digitaal microfluidisch platform	xxvi
3	Proefbuis integratie: schematische weergave van het assemblage toestel en lay-out van de chip	xxvii
1	Ring resonator label-free biosensor	xxx
2	Integration of SOI ring resonator sensors into a digital microfluidic platform	xxxii
3	Reaction tube integration: Schematic of the assembly device and layout of the chip	xxxii
1.1	Labeled biosensing principle	3
1.2	Reaction tube and microtiter plate where label assays such as ELISA are performed	4
1.3	Label-free biosensing principle	5
1.4	Flow cell used in a lab-on-a-chip device	6
1.5	Parabolic velocity profile of the laminar flow in a microchannel	7
2.1	Illustration of two classes of mechanical biosensors	19
2.2	An electrical biosensor based on a MOSFET with silicon nanowire	21
2.3	Working principle of a surface plasmon resonance (SPR) based sensor with coupling prism	23
2.4	Working principle of a Mach-Zehnder interferometer (MZI)	25
2.5	Representation of a spectral shift in an MZI	26
2.6	Periodicity of photonic crystals	27
2.7	Defect photonic crystal	28
2.8	All-pass ring resonator	31
2.9	Transmission spectrum of an all-pass ring resonator	32
2.10	Channel-drop ring resonator	33
2.11	Transmission spectrum of a channel-drop ring resonator	34
2.12	Directional coupler	36

2.13	Ring resonator label-free biosensor	37
2.14	Silicon-on-insulator (SOI) platform	38
2.15	Evanescent field of the quasi-TE mode of a silicon wire waveguide	39
2.16	Vernier effect ring resonators and their theoretical wavelength spectrum	40
3.1	Light propagation in optical fibers	53
3.2	Fiber Bragg Grating (FBG) fabrication methods	55
3.3	Photonic Crystal Fibers (PCF)	56
3.4	Fiber Fabry-Perot cavities	57
3.5	Coupled fibers as fiber-based biochemical sensor platform	59
3.6	SPR fiber sensor	59
3.7	Grating couplers couple the light from the fiber to the photonic circuit	61
3.8	Schematic of the top view of the optical fiber probe with the photonic circuit aligned to the core of the fiber	63
3.9	Microscope picture of the fiber probe facet with the photonic circuit aligned to the core of the fiber	64
3.10	Fabrication process: Route 1	65
3.11	Grating couplers membrane suspended in air and later collapsed on the silicon substrate	67
3.12	Bad detachment of the photonic circuit membrane after collapse	68
3.13	Fabrication process: Route 2	69
3.14	Mask geometry of the surroundings of the optical circuit	72
3.15	Read-out employed to characterize the fiber probe	73
3.16	Fiber sensor resonance	74
3.17	Measured resonance wavelength shift due to the change in refractive index of various aqueous solutions	75
4.1	Molecular representation of surface tension	83
4.2	Hydrophilic vs. hydrophobic surfaces	84
4.3	Hysteresis contact angle	85
4.4	Electrowetting mechanism	85
4.5	Electrowetting (EW) and electrowetting-on-dielectric (EWOD)	87
4.6	Cross-section of a typical EWOD platform	88
4.7	Cross-section of an electrowetting-on-dielectric (EWOD) lab-on-a-chip and the electrowetting principle	91
4.8	Photograph of the digital microfluidic chip	91
4.9	Droplet movement controlled along a pattern of electrodes	92
4.10	Chip layout top view	93

4.11	Integration of SOI ring resonator sensors into a digital microfluidic platform	94
4.12	Alignment of the electrodes chip and the SOI chip	95
4.13	IR camera image of the SOI chip placed up-side down	97
4.14	Measurement process to characterize the photonic sensors in the digital microfluidic platform	98
4.15	Teflon pattern on the SOI chip	99
4.16	Evolution in time of the resonance wavelength shift of the ring resonators during the measurements of different sodium chloride concentrations	100
4.17	Resonance wavelength shift of the ring resonators due to the change in refractive index of various aqueous solutions	101
5.1	Microtest tube introduced in laboratories by Eppendorf in 1963	108
5.2	Mobidiag assay principle	108
5.3	The Corning Epic System based on waveguide grating optical biosensors at the bottom of a microtiter plate	109
5.4	The photonic chip is attached at the bottom of the reaction tube using a UV curable adhesive	111
5.5	Schematic of the assembled device and layout of the chip	111
5.6	Microscope image of part of a silicon ring resonator where the silicon substrate is locally etched away	112
5.7	Microscope picture of laser perforations with residues	112
5.8	Microscope picture of the perforation configuration	113
5.9	Simulation of a water-based fluid flow in our device configuration	115
5.10	Simulation detail of one of the apertures	115
5.11	Pressure setup used to characterize the reaction tube device	116
5.12	Device mounted on a vacuum chuck with an additional pump to move the fluid across the chip surface	117
5.13	Device mounted on a vacuum chuck, while measurements are being performed from the bottom of the chip	117
5.14	Evolution in time of the resonance wavelength shift of the ring resonators during the measurements of different sodium chloride concentrations	119
5.15	Resonance wavelength shift of the ring resonators in the different steps of the bioassay	120

List of Tables

4.1 Different concentrations and refractive indices of the droplets used in the experiments	96
--	----

List of Acronyms

A

AC Alternating Current

B

BCB Benzocyclobutene
BOX Buried oxide
BSA Bovine Serum Albumin

C

CNT Carbon NanoTubes
CMOS Complementary Metal Oxide Semiconductor
CMP Chemical Mechanical Polishing
CCD Coupled Charge Device

D

DC Direct Current
DAQ Data acquisition
DI Deionised
DNA Deoxyribonucleic acid

E

ELISA	Enzyme-linked immunosorbent assay
EM	Electro Magnetic

F

FDTD	Finite Difference Time Domain
FBG	Fiber Bragg Grating
FOM	Figure of Merit
FSR	Free spectral range
FWHM	Full Width at Half Maximum

H

HF	Hydrofluoric acid
HIV	Human Immunodeficiency Virus

I

IC	Integrated Circuit
IPA	Isopropyl alcohol, Isopropanol
ISFET	Ion-sensitive field-effect transistor

K

KOH	Potassium hydroxide
-----	---------------------

L

LED	Light emitting diode
LOD	Limit of Detection
LPCVD	Low-Pressure Chemical Vapour Deposition
LPG	Long-Period Grating

M

MOSFET	Metal-oxide-semiconductor field-effect transistor
MZI	Mach-Zehnder Interferometer

N

NI	National Instruments
----	----------------------

P

PBS	Phosphate Buffered Saline
PCF	Photonic Crystal Fiber
PhC	Photonic Crystal
PIC	Photonic Integrated Circuit
PECVD	Plasma-Enhanced Chemical Vapour Deposition

Q

QCM	Quartz Crystal Microbalance
-----	-----------------------------

R

RI	Refractive Index
RIU	Refractive Index Unit

S

SAW	Surface acoustic wave
SEM	Scanning Electron Microscope
SiNW	Silicon nanowire
SLED	Superluminescent LED
SMF	Single Mode Fibre
SNR	Signal-to-noise ratio
SOI	Silicon-On-Insulator
SP	Signal processing
SPR	Surface plasmon resonance
SPW	Surface plasmon wave

T

TE	Transverse Electric
TM	Transverse Magnetic

U

UV	Ultraviolet
----	-------------

Y

YI	Young Interferometer
----	----------------------

Nederlandse samenvatting

–Summary in Dutch–

Tegenwoordig speelt biosensortechnologie een belangrijke rol bij de diagnose van ziekten zoals kanker. Dit impliceert een technologische uitdaging voor de biosensortechnologieplatformen die naast het aanbieden van uitstekende prestaties op het vlak van multiplexing tegelijkertijd moeten voldoen aan andere eisen, zoals lage productiekosten, gebruiksvriendelijkheid en een draagbaarheid.

Labelvrije biosensing is een methode die gemultiplexte real-time controle van de interactie tussen moleculen toelaat en daarbij kwantitatieve informatie over de concentratie, affiniteit en bindingskinetiek verstrekt. Bovendien is bijna geen staalvoorbereiding vereist, wat het bio-assay vereenvoudigt en kosten en tijd reduceert. In labelvrije biosensoren worden receptormoleculen rechtstreeks geïmmobiliseerd op het sensoroppervlak. De detectie is gebaseerd op de affiniteitsinteractie van de analyetmoleculen zonder de behoefte aan extra labels of extra stappen in het detectieproces. Dit soort sensoren kan onder meer elektrisch, mechanisch of fotonisch zijn. In dit werk zullen we ons richten op fotonische sensoren.

Fotonische geïntegreerde circuits bestaan uit optische bouwblokken zoals laserbronnen, filters en detectoren die geminiaturiseerd zijn tot een micro- of nanoschaal en met mekaar worden verbonden worden op chips. Bovendien kunnen ze zonder extra ontwikkelingskosten voor apparatuur gefabriceerd worden, gezien ze gebruik maken van mature CMOS technologie. Dit laat massaproductie toe wat dan weer de wegwerpbaarheid van sensoren verhoogt: een voorwaarde voor point-of-care diagnostiek. Onder de verschillende fotonische sensoren, vallen ringresonatoren op als voornaamste kandidaten om een hoge performantie te bereiken. Daarenboven beschikken ze over het potentieel om in zeer dichte arrays voor gemultiplexte analyse te worden ingezet.

Een ringresonator bestaat enerzijds uit een gesloten golfgeleiderlus, die circulerende resonantiemodes ondersteunt, en anderzijds uit een koppelingsmechanisme dat toegang verschaft tot deze lus. Een labelvrije biosensor is in staat om interacties tussen analyetmoleculen en geïmmobiliseerde receptormolecu-

len op zijn oppervlak te meten (Figuur 1). Een meetbare verandering in de resonantiegolflengte wordt geïnduceerd wanneer moleculaire bindingen optreden op het oppervlak. Deze verandering kan continu gemeten worden wat kwantitatieve gegevens over de concentratie van het analiet, de affiniteit tussen moleculen en de kinetiek van de moleculaire reacties oplevert.

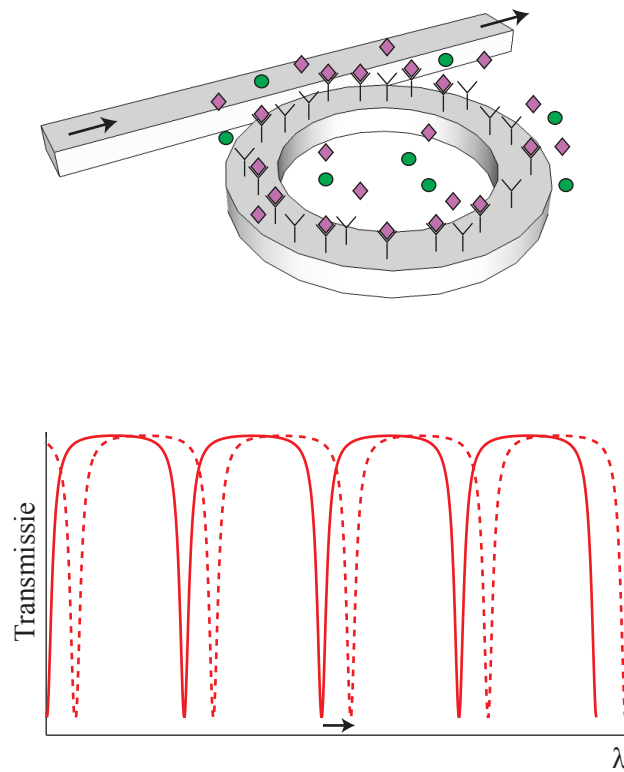
Dit is dan ook de transducer die we in dit doctoraatswerk zullen gebruiken.

Twee belangrijke factoren die biosensortechnologie aan de bovengenoemde eisen helpen te voldoen zijn integratie en miniaturisatie. De zogenaamde 'lab-on-a-chip' toestellen integreren de transducer, in ons geval ringresonatoren, in een gebruiksvriendelijk platform waar de toelevering van het staal aan het oppervlak van de sensor op een zeer efficiënte en vrijwel geautomatiseerde manier plaats vindt. Hierdoor is de behoefte aan vaak dure laboratoriumapparatuur die eenvoudige staalvoorbereidingen uitvoert verminderd. Behoeft aan een kleinere hoeveelheid staal, verminderd reagensverbruik en verminderde analysetijd zijn extra voordelen van deze geminiaturiseerde toestellen die, normaal gezien, een lage productiekost en een draagbaar formaat met zich meebrengen.

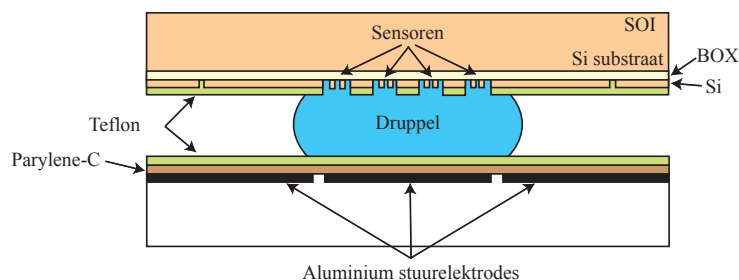
Het doel van dit werk is om drie lab-on-a-chip platformen voor te stellen waarbij de transducer een fotonische ringresonator sensor is.

Voor toepassingen die metingen op moeilijk bereikbare, afgelegen plaatsen vereisen, is een analoog concept aan lab-on-a-chip geïntroduceerd: lab-on-fiber. Glasvezeltechnologie vormt een waardevol platform dat de implementatie van complexe multifunctionele sensorsystemen met voordelen als miniaturisatie, laag gewicht, kosteneffectiviteit, robuustheid, draagbaarheid, flexibiliteit en een laag stroomverbruik kan aanbieden. Wij maken gebruik van dit platform om een ringresonator sensor te integreren op het facet van een single mode glasvezel. In deze implementatie wordt de fotonische geïntegreerde schakeling losgemaakt van het substraat van een Silicon-on-Insulator (SOI) chip en overgedragen op het facet van de vezel. Na fabricage karakteriseren we de component door middel van bulk-sensing experimenten. Hierbij nemen we een zelfde performantie waar als bij eenzelfde sensor op een SOI chip, weliswaar niet geïntegreerd op het vezelfacet.

Er wordt veel aandacht besteed aan lab-on-a-chip toestellen die gebruik maken van kleine en makkelijk te gebruiken cartridges. Nieuwe opkomende microfluidische technologieën worden ontwikkeld en concurreren met de gevestigde microkanaaltechnologie. Dit is ook het geval voor digitale microfluidica die in staat is om alle vloeibare lab-on-chip bewerkingen (doseren, transport, mengen, splitsen, samenvoegen, opslaan) van micro-druppeltjes in een enkel platform, zonder verontreiniging, uit te voeren. We presenteren een tweede platform dat deze veelbelovende technologie combineert met de reeds besproken labelvrije SOI ringresonator sensoren en bieden daarbij een alternatief voor de, over het algemeen, duurdere en ingewikkeldere sensoren die gebaseerd zijn



Figuur 1: Een labelvrije ringresonator biosensor met selectieve affiniteitsinteracties tussen analietmoleculen en geïmmobiliseerde receptormoleculen op het oppervlak van de ring. Een meetbare verandering in de resonantiegolflengte wordt geïnduceerd wanneer moleculaire bindingen optreden op zijn oppervlak. Deze verandering kan continu gemeten worden wat kwantitatieve gegevens over de concentratie van het analiet, de affiniteit tussen moleculen en de kinetiek van de moleculaire reacties oplevert.



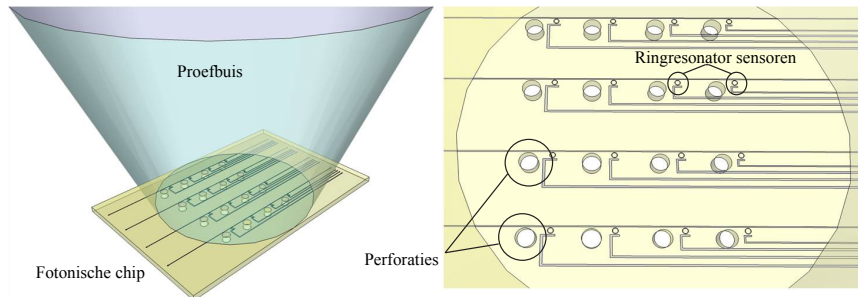
Figuur 2: Incorporatie van de SOI chip met een matrix van microringresonator sensoren in het digitaal microfluidisch systeem door het vervangen van de bovenste glasplaat van het platform.

op microkanalen. In deze implementatie wordt de bovenste glasplaat van een standaard digitaal microfluidisch platform vervangen door de SOI chip met een reeks biosensoren waarbij de bovenkant naar beneden geplaatst wordt (Figuur 2). Omdat ook hier geen fysieke verbinding nodig is tussen de optische chips, de lichtbron en de detectie-eenheid, levert dit alternatief een plug-en-play gebruiksgemak, dat ideaal is voor eenvoudig en snel gebruik in een laboratorium.

We bewijzen de uitstekende prestaties en de compatibiliteit van dit gecombineerde systeem door aan te tonen dat er geen degradatie van de prestaties van de sensor optreedt ten opzichte van simulaties of eerdere metingen van dezelfde sensoren met een typisch, complexer microfluidisch systeem. Deze combinatie zorgt voor een gemultiplexte real-time detectie en analyse.

Een laatste platform bestaat uit de integratie van ringresonator fotonische sensoren met proefbuizen. Proefbuizen worden in ziekenhuizen en laboratoria gebruikt om gelabelde bioassays uit te voeren. De voorgestelde sensor is echter labelvrij en bovendien compatibel met alle labo-instrumenten die betrekking hebben tot geautomatiseerde staalbehandeling. Op die manier kan men labelvrije bioassays uitvoeren met de hulp van onze ringresonator fotonische sensoren.

We combineren de eenvoud en draagbaarheid van het proefbuisformaat met de prestaties van silicium fotonische ringresonator biosensoren door ze onder te brengen in een toepassing die gebruik maakt van stroming van het te meten staal door de sensor. De kanalen van een ingesloten microfluidisch systeem bestaan uit perforaties van de SOI chip bevestigd aan de bodem van de buis. Dit biedt een alternatief voor de algemeen duurdere en ingewik-



Figuur 3: a) Schematische weergave van het assemblage toestel. De silicon-on-insulator chip wordt aangebracht aan de bodem van een proefbuis. b) Lay-out van de chip. De reeks ringresonator sensoren gaat gepaard met een reeks perforaties ernaast. De stroming in de buis wordt geleid door deze openingen. Het staal dat wordt ingebracht in de buis zal door deze openingen stromen, die werken als uitgangskanalen. De gecreëerde stroom zal het detectieproces versnellen.

keldere microfluidische sensoren gebaseerd op microkanalen (Figuur 3). De wegwerpbaarheid van het gecombineerde toestel wordt versterkt door de massafabricage van SOI chips en de goedkope en gebruiksvriendelijke indeling van proefbuizen die elke dag gebruikt worden in laboratoria en ziekenhuizen: twee factoren die het gebruik ervan ten goede komen voor het uitvoeren van labelvrije bioassays. Uit bulk sensing experimenten blijkt dat deze sensoren even goed presteren als sensoren in een conventioneel microfluidisch systeem. Daarnaast hebben we de binding van streptavidin aan avidin op het oppervlak van de sensoren aangetoond wat bewijst dat deze toepassing performant is.

English summary

Nowadays, biosensor technology plays an important role during diagnosis of diseases such as cancers. This implies a technological challenge for the biosensor technology platforms which must keep on offering the best multiplexed performance while at the same time meeting other requirements such as low cost, user-friendliness and portable format.

Label-free biosensing is a method that allows for multiplexed real-time monitoring of the interaction between molecules providing quantitative information on the concentration, affinity and binding kinetics. Besides, almost no sample preparation is required which simplifies the assay, thereby reducing costs and time. In label-free biosensors receptor molecules can be directly immobilized on the surface of the sensor and the detection directly responds to the affinity interaction of the analyte molecules without the need for extra labels or steps in the detection process. This kind of sensor can be electric, mechanic or photonic. In this work we will focus on photonic sensors.

Photonic integrated circuits combine and miniaturize optical functions such as laser sources, filters and detectors, on chips that can be fabricated with nanoscale features and with no extra equipment development cost since they use CMOS processing technology. This allows for mass production, enhancing disposability of devices, which for point-of-care diagnoses is a prior requirement. Among different photonic sensors, ring resonators stand out as prime candidates for achieving high performance and their potential to be produced in highly dense arrays for multiplexed analysis.

A ring resonator consists of a loop, and a coupling mechanism to access this loop, which supports circulating resonant modes. It is a label-free biosensor able to measure interactions between analyte molecules and receptor molecules immobilized on its surface (Figure 1). A measurable shift in the resonance wavelength is induced when molecular binding occurs on its surface. This shift can be continuously monitored over time which gives information on the analyte concentration, affinity between molecules and the kinetics of the biochemical reaction.

This is the transducer that we will use in this PhD work.

Two key factors that help biosensor technology to meet the above men-

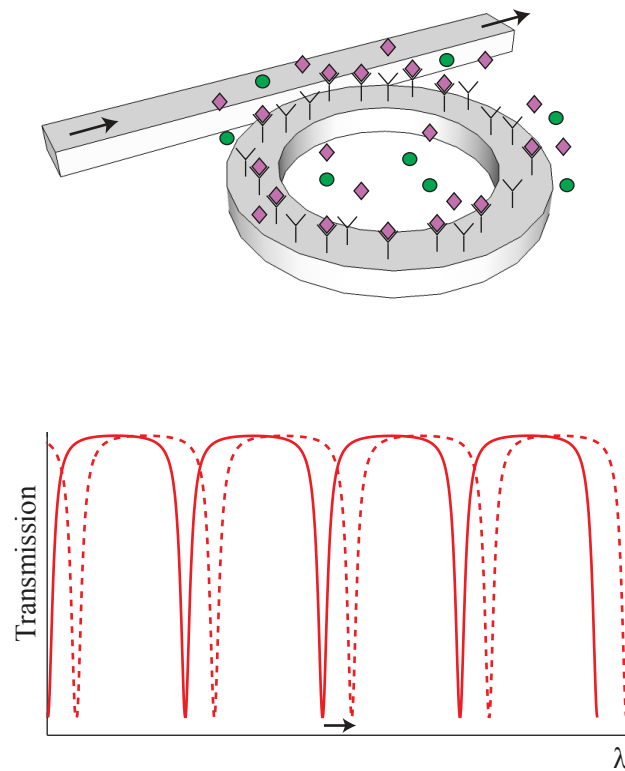


Figure 1: A ring resonator label-free biosensor measures selective affinity interactions between analyte molecules and receptor molecules immobilized on the ring waveguide surface. A measurable shift in the resonance wavelength is induced when molecular binding occurs on its surface. This shift can be continuously monitored over time which gives information on the analyte concentration, affinity between molecules and the kinetics of the biochemical reaction.

tioned requirements are integration and miniaturization. The so-called 'lab-on-a-chip' devices integrate the transducer, in our case ring resonators, in a user-friendly platform where the delivery of the sample to the surface of the sensor is done in a very efficient and almost automated manner that reduces the need for often expensive laboratory equipment that performs simple sample preparation tasks. Smaller sample requirement, reduced reagent consumption and decreased analysis time are extra advantages of these miniaturized devices that are normally low cost and offer a portable format.

The goal of this work is to propose three lab-on-a-chip platforms in which the transducer is the well-known photonic ring resonator sensor.

For those applications which require performing measurements in remote locations that are hard to reach, an analog concept to lab-on-a-chip has been created, lab-on-fiber. Optical fiber technology constitutes a valuable platform that can enable the implementation of complex multifunction sensing systems with all the advantages of miniaturization, light weight, cost-effectiveness, robustness, portability, flexibility and low power consumption. We make use of this platform to integrate a ring resonator sensor on the facet of a single mode optical fiber. In this implementation the integrated photonic circuit is transferred to the facet by detaching it from the substrate of the Silicon-on-Insulator (SOI) chip. After fabrication, we characterize the device by bulk sensing experiments, which show no degradation when comparing to the same sensor on a separate SOI chip, i.e. not integrated on the fiber tip.

A lot of effort is being spent to implement lab-on-a-chip devices in small and easy-to-use cartridges and new emerging microfluidic technologies are being developed and are competing against the well-established microchannel technology. This is the case with digital microfluidics which is able to perform all the fluidic lab-on-a-chip operations (dispensing, transport, mixing, splitting, merging, storing) of micro-sized droplets in a single platform without contamination. We present a second platform which combines this promising technology with the well-known label-free SOI ring resonator sensors, providing an alternative to the typically costly and complex microfluidic system based on microchannels. In this implementation the top glass plate of a basic digital microfluidic platform is replaced by the SOI chip containing the array of biosensors which is placed up-side down (Figure 2). Since no physical connection is needed between the optical chips and the light source and detection unit, this alternative enables plug-and-play ease of use which is ideal for easy and fast use in any laboratory.

We prove the excellent performance and compatibility of this combined system, showing no degradation of the sensor performance with respect to simulations or previous measurements of the same sensors using the typical, more complex microfluidic system. This combination allows for multiplexed real-

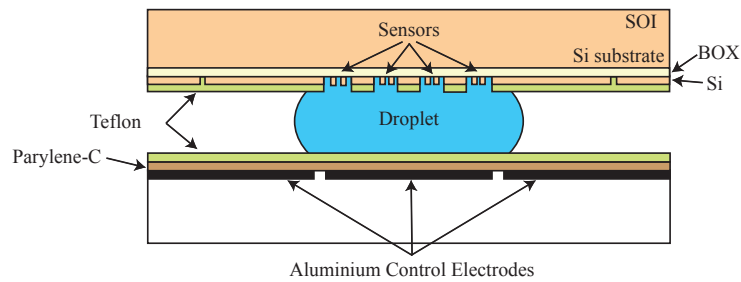


Figure 2: Incorporation of the SOI chip containing an array of microring resonator sensors into the digital microfluidic system by replacing the top glass plate of the platform.

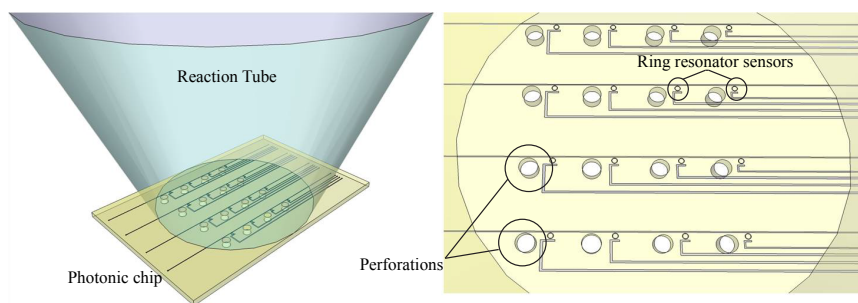


Figure 3: a) Schematic of the assembly device. The silicon-on-insulator chip is incorporated at the bottom of a reaction tube. b) Layout of the chip. The array of ring resonators sensors is accompanied by an array of perforations next to them. The flow within the tube is guided through these apertures. The solution inserted in the tube will flow through these openings which work as exit channels, creating the flow which will accelerate the detection process.

time detection and analysis.

A final platform is presented as the integration of ring resonators photonic sensors with reaction tubes. Reaction tubes are commonly used in hospitals and labs to perform labeled bioassays. However, we propose this platform which is compatible with all lab instrumentation related to automated sample-liquid handling, to perform label-free bioassays with the help of our ring resonator photonic sensors.

We combine the simplicity and portability of the reaction tube format with the performance and throughput of silicon photonic ring resonator biosensors by embodying them in a single flow-through device. An embedded microfluidic system based on perforations of the SOI chip attached to the tube provides an alternative to the typically costly and complex microfluidic system based on microchannels (Figure 3). The disposability of the combined device is enhanced by the mass fabrication of SOI chips and the cheap and user friendly format of reaction tubes which are used every day in labs and hospitals, two factors that benefit their use for performing label-free bioassays. We demonstrate by bulk sensing experiments that the sensors suffer no degradation when being integrated in the reaction tube as well as the good performance of the device by showing the binding of streptavidin to avidin on the surface of the sensors.

1

Introduction

Nowadays there are many diseases where technology can play an important role during diagnosis. Cancers, e.g., arise as a result of the disruption of normal cell signaling pathways, which produce cancer cells to exhibit a decisive growth advantage compared to their neighbors. Unfortunately today it is still very challenging to explore their causes and to develop methods for early diagnosis and treatment. The common method for cancer diagnosis and prognosis still relies heavily on technologies that are over 100 years old (visual inspection of cell morphology by a pathologist).

Proteomics, the large-scale study of proteins, attempts to overcome this limitation by studying altered protein expressions in tissue or bodily fluids. Of special interest is the direct analysis of proteins in blood serum (the liquid portion of blood without clotting factors), since it is an easy accessible liquid that contains a variety of proteins released by diseased tissue. However this analysis is not straightforward and there exists a need for a new biosensing technology able to provide data of many different proteins concentrations that can be affected by a disease [1].

New biosensor technology platforms must then meet certain requirements. First, they should be multiplexed, i.e. many molecular interactions should be monitored in the same sample at the same time. Another important requirement is an exceptional limit of detection (LOD) which refers to the minimum detectable concentration or mass amount of an analyte in a sample. New tech-

nology must be able to detect very low concentrations of proteins while rejecting other proteins present in high concentrations that are not of interest. This demands excellent sensitivity and selectivity. Other requirements for the biosensor technology are short time to analyze samples, little sample preparation, user-friendly format, portability, low-cost, quantitative measurements and high throughput.

There are different ways of doing biosensing [2–5] and they fall into two classes: labeled and label-free biosensing. In the following sections, we will review the basic principle of both methods. Then we will introduce the concept of a lab-on-a-chip device, discussing the most established integration platforms. Finally, we will propose three new different lab-on-a-chip formats which will be investigated in the course of this thesis.

1.1 Labeled biosensing

The most popular labeled assay today is known as *enzyme-linked immunosorbent assay* (ELISA) [5]. It is e.g. today's primary test for diagnostics of a human immunodeficiency virus (HIV) infection [6]. It is based on the indirect detection of an analyte by attaching an easy-to-measure label to it, such as a fluorescent dye or an enzyme that produces a visible signal. The process is illustrated in Figure 1.1. First, the target molecules (i.e. analyte) in a fluidic sample are immobilized on a substrate, either via non-specific adsorption (indirect ELISA) or via specific binding to previously immobilized antibodies (sandwich ELISA) [7]. In a second step, a detection antibody specific to the antigen is added, which binds to the immobilized antigens. The last is either directly linked to an enzymatic label or recognized by an extra non-specific label antibody. In between the different steps the surface needs to be washed with detergent solution to remove non-specifically bound molecules. Finally, an enzymatic substrate is added that reacts with the enzymatic labels and produces a visible signal indicating the presence and quantity of the antigen in the sample.

In practice, labeled assays such as ELISA take place in reaction tubes or microtiter plates [8] (see Figure 1.2). The change in color of a positive assay result can be measured qualitatively without read-out equipment (naked-eye), or quantitatively by measuring the optical transmission using a camera or an optical power meter.

While ELISA only allows measuring a single protein in each sample, there exist other labeled techniques that allow for multiplexed measurements. This is the case of protein microarrays which allow measurements to be performed on a massively parallel scale. It is a technique very similar to standard ELISA immunoassays, but in this case different receptors antibodies are immobilized at spatially defined locations that subsequently allow for deconvolution of the

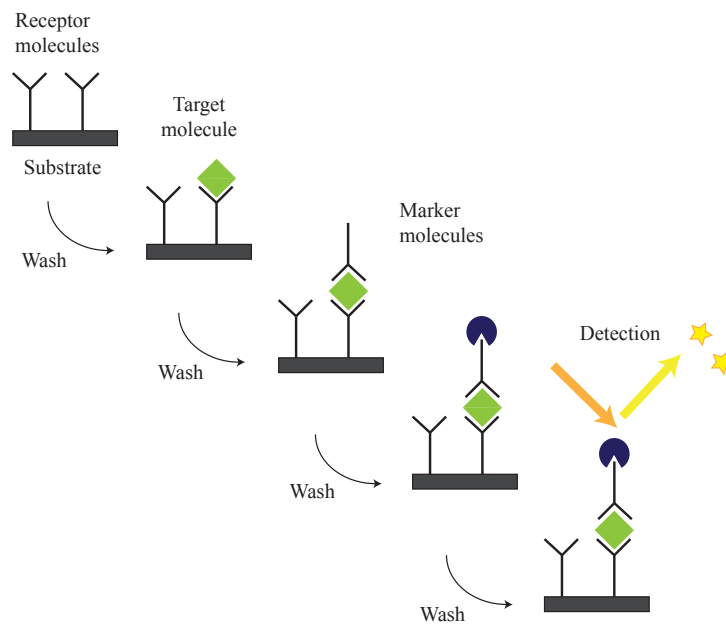


Figure 1.1: The target molecules bind to previous immobilized antibodies on a substrate. After that, marker molecules bind to another site of the target molecules. The marker molecules are normally activated by adding an enzymatic substrate that produces a visible signal indicating presence and quantity of the antigen in the sample. In-between different steps, the surface needs to be washed with a detergent solution to remove non-specifically bound molecules.

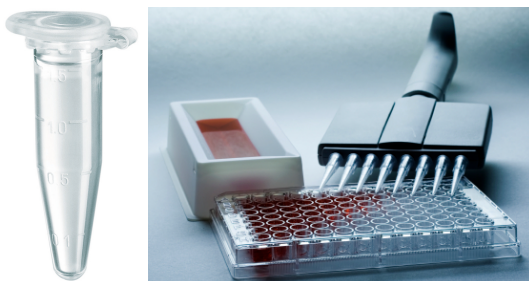


Figure 1.2: Reaction tube and microtiter plate where label assays such as ELISA are performed.

multiplexed measurements, such that the detection of different proteins can be monitored in the same well [7].

1.2 Label-free biosensing

While labeled detection methods can be sensitive down to a single molecule [9], they have some disadvantages. First, the labeling process is labour-intensive and costly. Markers sometimes don't bind directly to the target molecule so an intermediary molecule is required [10]. Second, labels can structurally and functionally alter the assay. Often they degrade over time, which can reduce the efficiency of the assay. Third, the required washing between the different steps of the assay increases the sample preparation, it is time consuming, and can reduce the effective throughput. Lastly, these assays can only be performed in an 'end-point' fashion, i.e. the signal is only interrogated after the complete assay is finished. This doesn't allow for continuous, real-time monitoring of molecular interactions so that no kinetic information (i.e. binding of target to receptor molecules as a function of time) can be obtained. Instead, quantification is difficult since it is not possible to determine precisely the amount of markers that bind to the target molecules.

In contrast, in label-free detection, target molecules are not labeled or altered, and are detected in their natural forms which makes the detection relatively easy and cheap to perform. Label-free detection involves a transducer that directly measures some physical property (e.g. electrical, mechanical or optical) of the biological compound. A receptor molecule is attached to the surface of the sensor, which responds to the affinity interaction of the receptor with an analyte (Figure 1.3). The formation of complexes can thus be monitored continuously in real-time allowing for quantitative and kinetic measurement of

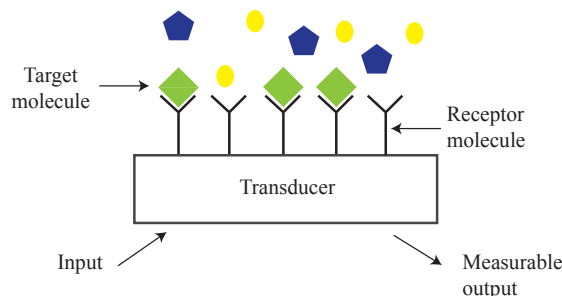


Figure 1.3: A transducer coated with receptor molecules is able to generate a measurable signal of a physical property when target molecules bind to these receptor molecules.

molecular interaction. Additionally a highly multiplexed assay is easy to perform by measuring multiple transducers with different receptor molecules on the same substrate [11]. Sample preparation is almost not required which decreases costs and enhances the throughput. In the rest of this work, we will only consider label-free biosensors. An overview of the state of the art of label-free biosensors will be given in Chapter 2.

1.3 Lab-on-a-chip

Lab-on-a-chip is not a well-defined scientific term, since many disciplines in the life sciences approach the term with different meanings. In particular for our case, a lab-on-a-chip device consists of the integration of a transducer, which will act as a sensor, and a microfluidic component, which will deliver the analyte to the sensor [12]. The concept appears in order to reduce costs, time and increase portability.

Lab-on-a-chip devices reduce the need for often expensive laboratory equipment that performs simple sample preparation tasks. These operations, such as mixing, dispensing, separation, can all be incorporated on a single chip. Miniaturization is the key feature of lab-on-a-chip devices since it brings numerous advantages such as smaller sample requirement, reduced reagent consumption and decreased analysis time. Furthermore, because space is used sparingly, massive parallelization can be accomplished, increasing levels of throughput.

The current most popular technology for the fabrication of the microfluidic component of such devices is based on the soft lithography of poly-di-

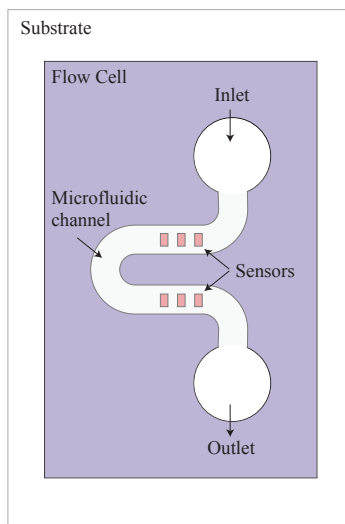


Figure 1.4: A fluidic compartment (flow cell) which has microchannels defined in one of its surfaces, is attached to a substrate where it brings the sample with target molecules in contact with the chemically functionalized biosensors.

methyl siloxane (PDMS). This material is a transparent, biocompatible elastomer which, through simple molding procedures, can be made into microfluidic devices. Normally this microfluidic compartment (also commonly known as flow cell) which has small microchannels defined in one of its surfaces, is glued onto the surface sensor [13] (see Figure 1.4) and the analyte is flown over the coated sensor surface, bringing the target molecules in close contact with the receptor molecules.

In microwell-plate-based methods biomolecules reach the surface of interest (the surface where the receptor molecules are bound) by pure diffusion: due to thermally-induced random motion of particles, such as Brownian motion [14], biomolecules diffuse towards the sensor surface where they bind to the receptor molecules. The time that a molecule takes to diffuse towards the sensor increases when an initial amount of molecules has already bound to the sensor [15], which means that the process gets slower over time.

However, in the well-established microchannel technology the time needed to bring the analyte in contact with the sensor is significantly reduced by the miniaturization of the system. The compressed size of the microchannels reduces the influence of the inertial forces compared to frictional forces, leading to the formation of laminar flow. In this case and depending on the flow rate, the

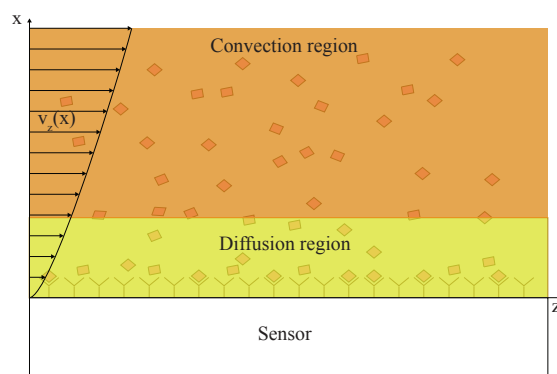


Figure 1.5: The laminar flow developed between two parallel plates has a parabolic velocity profile. This implies that the velocity near the sensor surface is very small, compared to its maximum in the centre of the channel. A diffusion-dominated region develops near the sensor surface and a much larger, convection region dominates the rest of the channel.

delivery of new target molecules can counteract the slow diffusive effect, which has a direct influence on the characteristic times of the system.

Nevertheless there are also drawbacks to this technology. In a fully-developed laminar flow in a channel consisting of two parallel plates, the velocity profile is parabolic, which means that the fluid speed near the walls is much smaller than in the center of the channel. In the center of the channel, the flow velocity is high enough to counter the diffusion effect, so convection will be the dominant effect, whereas near the channel walls diffusion will remain the dominant effect (see Figure 1.5). A permanent diffusion zone directly above the sensor will always remain, even when increasing the flow rate significantly [15]. Furthermore, laminar flows only produce relatively slow diffusive mixing, which can be a major limitation for some applications requiring fast homogenization of flow. In addition, the small reagent consumption theoretically reachable in microfluidic devices is generally not reached due to a current lack of methods for fluid handling.

PDMS -the material most commonly used in academic studies of microfluidics- offers an excellent optical transparency and a flexible platform with which new concepts can be tested. However it has an affinity for small hydrophobic molecules and thus could lead to biomolecule absorption/adsorption from the medium, which can bias the experimental conditions. The permeability of

PDMS to water vapor can also lead to media drying and concentration changes. The use of rigid material like silicon, glass or steel [16, 17], may solve these problems and allow reactions at high temperatures and pressures, but the fabrication of devices with any of these materials is more difficult than with PDMS. Pumping and valving in rigid materials such as steel must be accomplished using entirely different strategies from those used in PDMS. Other materials like Mylar, polycarbonate, polymethyl-methacrylate (PMMA) and polyolefin have been also studied [18]. Some of them offer a less time-consuming fabrication process than the casting of PDMS. It is the case of Mylar or PMMA which can be fabricated using a direct-write CO₂ laser system [19].

1.4 Three novel integrated platforms proposed in this thesis

While a lot of effort has been spent to implement such lab-on-a-chip devices in small and easy-to-use cartridges, there exist many applications that require performing measurements in remote locations that are hard to reach. For these cases a new concept has been created, Lab-on-fiber. Optical fiber technology constitutes a valuable platform that can enable the implementation of complex multifunction sensing systems with all the advantages of miniaturization, lightweight, cost-effectiveness, robustness, portability, flexibility and low power consumption. In the last decade, many research groups have focused their efforts on the design and the development of all-fiber integrated devices based on fiber Bragg gratings (FBG), long-period gratings (LPG), surface plasmon resonance (SPR) and other configurations [20–23]. In Chapter 3 we will elaborate on the fabrication of a novel special Lab-on-fiber device which consists of the integration of an optical transducer, an SOI ring resonator, on the tip of an optical fiber. This work was published in [24]. Posterior to this work a similar approach was performed by Shambat et al. in [25] where a semiconductor photonic crystal membrane was transferred to a fiber facet using a different fabrication process. Another interesting nano-transferring approach was proposed by [26] where in this case patterns of metallic nanostructures were transferred to the tip of an optical fiber.

Despite the previously mentioned drawbacks of the microchannel-based technology, this is the most established microfluidics technology nowadays. However new emerging technologies are gaining traction offering much more versatility. This is the case with digital microfluidics.

Digital microfluidics is similar to microchannel technology in that both can perform lab analyses with much smaller sample volumes than in bench-scale methods, i.e. in the microliter to nanoliter range [27]. While in microchannel

technology it is common to work with continuous flows, digital microfluidics is based on microdroplet manipulation. Microliter- to picoliter-sized droplets are generated, transported, mixed, and split, on reconfigurable paths of buried actuation electrodes with high flexibility without the need for moving parts such as pumps or valves. This avoids cross-contamination between samples or reagents and allows fluid plugs to be manipulated on reconfigurable paths.

Many applications such as DNA extraction and amplification [28], cell-based assays [29, 30], enzymatic assays [31–34] and immunoassays [35] demonstrate that this platform is a successful lab-on-a-chip implementation. Few research results have been reported on the integration of sensing systems with digital microfluidic chips [36, 37]. In Chapter 4 we will investigate how this platform can be part of a robust lab-on-a-chip device, where the integration of this microfluidic system is done together with an array of photonic label-free ring resonator sensors fabricated on an SOI chip. This work was published in [38] and is a result of a collaboration with the MeBioS research group (prof. Lammertyn, KU Leuven) which is experienced in digital microfluidics. Luan et al. [39] have already integrated a microdisk resonator in such platform. However the system relies on very complex fabrication procedures to integrate polymer-based disk resonators, photodetectors and bulky fiber optical connections. In contrast, the integration of both chips presented in this work enables plug-and-play ease of use, and offers other advantages such as portability, flexibility and an excellent performance.

At this point, we have introduced two devices, one based on lab-on-a-chip where digital microfluidics were integrated with photonic sensors in a chip platform, and another one based on a Lab-on-fiber, where a photonic sensor is integrated on an optical fiber platform. In Chapter 5 we introduce another lab-on-a-chip device: the integration of ring resonators photonic sensors with reaction tubes. Millions of them are used every day in labs and hospitals to perform common labeled bioassays. An additional advantage of this platform is its compatibility with all lab instrumentation related to automated sample-liquid handling compatible with the tube format invented by Eppendorf in 1963. An example of this is a platform commercialized by Mobidiag [40] which incorporates a microchip at the bottom of a reaction tube where a microarray is defined. The device is used for labeled biosensing applications. We, however, propose the integration of an SOI chip with an array of ring resonators, which work as label-free biosensors. Furthermore, a second level of integration will be enabled by creating a flow over the sensors' surface, i.e. also integrating the microfluidics in the same device.

It is obvious that recent advances in microfabrication have enabled high density, chip-scale integration of optical components with substantial advantages for lab-on-a-chip applications by enabling integration of both fluidic han-

dling and optical analysis onto a single chip. These types of integrated sensing devices have the potential to enable creation of biosensors that can provide rapid, sensitive, and multiplexed measurements in point-of-care diagnostic applications.

1.5 Thesis outline

In Chapter 2 we will give a state-of-the-art overview of available label-free biosensors where we will focus on photonic sensors. An extensive overview over ring resonator sensors, their advantages, drawbacks and their applications will be provided since this is the sensor we will base the research of this PhD work on. The impact of optical fiber technology in biosensors will be explained in Chapter 3 where we will give a short overview of the most relevant label-free optical fiber sensor technologies. Here we will introduce our first novel integration: we will describe the design, fabrication and characterization of a ring resonator-based optical fiber sensor developed in the course of this PhD work. We pretend to provide with a flexible and portable biosensor device able to measure in remote locations with the high quality of a ring resonator sensor. To verify the capability of this Lab-on-fiber device, proof-of-principle experiments are presented and discussed. Chapter 4 will study the possibility of integrating a digital microfluidic platform with an SOI ring resonator sensor platform. The advantages of this new trend in microfluidics overcome many limitations of the most established technology based on microchannels. Proof-of-principle experiments are presented and discussed, with the objective of paving a way for a novel integrated platform in diagnostics. Another lab-on-a-chip device will be introduced in Chapter 5 where the reaction tube will be used as a platform. The integration of this disposable and compatible platform with SOI ring resonator sensors offers label-free biosensing advantages in a historically labeled platform. In this chapter we discuss the advantages of the device, describe the integration, and show the results of proof-of-principle experiments. The impact of this device could imply a big development in diagnostics. Conclusions of the work in this PhD and perspectives are finally given in Chapter 6.

1.6 Publications

Patent applications

1. P. Bienstman, C. Lerma Arce and E. Hallynck. *Biosensing device*. US Provisional.

Publications in international journals

1. C. Lerma Arce, S. Van Put, A. Goes, E. Hallynck, P. Dubruel, K. Komorowska and P. Bienstman. *Reaction tubes: a new platform for silicon nanophotonic ring resonator sensors*. Journal of Applied Physics, (accepted).
2. C. Lerma Arce, D. Witters, R. Puers, J. Lammertyn and P. Bienstman. *Silicon Photonic Sensors incorporated in a Digital Microfluidic System*. Analytical and Bioanalytical Chemistry, 404(10):2887–2894, 2012.
3. C. Lerma Arce, K. De Vos, T. Claes, K. Komorowska, D. Van Thourhout and P. Bienstman. *Silicon-on-insulator microring resonator sensor integrated on an optical fiber facet*. IEEE Photonics Technology Letters, 23(13):890–892, 2011.

Publications in magazines

1. C. Lerma Arce, A. Goes, E. Hallynck, P. Dubruel, K. Komorowska, S. Van Put and P. Bienstman. *Reaktionsgefäße als neue Plattform für Sensoren mit nanophotonischen Silizium-Ringresonatoren*. BioPhotonik 6(2):40–42, 2013.

Book chapters

1. C. Lerma Arce, K. De Vos, T. Claes, K. Komorowska and P. Bienstman. *SOI microring resonator sensor integrated on the fiber facet*. Lab on Fiber Technology. Springer-Verlag Berlin Heidelberg New York. Editors: A. Cusano, M. Consales, A. Crescitelli, A. Ricciardi.

Publications in international conferences

1. P. Bienstman, S. Werquin, C. Lerma Arce, D. Witters, R. Puers, J. Lammertyn, T. Claes, E. Hallynck, J.-W. Hoste and D. Martens. *Silicon Nanophotonics On-chip Sensing (invited)*. PIERS 2013, to be published, Stockholm, Sweden, August 2013.

2. C. Lerma Arce, A. Goes, E. Hallynck, P. Dubruel, K. Komorowska, S. Van Put and P. Bienstman. *Reaction tubes as a platform for silicon nanophotonic ring resonator biosensors*. Integrated Photonics Research, Silicon and Nano-Photonics (IPR) OSA 2013, Rio Grande, Puerto Rico, July 2013.
3. P. Bienstman, S. Werquin, C. Lerma Arce, D. Witters, R. Puers, J. Lammertyn, T. Claes, E. Hallynck, J.-W. Hoste and D. Martens. *Nanophotonic biosensors in silicon-on-insulator (invited)*. Transducers 2013, Barcelona, Spain, June 2013.
4. C. Lerma Arce, A. Goes, E. Hallynck, P. Dubruel, K. Komorowska, S. Van Put and P. Bienstman. *Silicon nanophotonic ring resonator sensors integrated in reaction tubes*. Photonics West, 859801, San Francisco, CA, USA, February 2013.
5. P. Bienstman, S. Werquin, C. Lerma Arce, D. Witters, R. Puers, J. Lammertyn, T. Claes, E. Hallynck, J. W. Hoste and D. Martens. *Ring resonator based SOI biosensors*. Photonics West, 862905, San Francisco, CA, USA, February 2013.
6. C. Lerma Arce, D. Witters, R. Puers, J. Lammertyn and P. Bienstman. *The use of digital microfluidics for a silicon photonic sensors platform*. Annual Symposium IEEE Photonics Society Belenux Chapter, Mons, Belgium, November 2012.
7. C. Lerma Arce, T. Claes, K. Komorowska and P. Bienstman. *Silicon nanophotonic sensors integrated in reaction tubes XI Conference on Optical Chemical Sensors and Biosensors EUROPT(R)ODE XI, Barcelona, Spain, April 2012*.
8. C. Lerma Arce, D. Witters, J. Lammertyn and P. Bienstman. *Silicon nanophotonic sensors incorporated in a digital microfluidic system*. XI Conference on Optical Chemical Sensors and Biosensors EUROPT(R)ODE XI, Barcelona, Spain, April 2012.
9. P. Bienstman, T. Claes, C. Lerma Arce, W. Bogaerts, K. Komorowska and D. Van Thourhout. *Novel Ring Resonator Based Biosensors*. CLEO Europe (invited), Munich, Germany, May 2011.
10. C. Lerma Arce, K. Komorowska, D. Van Thourhout and P. Bienstman. *Optical fiber probe sensor based on Silicon-on-Insulator ring resonator*. Annual Symposium IEEE Photonics Benelux, Delft, Netherlands, November 2010.

References

- [1] S. Ray, P. J. Reddy, R. Jain, K. Gollapalli, A. Moiyadi, and S. Srivastava. *Proteomic technologies for the identification of disease biomarkers in serum: advances and challenges ahead*. *Proteomics*, 11(11):2139–61, June 2011.
- [2] X. Fan, I. M. White, S. I. Shopova, H. Zhu, J. D. Suter, Y. Sun, and J. D. Suter. *Sensitive optical biosensors for unlabeled targets: a review*. *Analytica Chimica Acta*, 620(1-2):8–26, July 2008.
- [3] K. Länge, B. E. Rapp, and M. Rapp. *Surface acoustic wave biosensors: a review*. *Analytical and Bioanalytical Chemistry*, 391(5):1509–1519, July 2008.
- [4] M. A. Cooper. *Optical biosensors in drug discovery*. *Nature Reviews: Drug Discovery*, 1(7):515–528, July 2002.
- [5] R. M. Lequin. *Enzyme immunoassay (EIA)/Enzyme-linked immunosorbent assay (ELISA)*. *Clinical Chemistry*, 51(12):2415–2418, December 2005.
- [6] E. Mylonakis, M. Paliou, M. Lally, T. P. Flanigan, and J. D. Rich. *Laboratory testing for infection with the human immunodeficiency virus: established and novel approaches*. *The American Journal of Medicine*, 109(7):568–576, November 2000.
- [7] U. B. Nielsen and B. H. Geierstanger. *Multiplexed sandwich assays in microarray format*. *Journal of Immunological Methods*, 290(1-2):107–120, July 2004.
- [8] V. Spiehler, D. S. Isenschmid, P. Matthews, P. Kemp, and T. Kupiec. *Performance of a microtiter plate ELISA for screening of postmortem blood for cocaine and metabolites*. *Journal of Analytical Toxicology*, 27:587–591, 2003.
- [9] S. Schultz, D. R. Smith, J. J. Mock, and D. a. Schultz. *Single-target molecule detection with nonbleaching multicolor optical immunolabels*. *Proceedings of the National Academy of Sciences of the United States of America*, 97(3):996–1001, February 2000.
- [10] M. L. Phelan and S. Nock. *Generation of bioreagents for protein chips*. *Proteomics*, 3:2123–2134, November 2003.
- [11] K. De Vos. *Label-free Silicon Photonics Biosensor Platform with Microring Resonators*. Phd dissertation, Ghent University, Ghent, 2010.
- [12] D. Psaltis, S. R. Quake, and C. Yang. *Developing optofluidic technology through the fusion of microfluidics and optics*. *Nature*, 442(7101):381–386, July 2006.

- [13] Elveflow, <http://www.elveflow.com/microfluidic-reviews-and-tutorials/review-microfluidic-for-cell-biology>.
- [14] H. Bruus. *Theoretical Microfluidics*. Oxford University Press, 2008.
- [15] T. M. Squires, R. J. Messinger, and S. R. Manalis. *Making it stick: convection, reaction and diffusion in surface-based biosensors*. Nature Biotechnology, 26(4):417–426, April 2008.
- [16] L. Löwe and W. Ehrfeld. *State-of-the-art in microreaction technology : concepts , manufacturing and applications*. Electrochimica Acta, 44(21-22):3679–3689, 1999.
- [17] D. Snyder, C. Noti, P. Seeberger, F. Schael, T. Bieber, G. Rimmel, and W. Ehrfeld. *Modular microreaction systems for homogeneously and heterogeneously catalyzed chemical synthesis*. Helvetica Chimica Acta, 88(1):1–9, January 2005.
- [18] G. M. Whitesides. *The origins and the future of microfluidics*. Nature, 442(7101):368–73, July 2006.
- [19] R. Irawan, S. C. Tjin, X. Fang, and C. Y. Fu. *Integration of optical fiber light guide, fluorescence detection system, and multichannel disposable microfluidic chip*. Biomedical Microdevices, 9(3):413–9, June 2007.
- [20] A. Cusano, A. Cutola, and J. Albert, editors. *Fiber Bragg Grating sensors: research advancements, industrial applications and market exploitation*. Bentham Ebooks, 2011.
- [21] L. Rindorf and O. Bang. *Highly sensitive refractometer with a photonic-crystal-fiber long-period grating*. Optics Letters, 33(6):563–5, March 2008.
- [22] B. Spackova and J. Homola. *Theoretical analysis of a fiber optic surface plasmon resonance sensor utilizing a Bragg grating*. Optics Express, 17(25):199–203, 2009.
- [23] J. Pollet, K. P. F. Janssen, K. Knez, and J. Lammertyn. *Real-time monitoring of solid-phase PCR using fiber-optic SPR*. Small (Wiley-VCH), 7(8):1003–6, April 2011.
- [24] C. Lerma Arce, K. De Vos, T. Claes, K. Komorowska, D. V. Thourhout, and P. Bienstman. *Silicon-on-Insulator microring resonator sensor integrated on an optical fiber facet*. IEEE Photonics Technology Letters, 23(13):890–892, 2011.

- [25] G. Shambat, J. Provine, K. Rivoire, T. Sarmiento, J. Harris, and J. Vuckovic. *Optical fiber tips functionalized with semiconductor photonic crystal cavities*. Applied Physics Letters, 99(19):191102, 2011.
- [26] D. J. Lipomi, R. V. Martinez, M. A. Kats, S. H. Kang, P. Kim, and J. Aizenberg. *Patterning the tips of optical fibers with metallic nanostructures using nanoskiving*. Nano Letters, 11(2):632–636, 2011.
- [27] A. R. Wheeler. *Putting Electrowetting to Work*. Science, 322(October):539–540, 2008.
- [28] M. Abdelgawad, S. Freire, H. Yang, and A. R. Wheeler. *All-terrain droplet actuation*. Lab on a Chip, 8(5):672–677, 2008.
- [29] D. Witters, N. Vergauwe, S. Vermeir, F. Ceyskens, S. Liekens, R. Puers, and J. Lammertyn. *Biofunctionalization of electrowetting-on-dielectric digital microfluidic chips for miniaturized cell-based applications*. Lab on a Chip, 11:2790–2794, 2011.
- [30] I. Barbulovic-Nad, H. Yang, P. Park, and A. R. Wheeler. *Digital microfluidics for cell-based assays*. Lab on a Chip, 8:519, 2008.
- [31] V. Srinivasan, V. K. Pamula, and R. B. Fair. *An integrated digital microfluidic lab-on-a-chip for clinical diagnostics on human physiological fluids*. Lab on a Chip, 4:310–315, 2004.
- [32] N. Vergauwe, D. Witters, Y. T. Atalay, B. Verbruggen, S. Vermeir, F. Ceyskens, R. Puers, and J. Lammertyn. *Controlling droplet size variability of a digital lab-on-a-chip for improved bio-assay performance*. Microfluidics and Nanofluidics, 11(1):25–34, January 2011.
- [33] N. Vergauwe, D. Witters, F. Ceyskens, S. Vermeir, B. Verbruggen, R. Puers, and J. Lammertyn. *A versatile electrowetting-based digital microfluidic platform for quantitative homogeneous and heterogeneous bio-assays*. Journal of Micromechanics and Microengineering, 21(5):054026, May 2011.
- [34] D. Witters, N. Vergauwe, R. Ameloot, S. Vermeir, D. De Vos, R. Puers, B. Sels, and J. Lammertyn. *Digital microfluidic high-throughput printing of single metal-organic framework crystals*. Advanced materials, 24(10):1316–1320, March 2012.
- [35] R. Sista, Z. Hua, P. Thwar, A. Sudarsan, V. Srinivasan, A. Eckhardt, M. Pollack, and V. Pamula. *Development of a digital microfluidic platform for point of care testing*. Lab on a Chip, 8(Dec):2091–2104, 2008.

-
- [36] L. Malic, T. Veres, and M. Tabrizian. *Two-dimensional droplet-based surface plasmon resonance imaging using electrowetting-on-dielectric microfluidics*. *Lab on a Chip*, 9(3):473–475, 2009.
- [37] L. Luan, R. D. Evans, N. M. Jokerst, and R. B. Fair. *Integrated optical sensor in a digital microfluidic platform*. *IEEE Sensors Journal*, 8(5):628–635, May 2008.
- [38] C. Lerma Arce, D. Witters, R. Puers, J. Lammertyn, and P. Bienstman. *Silicon photonic sensors incorporated in a digital microfluidic system*. *Analytical and Bioanalytical Chemistry*, 404(10):2887–94, December 2012.
- [39] L. Luan, M. W. Royal, R. Evans, R. B. Fair, and N. M. Jokerst. *Chip scale optical microresonator sensors integrated with embedded thin film photodetectors on electrowetting digital microfluidics platforms*. *IEEE Sensors Journal*, 12(6):1794–1800, June 2012.
- [40] Mobidiag, <http://www.mobidiag.com/default.aspx>.

2

Label-free biosensors

As mentioned in Chapter 1, label-free technologies have recently attracted significant interest for sensitive and quantitative analysis of biological systems. There are several different classes of label-free sensors, some already commercially available, others still under development. In this chapter, we will highlight and compare some of the more promising approaches. We will describe the fundamental principles of these different methods and discuss their advantages and disadvantages. Finally, we will focus on ring resonator sensors for which we will give an extensive overview since these are chosen to be the transducers of all three devices we present in this thesis.

2.1 Mechanical biosensors

Acoustic wave biosensors and microcantilevers are two classes of mechanical biosensors that have been successfully implemented and commercialized.

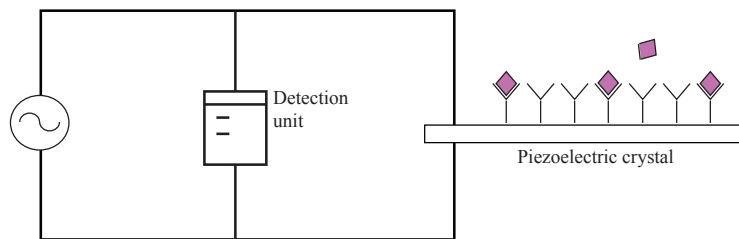
Acoustic wave biosensors, including quartz crystal microbalance (QCM) and integrated surface acoustic wave (SAW) technologies, are based on mechanical transduction and thus do not require labels. Both approaches utilize a piezoelectric quartz crystal connected to an oscillating external circuit that is able to measure the resonant oscillatory frequency of the system (see Figure 2.1a). Typically for QCM applications, a few tenths of a mm-thick quartz crystals are cut in the AT form, i.e. at a $35^{\circ}10'$ angle from the Z-axis. This geometry

provides a stable oscillation with almost no temperature fluctuation in frequency at room temperature. In most applications, the QCM technique relies upon circular quartz crystals operating in the thickness shear mode of oscillation, where basically the top and bottom half of the crystal move in opposite directions. Under these conditions, the lateral amplitude of a vibrating crystal is 1-2 nm. Any mass bound to the surface will tend to oscillate with the same lateral displacement and frequency as the underlying crystal. The usual fundamental resonance frequencies of these devices are in the range of 5-20 MHz. There are additional resonances at the 3rd, 5th, etc. harmonic overtones, whose frequencies are approximate, but not exact, odd multiples of the fundamental resonance frequency. At higher frequencies the devices become more sensitive but too thin and thus too fragile for practical use since the crystal thickness is inversely proportional to the frequency [1].

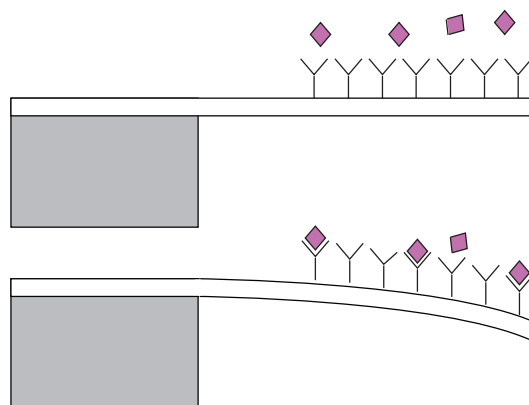
In their use as biosensors, when molecules bind to the surface of the sensor, the acoustic wave traveling along the device is affected by a change in amplitude, phase or frequency, which provides information about the binding event [2]. These sensors have been utilized to detect a wide range of biomolecules, including nucleic acids [3, 4], proteins [5], and lipids [6]. Their specificity is provided by the coating layer, which can range from a modified gold surface to a variety of polymers [7, 8]. While acoustic wave devices are extremely sensitive towards binding events, quantitative multiplexed biosensing is limited in these devices. Additionally, considerations such as viscoelasticity and hydration lead to non-linearities in frequency shifts accompanying biomolecular binding to the quartz crystal microbalance surface [9]. QCM technology has been commercialized by *Q-sense* and can be used to characterize the formation of thin films (nm) such as proteins, polymers and cells onto surfaces in liquid [10].

Another type of mechanical sensors that has recently attracted considerable attention as a multiplexed, label-free biosensing platform are microcantilevers (see Figure 2.1b). They can measure mass, temperature or stress changes on the surface of the cantilever. When a binding event occurs on this surface, three different methods can be used to quantify it: deflection of the cantilever [11], a change in the resonance frequency of the cantilever [12] or a change in the stress exerted on the cantilever, which generates an electric current in an attached piezoelectric element [13].

We could say that the simplest transduction event to monitor is the change in deflection, measured by reflecting a laser beam off the back of a cantilever and measuring the position with a split photodiode. However, the position of bound molecules must be considered during deflection measurements, since each molecule does not generate the same amount of deflection depending on its position and its mass. Furthermore, the required number of molecules bound to a surface to exert a detectable deflection is significantly higher than



a) Quartz crystal microbalance (QCM)



b) Microcantilever biosensor

Figure 2.1: a) Concept of a quartz crystal microbalance (QCM) based sensor. The binding of molecules changes a property of the acoustic wave which can be measured in a change as amplitude, phase or frequency. b) Microcantilever working principle. The deflection or other induced changes provoked by the binding of molecules quantifies the binding event.

with the other two transduction methods [14]. The resonance-based method involves monitoring the change in the resonance frequency upon binding of an analyte. While the readout equipment for this method, typically accomplished using interferometric schemes, is significantly more complex than that for deflection-based methods, it is by far the most sensitive [11]. However one limitation is that the oscillations of microcantilevers are highly susceptible to damping effects in liquids, which vary with solution composition. In the piezoelectric method, the binding of an analyte causes the cantilever to deflect, subsequently depolarizing the material and generating a current. It should also be noted that piezoelectric-modified microcantilevers can be used for both deflection-based and resonance-based measurements. Currently, several companies are developing commercial microcantilever-based systems, including *Protiveris* [15], *Contentris* [16] and *Bioscale* [17].

2.2 Electrical biosensors

The basis of these detection systems is a binding-induced change in some electrical property of the circuit, of which the sensor is the main component. One of the more recent electronic biosensors makes use of the basic component in microelectronics, i.e. the metal-oxide-semiconductor field-effect transistor (MOSFET). In normal transistor operation, a semiconducting element is attached to a source and a drain electrode, and current flowing through the element is modulated by changing the voltage applied to a gate electrode. In a FET-based nanowire biosensor configuration, the SiNW (silicon nanowire), functionalized with appropriate receptors is connected to a source and drain electrode. Binding of target biomolecules changes the dielectric environment around the nanowires and plays a role similar to that of the gate electrode. Thus, molecular binding can be directly quantified as a change in the conductivity of the nanowires [18] (see Figure 2.2). Their small dimensions provide ultrahigh sensitivity down to the single-molecule level [19]. Nanowire sensing technology holds much promise for multiparameter biological detection; however, there are some significant challenges to be addressed before routine operation of higher-order multiplexed analyses can be realized. One is that their performance deteriorates at physiological ionic strengths. Ions in solution respond similarly to the biomolecular target, and thus the device can experience a much diminished response to the binding event [20]. This can be avoided by desalting the sample prior to analysis, but introduces an additional preparative step. The second one is reproducibility and uniformity of the integration of nanowires [21].

Another type of promising electrical biosensors are carbon nanotubes (CNT). They have been widely investigated as biosensors, owing to their unique

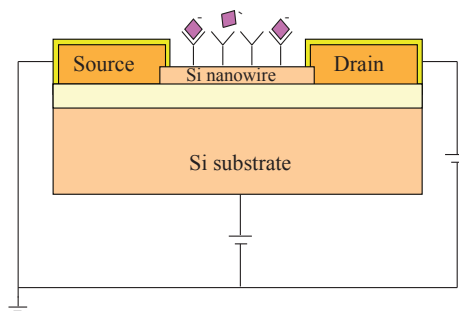


Figure 2.2: Operating principle of a silicon nanowire based metal-oxide-semiconductor field-effect transistor (MOSFET) as a biosensor. Charged molecules binding to the nanowire channel induce an electric field which results in a decrease in the conductance.

structure-dependent electronic and mechanical properties [22]. They have shown potential for biological detection. However, widespread utility has been limited to date by difficulties in controlling the physical parameters relevant to biosensing: length, diameter, and chirality [23]. These issues are particularly significant for multiplexed sensing, in which uniform and reproducible performance of each sensor element is essential.

Another electrical transduction method that has shown promise for multiparameter biological detection is electrochemical impedance spectroscopy (EIS). In EIS, sensing is accomplished by measuring changes in the resistance and/or capacitance of the electrode-solution interface upon binding of a target molecule to a receptor-functionalized surface [24–26]. Currently several companies are commercializing EIS-based system such as *ACEA Bioscience* [27] and *Applied BioPhysics* [28].

2.3 Optical biosensors

Optical biosensors make use of the fact that biological molecules have a dielectric permittivity ϵ greater than that of air and water, meaning that they reduce the propagation velocity of electromagnetic fields that pass through them. Thus optical biosensors translate changes in the propagation speed of light into a quantifiable signal proportional to the amount of biological material present on the sensor surface.

We can classify optical biosensors in three categories: plasmonic biosen-

sors, interferometer-based biosensors and cavity biosensors. Each of them can have a number of different implementations (free space optics, integrated waveguides, photonic crystals, fibers...) and material systems. We will briefly introduce the main working principles, which can help to understand different configurations. For a more complete overview about optical label-free biosensors we refer to [29]. For a discussion on fiber optic sensors, we refer to Chapter 3.

2.3.1 Surface plasmon resonators

The most common optical biosensor is the surface plasmon resonance (SPR) device. The SPR biosensor was first demonstrated by Liedberg [30] and since then it has been widely developed and commercialized [31–37] and hundreds of publications have demonstrated its outstanding performance to evaluate complex biosensing interactions [38–42].

A surface plasmon wave (SPW) is a charge density oscillation that occurs at the interface of two media with dielectric constants of opposite signs, such as a metal and a dielectric. It only propagates when the interface meets the surface plasmon polariton condition, i.e. when there exists a certain interaction or coupled state between the free electron oscillations in this interface and the incident light, which only happens when the real part of the dielectric constant of the metal is negative and its absolute value is greater than the real part of the dielectric constant of the dielectric, which has to be positive:

$$\begin{aligned} \Re(\epsilon_{dielectric}) \cdot \Re(\epsilon_{metal}) &< 0 \\ |\Re(\epsilon_{dielectric})| &< |\Re(\epsilon_{metal})| \end{aligned} \quad (2.1)$$

This condition implies that the field component of the mode guided at the metal-dielectric interface consists of two exponentially decaying functions, with a typical penetration depth much deeper into the dielectric than into the metal. Light is coupled to the interface of a thin metallic film (typically gold) via total internal reflection where propagating surface plasmon modes are excited, if the photons are of a particular frequency and incident angle. The evanescent field associated with the plasmon resonance samples the proximal optical dielectric environment and is highly sensitive to local changes in refractive index, including those associated with the binding of biomolecules to receptors presented by the surface. When biomolecules bind to specific receptors attached to the metallic film, the corresponding changes in the refractive index modulate the intensity of light reflected off the surface, which is measured by the detector.

Four main methods to excite SPR define the most common implementations of SPR biosensors: prism coupling, waveguide coupling, fiber optic coupling and grating coupling. The implementation that offers the best limit of

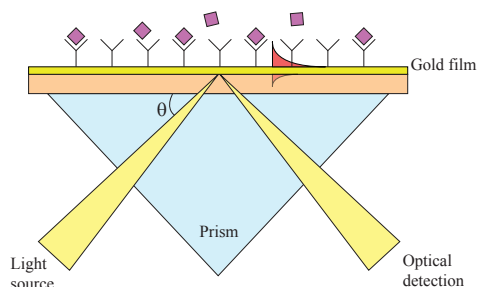


Figure 2.3: Working principle of a surface plasmon resonance based sensor with coupling prism in the Kretschmann configuration. Monochromatic light is coupled in while scanning the angle of incidence. For a certain angle, light will couple to the surface plasmon wave. After biomolecules bind to the metallic surface, the angle at which this occurs will change. The amount of refractive index change and the binding of biomolecule can be quantitatively deduced from this change.

detection (LOD) is the prism coupling configuration and it was first commercialized by Biacore. The incident light beam is totally reflected at the prism-metal interface and generates an evanescent field penetrating into the metal layer (see Figure 2.3). Since the incident power is then coupled to the surface plasmon wave, no output intensity is observed for that angle. When a binding event takes place on the metallic layer, the refractive index near the metallic-bio-interface will change, together with the resonance condition. This means that the intensity drop will occur for a different angle. This shift in resonant angle can be used to quantify the amount of refractive index change and the binding of biomolecules can be quantitatively deduced from this. It is also possible to work at a fixed angle and scan a range of wavelengths to see a resonance dip. Although this implementation offers a good LOD, it is bulky and it is difficult to integrate in a multiplexed system.

Other implementations have also been demonstrated as e.g. waveguide coupling which offers a good alternative to the prism. They are robust and easy to integrate with other optical and electrical components. Debackere et al. [39] integrated a SPR sensor in a Silicon-on-Insulator (SOI) chip with a LOD of 10^{-3} refractive index unit (RIU)¹. He et al. [43] demonstrated a detection of 10 pM

¹Refractive index unit (RIU)' makes reference to a unit change of the refractive index of a measured fluid. Note the difference with 'Resonance Units (RU)' used typically for SPR devices developed by Biacore [31] (market leader in commercial SPR devices) where 1 RU = 0.0001°.

DNA using SPR with signal amplification using gold particles. A SPR sensor excited using two light emitting diodes (LEDs) achieved a LOD of 2×10^{-5} RIU according to Suzuki [44]. Integration of SPR sensors on optical fibers is also possible, but this will be discussed in Chapter 3.

Another promising technique for the multiplexing approaches is surface plasmon resonance imaging (SPRI), also referred to as surface plasmon resonance microscopy. In this technique a CCD detector is used to image the intensity of light reflected off the surface, which directly corresponds to the amount of material bound to the metal film at a given image position. In this arrangement, changes in reflected light intensity can be measured down to a resolution of approximately $4 \mu\text{m}$, allowing for highly multiplexed measurements of a variety of biological binding events [45]. However, multiplexing comes with a cost, SPRI typically has limits of detection 10-100 times higher (worse) than standard non-imaging SPR spectroscopy [46].

2.3.2 Interferometer-based biosensors

Mach-Zehnder (MZI), Young (YI) and Hartman interferometers are the usual configurations employed for biosensing.

In the integrated version of a MZI, coherent, single frequency light from a laser enters the single-mode input waveguide and is split equally at a Y-junction. One branch has a window over the top of it allowing the evanescent field of that branch to interact with the sample while the reference arm is protected from the sample with a thick cladding layer. This scheme is illustrated in Figure 2.4. The two branches recombine at the output, resulting in interference, and a photodetector measures the intensity. Generally, the waveguide structure must be single polarization and single mode so that multimodal and cross-polarization interference do not appear at the output. A biomolecular interaction in the sensor area within the evanescent field will produce a variation in the effective refractive index of the light propagating through this area, inducing a phase difference between the light traveling in the sensor and the reference arm. The interferometric modulation at the device output is described by [29]:

$$I \propto \cos(\Delta\phi) \quad (2.2)$$

$$\Delta\phi = \frac{2\pi\Delta L}{\lambda} (n_{eff,S} - n_{eff,R}) \quad (2.3)$$

where n_{eff} is the effective refractive index, ϕ is the phase, ΔL is the length difference between the sensing arm and the reference arm, λ is the light wavelength and I is the light output intensity. The labels S and R stand for the sensing and the reference arms, respectively.

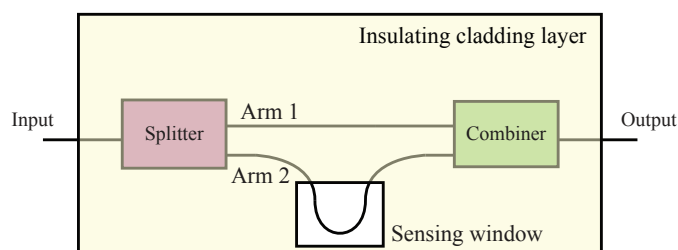


Figure 2.4: Working principle of a Mach-Zehnder interferometer (MZI). A lightwave is split into two paths. One branch has a window over the top of it allowing the evanescent field of that branch to interact with the sample while the reference arm is protected from the sample with a thick cladding layer. After combining both lightwaves again, the output intensity depends on the phase difference $\Delta\phi$ between the two waves.

Depending on the amount of phase delay (induced by e.g. a different refractive index medium or optical path length), the waves will (partially or completely) interfere constructively or destructively. When used in biosensing applications, the phase change can be very small and not easily detectable. Therefore it is more practical to scan a certain range of wavelengths (Figure 2.5) since in Equation 2.3 we see that the phase change $\Delta\phi$ depends on the wavelength λ .

An attractive aspect of this device is the possibility of using long interaction lengths, thereby increasing the sensitivity. Most common Mach-Zehnder interferometers are based on silicon nitride as a core layer and silica as cladding. MZIs have been shown to be able to detect refractive index changes of 10^{-7} RIU [47]. Prieto et al. [48] have achieved a LOD of 2×10^{-5} RIU using an anti-resonant reflecting optical waveguide (ARROW) in silicon dioxide. In silicon nitride Schipper et al. [49] reported a LOD of 10^{-4} RIU using a standard Mach-Zehnder interferometer.

A Hartman interferometer is a type of Mach-Zehnder implementation, where receptor molecules are patterned on top of a planar slab waveguide. Light is recombined on the chip which creates interference patterns between pairs of functionalized and unfunctionalized strips and is then coupled out of planar waveguides using gratings. A Hartman interferometer has been used by Schneider et al. for immunoassays for human chorionic gonadotropin (hCG) i.e. the human pregnancy hormone [50]. They achieved 5 ng/ml detection limit

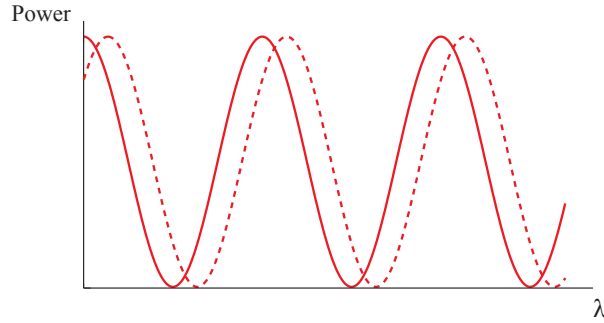


Figure 2.5: When scanning a certain wavelength range, more information is obtained. Due to binding of biomolecules to one sensing arm, the output spectrum will change (solid to dashed line).

and improved it to 0.5 ng/ml using signal amplification with gold nanoparticles conjugated to second any anti-hCG antibodies.

A Young interferometer (YI) is another well-explored interferometric device for biosensing. The YI is a waveguide with an integrated Y-junction acting as a beam splitter and, contrary to the MZI, the two beams are not recombined again. The exiting light from both arms is projected onto a CCD camera giving an interference pattern. The spatial intensity distribution, $I(x)$, along the detector screen, x , is given by the following equation [51]:

$$I(x) = 1 + \cos\left(\frac{2\pi nd}{\lambda f} - \delta\right) \quad (2.4)$$

where λ is the wavelength, n_{eff} the effective RI, δ represents a phase shift due to a RI change, and d and f are the distance between the two arms and the distance between the YI output and the screen, respectively. The equation shows that a phase change on the reference arm causes a shift in the position of the interference fringes, which can be analyzed quickly with a fast Fourier transform of the spatial intensity [52].

The first demonstration of an integrated YI for sensing was demonstrated by Brandenburg and Henninger [52]. A follow-up to this work using the same design concept yielded a RI LOD of 10^{-7} RIU [53]. A commercialized Young interferometer biosensor from *Farfield Scientific* [54] is currently available (called *AnaLight*®). It can probe two polarizations of light sequentially which provides extra information on the conformation of the biolayers.

A last class of interferometer-based biosensors is called backscattering interferometry. This typically consists of a laser focused onto a small sensing

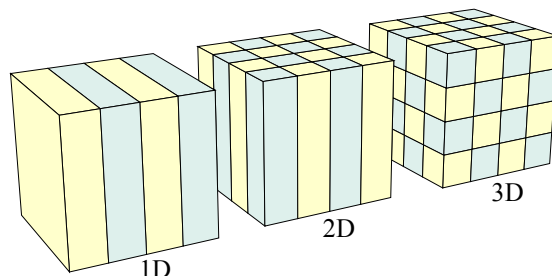


Figure 2.6: Photonic crystals can have periodicity in 1, 2 or 3 dimensions.

area and a detector to analyze the reflected intensity. Sub-wavelength structures (biomolecules) on the sensing surface results in interference at the detector. The reflected beams interfere generating a signal that directly depends on the amount of adsorbed molecules. This technique was implemented in various configurations, arrays, chips, fibers and commercialized by *Silicon Kinetics* [55], *FortéBio* [56] and *Biametrics* [57], amongst others.

2.3.3 Photonic crystals

An interesting photonic structure that has proved to be effective for multiplexed screening and detection is the photonic crystal (PhC) [58]. Photonic crystals are basically structures that exhibit a periodic variation of the refractive index. This periodicity can occur in 1D, 2D or 3D as illustrated in Figure 2.7. The lattice structure is generated on the length scale of the light wavelength, which generates photonic bandgaps where light cannot propagate in the crystal. The width and position of the photonic gap is highly dependent on the refractive-index change between the dielectric materials and on the periodicity of the structure [59], which is exploited for sensing. With use of this principle of detection, photonic crystal biosensors have demonstrated the ability to detect adsorbed protein down to approximately 1 pg/mm^2 on the surface [60].

Another interesting principle to measure photonics crystal structures is by introducing a photonic defect within the bandgap, so that the PhCs periodic structure can be disturbed leading to the formation of the defect mode. Light resonant with the defect mode can propagate in the PhC. As a result, in the transmission (or reflection) spectrum, the defect mode appears as a relatively sharp peak within the bandgap. Since the spectral position of the defect mode is highly sensitive to the change in the local environment around the 'defect', it can be used as the sensing transduction signal when the refractive index changes as a result of the binding of the molecules to the defect. Lee et al. for the first time demonstrated a PC microcavity biosensor that is capable of monitoring protein

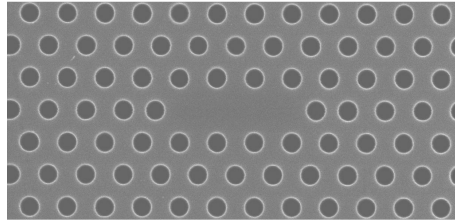


Figure 2.7: SEM picture of a photonic crystal structure. The defect introduced in the periodic structure results in a sharp peak within the bandgap of the transmission (or reflection) spectrum. In this case the defect is defined by the removal of a few holes in the periodic structure [62].

binding on the walls of the defect hole and quantitatively measuring the protein diameter [61].

Photonic crystals are interesting structures that can be implemented for many applications (e.g. sensing [63–65], lasing [66–68], filtering [69–71]) but are, on the other hand, notoriously sensitive to fabrication errors. Indeed they exhibit their interesting properties due to their periodic structuring, but small errors or variations in this periodicity are sometimes detrimental for their quality. For a review on photonic crystal based biosensors, we refer to Zhao [72].

Grating-coupled waveguide sensors

A particular case of a photonic crystal in 1D is the well-known grating coupler. Grating-coupled waveguide sensors are one of the first transducers developed [73]. A grating coupler is a system of periodic disturbances in a planar single-mode waveguide. The grating allows the excitation of a guided mode of the waveguide at a certain angle of incidence which is sensitive to any variation in the refractive index at the surface of the waveguide within the evanescent field region. Therefore, induced changes in the incoupling angle can be used for sensing. Alternatively, it is possible to evaluate the outcoupling angle of the guided light.

In the input grating coupler device, s- and p-polarized laser beams are typically scanned at a variable angle to excite both TE and TM modes. The grating sensor requires a precise mechanical movement of the rotation stage that includes the sensing platform, the fluidics and the photodetectors [74]. On the

other hand, output grating devices are based on the monitoring of the outcoupling angle, which does not require a moving stage, simplifying the setup and decreasing the response time [75]. The in- and output grating configurations were initially developed by Nellen and Lukosz et al., showing a refractive index LOD around 10^{-6} RIU. Later, Wiki et al. [76] developed the so-called WIOS (wavelength interrogated optical sensor), based on grating couplers. The approach is based on a single-mode waveguide structured with two grating couplers, to couple the light in and out, respectively. The change of the refractive index due to an interaction on the surface is monitored by scanning the resonance peak at a fixed angle of incidence by a tunable laser diode and adjusted with a mirror. A compact device including four channels and the laser source, the mirror, the flow cell and other components was also developed and tested for biosensing of low molecular weight analytes, such as biotin, showing mass detection limits of 0.3 pg/mm^2 . The device showed a label-free detection of molecules as small as 200 Da.

Commercial systems for high-throughput cell-based assays are offered by *Corning* [34] and *SRU Biosystems* [77], which fabricate low-cost gratings that can be incorporated into standard microtiter plates. However, multiplexed interrogation of different wells of the plate in parallel typically requires optical imaging that only offers end-point read-out and in consequence loses information about binding kinetics and affinity.

2.3.4 Ring resonators

Ring resonator transducers are increasingly being used for biosensing due to their high sensitivity and their potential to be produced in highly dense arrays for multiplexed analysis. In general, ring resonators consist of a loop and a coupling mechanism to access this loop. When waves that travel in the loop have a round trip phase shift that equals an integer times 2π , the waves interfere constructively and the cavity is in resonance.

Ring resonators are well-known photonic components [78, 79] that can be used not only as biosensors but as filters in wavelength-division-multiplexed networks [80], as delay elements in optical buffers [81], and when combined with active materials as laser cavities [82] and modulators [83]. When used for biosensing applications, a measurable shift in the resonance wavelength is induced when molecular binding occurs in the range of the evanescent field. This shift can be continuously monitored over time which gives information on the analyte concentration, affinity between molecules and the kinetics of the biochemical reaction.

Since the concept was first described by Boyd et al. [84], multiple research groups have contributed to the experimental characterization. Ramachandran

[85] has demonstrated a ring resonator-based sensor in glass that was able to detect 500 nM of a sequence of 25 base pairs of the genome of the bovine viral diarrhoea virus. A polymer-based ring resonator was fabricated by Chao [86] and had a detection limit of 10^{-7} RIU. In our group, Katrien De Vos [87] has designed an SOI ring resonator with a detection limit of 10^{-5} RIU. She was later able to show multiplexed detection with these sensors using an infra-red camera [88]. In the industry, Genalyte [89] is the only company that makes use of ring resonators as transducers. Currently it is launching a multiplexed label-free biosensor platform based on silicon ring resonators. In collaboration with this company, the group of R.C Bailey made extensive contributions to the characterization of the platform [90–95].

We will dedicate the next section to study extensively silicon photonic ring resonator label-free biosensors, although more detailed information on ring resonators can be found in the PhD works of Tom Claes [96] and Katrien De Vos [97].

2.4 Silicon photonic ring resonators label-free biosensors

As mentioned above, when the wavelength of the coupled light fits an integer number of times in the optical path length of the ring resonator, the waves interfere constructively and the cavity is in resonance. This is illustrated by Equation 2.5 where λ_{res} is the resonant wavelength, n_{eff} the effective index of the resonant mode, L is the physical roundtrip length and m is a strictly positive integer.

$$\lambda_{res} = \frac{n_{eff}L}{m} \quad (2.5)$$

One or more access waveguides are coupled to the ring to excite its resonant modes. Two main configurations, all-pass configuration and channel-drop configuration, with one and two access waveguides respectively, are discussed below.

All-pass ring resonators

In the all-pass configuration (Figure 2.8), one access waveguide couples a fraction k of its field amplitude to the ring. In an ideal lossless case, this amplitude cross-coupling coefficient and the amplitude self-coupling coefficient obey the condition $k^2 + r^2 = 1$. Initially, rE_{in} will be transmitted to the output and $(-jk)E_{in}$ is coupled to the ring. Inside the ring, the wave amplitude is multiplied by a factor $a = \exp(-\frac{\alpha}{2}L)$ where L is the ring length and α the power

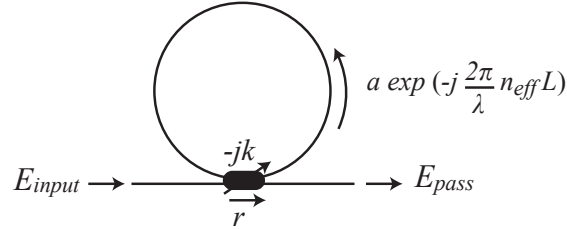


Figure 2.8: An all-pass ring resonator has one access waveguide that couples a fraction k of its field amplitude to the ring, while a fraction r remains in the access waveguide. The cavity is in resonance when the wavelength of the coupled light fits an integer number of times in the optical path length of the ring resonator.

attenuation coefficient. Note that the phase of the resonator mode runs $\frac{\pi}{2}$ radians behind that of the access waveguide mode. The transmission after one round trip is $a \exp(-j \frac{2\pi}{\lambda} n_{eff} L)$. It is obvious that the amplitude of the wave at the output port can be considered as an infinite sum of waves that have passed through the ring once up to an infinite number of times, from which the power transmission can be formulated as [98]:

$$T_{allpass}(\lambda) = \frac{a^2 + r^2 - 2ar \cos \phi}{1 + (ra)^2 - 2ar \cos \phi} \quad (2.6)$$

where $\phi = \frac{2\pi}{\lambda} n_{eff} L$ is a single pass phase shift.

The all-pass ring resonator owes its name to the ideal case of a lossless ring, when $a=1$ and the power transmission is unity for all wavelengths. In this case the ring only acts as a phase rotator. However, in practical ring resonators ($a < 1$) the power transmission exhibits dips at the resonance wavelengths, caused by destructive interference between the access waveguide mode and the light coupled back from the ring to the access waveguide.

Each resonance dip is characterized by the following parameters, that are illustrated in Figure 2.9:

Extinction ratio T_{max}/R_{min} :

$$T_{max} = \frac{(a+r)^2}{(1+ar)^2} \quad (2.7)$$

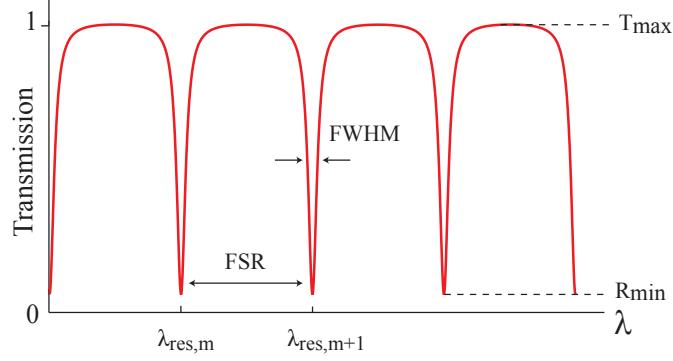


Figure 2.9: The dips in the transmission spectrum of an all-pass ring resonator at the resonance wavelengths are characterized by their full-width at half-maximum (FWHM) and on-off extinction ratio (T_{max}/R_{min}). The spectral distance between consecutive resonances is called the free spectral range (FSR).

$$R_{min} = \frac{(r - a)^2}{(1 - ar)^2} \quad (2.8)$$

Full-width at half maximum (FWHM):

$$FWHM = \frac{(1 - ar)\lambda_{res}^2}{\pi n_g L \sqrt{ar}} \quad (2.9)$$

Free spectral range (FSR): spectral distance between subsequent resonances.

In the first order approximation of dispersion the FSR becomes:

$$FSR = \frac{\lambda^2}{n_g L} \quad (2.10)$$

When the roundtrip loss increases (decrease of a) and coupling increases (r decreases), the resonances are broader. The extinction ratio of an under-coupled ring resonator ($r > a$) increases with increasing coupling until it becomes infinite at critical coupling ($r = a$), when the coupled power is equal to the power loss in the ring. Over-coupling ($r < a$) decreases the extinction ratio again and further broadens the resonances.

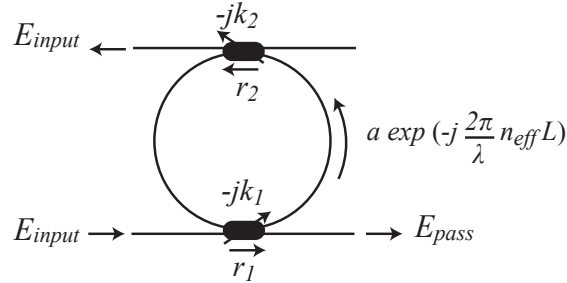


Figure 2.10: A channel-drop ring resonator has a second access waveguide that receives part of the light of the cavity, providing a power transmission spectrum with resonance peaks at its drop port.

Channel-drop ring resonators

The previous is the simplest configuration of a ring resonator. Here we introduce a second access waveguide; this configuration will be used for our sensor devices.

Part of the light is now coupled to the drop port of the second access waveguide, while the pass port of the first access waveguide is similar to the output port of the all-pass resonator previously described. The power transmission in continuous wave regime to that pass port can be described as [98]:

$$T_{pass}(\lambda) = \frac{r_1^2 + a^2 r_2^2 - 2ar_1 r_2 \cos \phi}{1 + (ar_1 r_2)^2 - 2ar_1 r_2 \cos \phi} \quad (2.11)$$

which is similar to the transmission of an all-pass ring resonator (Equation 2.6) with a round trip ar_2 . The coupling to the second access waveguide introduces an extra loss factor which is reflected as follows in the resonance dips (Figure 2.11):

$$T_{max} = \frac{(r_1 + ar_2)^2}{(1 + ar_1 r_2)^2} \quad (2.12)$$

$$R_{min} = \frac{(r_1 - ar_2)^2}{(1 - ar_1 r_2)^2} \quad (2.13)$$

$$FWHM = \frac{(1 - ar_1 r_2) \lambda_{res}^2}{\pi n_g L \sqrt{ar_1 r_2}} \quad (2.14)$$

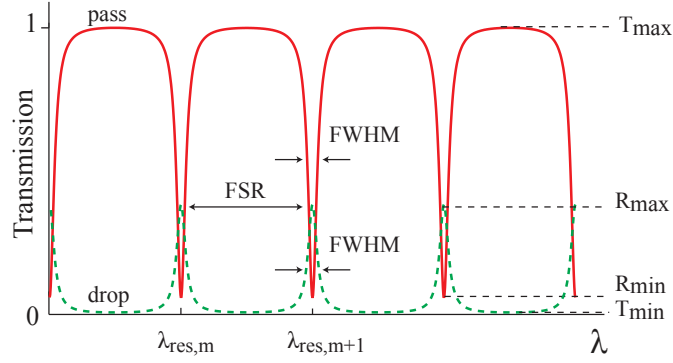


Figure 2.11: The transmission spectrum of the drop port has peaks at the resonance wavelengths with an on-off extinction ratio R_{max}/T_{min} , while the pass port exhibits resonance dips similar to the transmission of an all-pass ring resonator.

The on- off extinction ratio T_{max}/R_{min} becomes infinite at the critical coupling condition $r_1 = ar_2$. The second access waveguide has a power transmission spectrum at its drop port that can be formulated as [98]:

$$T_{drop}(\lambda) = \frac{a(1-r_1^2)(1-r_2^2)}{1+(ar_1r_2)^2-2ar_1r_2\cos\phi} \quad (2.15)$$

which exhibits peaks at the resonance wavelengths (Figure 2.11). These peaks are characterized by the FWHM (equation 2.14) and the extinction ratio at the drop port is defined as R_{max}/T_{min} :

$$R_{max} = \frac{a(1-r_1^2)(1-r_2^2)}{(1-ar_1r_2)^2} \quad (2.16)$$

$$T_{min} = \frac{a(1-r_1^2)(1-r_2^2)}{(1+ar_1r_2)^2} \quad (2.17)$$

Alternative parameters of a ring resonator related to the previously defined are:

Finesse which measures the sharpness of resonances relative to their spacing.

$$\mathcal{F} = \frac{FSR}{FWHM} \quad (2.18)$$

Quality factor which measures the sharpness of the resonance relative to its central wavelength.

$$Q = \frac{\lambda_{res}}{FWHM} \quad (2.19)$$

To define the Q-factor, the microring is excited to a certain level and the rate of power decay is considered. From this point of view it is understood that round trip losses as well as coupling in the directional couplers are loss factors that need to be reduced to obtain high-Q resonances. Therefore an all-pass resonator typically exhibits a higher Q-factor than an add-drop resonator (when both devices operate close to critical coupling).

2.4.1 Lorentzian approximation of resonances

The shape of the transmission curves approximates a Lorentzian curve around resonance. Therefore, the following easy-to-fit Lorentzian functions will be used to fit to resonance dips in the pass transmission and resonance peaks in the drop transmission port.

$$T_{dip}(\lambda) \approx \frac{R_{min} \left(\frac{FWHM}{2} \right)^2 + (\lambda - \lambda_{res})^2}{\left(\frac{FWHM}{2} \right)^2 + (\lambda - \lambda_{res})^2} \quad (2.20)$$

$$T_{peak}(\lambda) \approx \frac{R_{max} \left(\frac{FWHM}{2} \right)^2}{\left(\frac{FWHM}{2} \right)^2 + (\lambda - \lambda_{res})^2} \quad (2.21)$$

For a detailed derivation of the Lorentzian approximation of resonances we refer to [96].

2.4.2 Coupling section

A good understanding of the behavior of the coupling section is crucial for ring resonator filter design. Two coupling schemes are commonly used for coupling light from a waveguide to a resonator: multimode interferometers (MMIs) and directional waveguide couplers. Although MMIs [99] can provide 50% coupling with high tolerance to dimensional variations, they are much more unstable when used for very low coupling as required in low loss ring resonators. Therefore we used directional couplers which consist of two waveguides that are brought close together so that the waveguide modes are coupled and power can be transferred from one mode to the other.

The common directional coupler employed for the rings in this thesis consists of a section with length L_c where the two waveguides are parallel to each other with a gap G_c , and two identical sections where one of the two waveguides

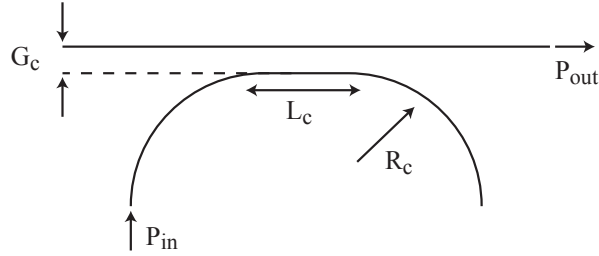


Figure 2.12: The directional coupler employed in our ring resonators consists of a section with length L_c where the two waveguides are parallel to each other with a gap G_c , and two identical sections where one of the two waveguides is bent away from the other with radius R_c .

is bent away from the other with radius R_c (Figure 2.12). The power cross coupling can be formulated as [97]:

$$k^2 = \frac{P_{out}}{P_{in}} = \sin \kappa \cdot L_c + \kappa_0^2 \quad (2.22)$$

with $\kappa [1/\mu m]$ the coupling coefficient per unit distance in the parallel section of the coupler and κ_0 the offset coupling in the two bent regions. The coupling strength (both κ and κ_0) increases with increasing wavelength, due to a decreasing mode confinement.

2.4.3 Silicon ring resonator for biosensing

A ring resonator label-free biosensor measures selective affinity interactions between analyte molecules and receptor molecules immobilized on the ring waveguide surface (Figure 2.13). Since most biological molecules (proteins, DNA, ...) have a refractive index (around 1.45) larger than that of the aqueous solvent (around 1.31), this molecular binding locally increases the refractive index in the range of the evanescent field of the waveguide mode. The resulting phase change of the mode induces measurable shifts of the resonance wavelengths of the ring, which are continuously monitored over time and which give information on the analyte concentration, affinity between the molecules and the kinetics of the biochemical reaction.

The silicon ring resonators used in this thesis were fabricated in SOI using standard CMOS processing tools, in particular 193 nm deep-UV lithography and dry etching [100, 101], so their manufacturing can be scaled to high volumes

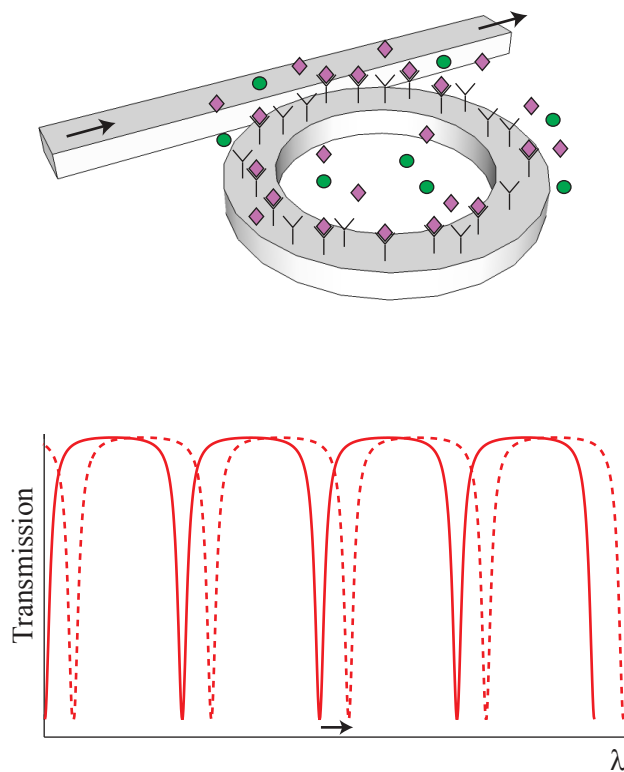


Figure 2.13: A ring resonator label-free biosensor measures selective affinity interactions between analyte molecules and receptor molecules immobilized on the ring waveguide surface. This molecular binding locally increases the refractive index in the range of the evanescent field of the waveguide mode, inducing measurable shifts of the resonance wavelengths of the ring, which are continuously monitored over time and which give information on the analyte concentration, affinity between the molecules and the kinetics of the biochemical reaction.

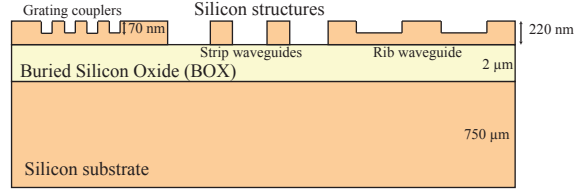


Figure 2.14: Silicon-on-insulator (SOI) photonic structures are defined in silicon separated from a silicon substrate by a buried oxide layer with low refractive index. The high index contrast of silicon and silicon oxide offers many benefits to the platform.

at wafer scale using very reliable processes. This enables high quality sensors cheap enough to be disposable, which avoids complex cleaning of the sensor surface after use, since they can be single-use. Figure 2.14 illustrates basic photonic components defined in an SOI wafer.

The rings consist of a silicon core with high refractive index (3.476 at 1.55 μm wavelength) separated from a silicon substrate by a buried oxide layer with low refractive index (1.44 at 1.55 μm wavelength). This high index contrast benefits the sensor in two ways. First, the rings can be very compact (down to 5 μm diameter is possible), which provides for high throughput and highly multiplexed sensing. Second, the evanescent field in the ring waveguide decays rapidly. The mode thus only interacts with changes in the cladding that happen tens of nanometers away from the waveguide's surface, making it very selective towards refractive index changes caused by molecular binding near that surface. This is a large asset for our biosensors, since it decreases the interaction with refractive index changes in the liquid away from the surface, and therefore improves the signal-to-noise ratio. Although the evanescent field is non-uniformly distributed over the waveguide surface (Figure 2.15), the impact for sensing is negligible when working far enough from single-molecule detection limits.

From the resonant condition (Equation 2.5), the measurable shift of the resonance wavelength when biomolecular interaction takes place in the range of the evanescent field is formulated as follows:

$$d\lambda = \frac{dn_{eff}L}{m} \quad (2.23)$$

where m is the order of the resonant mode. n_{eff} is influenced by the refractive index of the cladding, which is altered upon sensing. Because of the large index contrast of SOI, the waveguide dispersion cannot be neglected. Thus, a change in resonance wavelength will also change the effective index. This is illustrated in Equation 2.24.

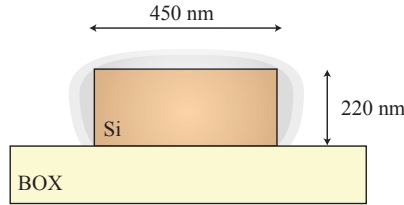


Figure 2.15: The evanescent field of the quasi-TE mode of a silicon wire waveguide decays rapidly with the distance from the waveguide; it has a penetration depth of only a few tens of nanometers.

$$d\lambda = \frac{\left(\frac{\partial n_{eff}}{\partial n_{bio}} dn_{bio} + \frac{\partial n_{eff}}{\partial \lambda} d\lambda \right) L}{m} \quad (2.24)$$

Taking into account that the group index of a dispersive SOI waveguide is given by:

$$n_g = n_{eff} - \lambda \frac{\partial n_{eff}}{\partial \lambda} \quad (2.25)$$

Inserting (2.5) and (2.25) into Equation 2.24, we can define the sensitivity of our rings as:

$$S = \frac{d\lambda}{dn_{bio}} = \frac{\frac{\partial n_{eff}}{\partial n_{bio}} \lambda}{n_g} \quad (2.26)$$

A rigorous derivation of the sensitivity of n_{eff} of slab waveguides for variations of the environment was performed by Tiefenthaler et al. in [102].

2.4.4 Vernier ring resonators

The ring resonator discussed above is the component used in its simplest form. Many other configurations containing multiple rings in e.g. a cascade or in combination with an MZI are possible and have been demonstrated [103, 104]. One of these configurations is two rings in a Vernier configuration. The principle is very similar to the Vernier scale found on e.g. micrometers or a calliper: by using two scales with a slightly different spacing (i.e. FSR), increased precision can be achieved. For ring resonators, this is illustrated in Figure 2.16.

The PhD work of Tom Claes [96] provides more in-depth information about Vernier ring resonators, as well as experimental data on such sensors, fabricated in SOI. It is shown that a significant improvement in sensitivity can be

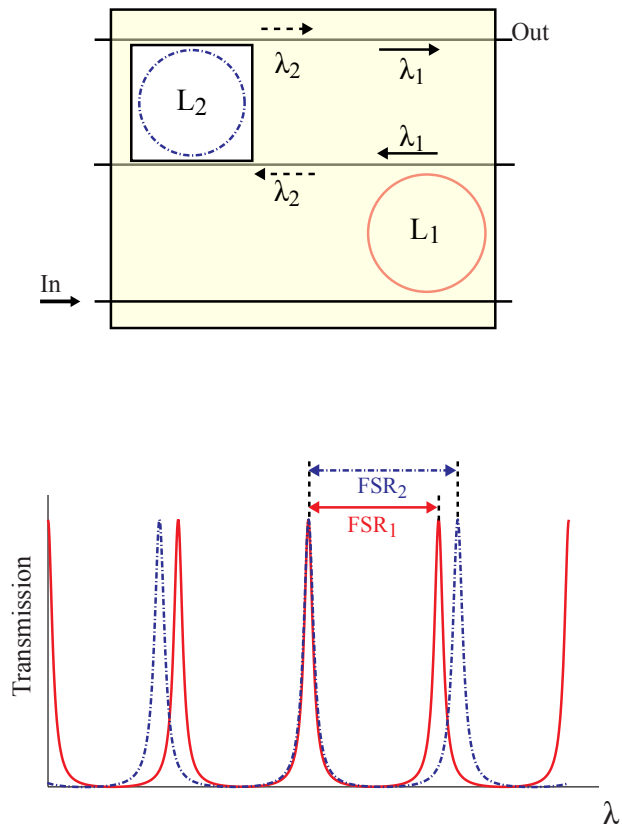


Figure 2.16: Broadband light is coupled in the top waveguide. When overlapping both transmission spectra of the slightly different rings, it is clear that one peak will, in theory, be completely transmitted while others will be attenuated. For a small shift in one of the ring spectra, a larger shift in the overall transmission spectrum can be obtained.

achieved, compared to a regular ring resonator. Furthermore, it is interesting to note that Vernier-cascade sensors exhibit an improved LOD over ring resonators [96]. Jin [105] has also published a Vernier-based sensor with a sensitivity of 1300 nm/RIU, below that of Claes [96] which is 2170 nm/RIU. In a recent article published by La Notte [106], a Vernier-configuration with a ring resonator and Mach-Zehnder interferometer is presented with a sensitivity of over 1000 μm /RIU.

2.5 Conclusions

We have given an introduction to the most common types of biosensors in mechanics, electronics and integrated photonics. Apart from the literature study, we have studied in detail one of the devices, ring resonators, which will be proposed as the main transducer for all three devices that we develop in the course of this PhD work. It is clear that each of the presented structures has its own advantages and disadvantages, but in the following chapters, we will make use of ring resonators in their simplest configuration, knowing that more complex configurations or elaborated designs could provide better performance for the platforms developed.

References

- [1] K. Marx. *Quartz crystal microbalance: a useful tool for studying thin polymer films and complex biomolecular systems at the solution-surface interface*. *Biomacromolecules*, 4(5):1099–120, 2003.
- [2] K. Länge, B. E. Rapp, and M. Rapp. *Surface acoustic wave biosensors: a review*. *Analytical and Bioanalytical Chemistry*, 391(5):1509–1519, July 2008.
- [3] A. Bardea, A. Dagan, I. Ben-dov, and I. Willner. *Amplified microgravimetric quartz-crystal-microbalance analyses of oligonucleotide complexes: a route to a Tay-Sachs biosensor device*. *Chemical Communications*, 12:839–840, 1998.
- [4] J. Wang, M. Jiang, T. W. Nilsen, and R. C. Getts. *Dendritic Nucleic Acid Probes for DNA Biosensors*. *American Chemical Society*, 120(32):8281–8282, 1998.
- [5] K. Niikura, K. Nagata, and Y. Okahata. *Quantitative Detection of Protein Binding onto DNA by Using a Quartz-Crystal Microbalance*. *Chemistry Letters*, pages 863–864, 1996.
- [6] T. Sato, M. Ishii, F. Ohtake, K. Nagata, T. Terabayashi, Y. Kawanishi, and Y. Okahata. *Binding affinity of GM3 lactone for influenza virus*. *Glycoconjugate Journal*, 16(3):223–7, March 1999.
- [7] J. Gimzewski, C. Gerber, E. Meyer, and R. Schlittler. *Observation of a chemical reaction using a micromechanical sensor*. *Chemical Physics Letters*, 217(5-6):589–594, January 1994.
- [8] Z. Guo, Q. Zhang, F. Dong, D. Chen, Z. Xiong, Z. Miao, C. Li, B. Jiao, and X. Wu. *Performance analysis of microcantilever arrays for optical readout uncooled infrared imaging*. *Sensors and Actuators A: Physical*, 137(1):13–19, June 2007.
- [9] Y. Ebara and Y. Okahata. *In situ surface-detecting technique by using a quartz-crystal microbalance. Interaction behaviors of proteins onto a phospholipid monolayer at the air-water interface*. *Langmuir The ACS Journal Of Surfaces And Colloids*, 9(2):574–576, 1993.
- [10] Q-sense, <http://q-sense.com/>.
- [11] N. V. Lavrik, M. J. Sepaniak, and P. G. Datskos. *Cantilever transducers as a platform for chemical and biological sensors*. *Review of Scientific Instruments*, 75(7):2229, 2004.

- [12] B. Ilic, D. Czaplewski, M. Zalalutdinov, H. G. Craighead, P. Neuzil, C. Campagnolo, and C. Batt. *Single cell detection with micromechanical oscillators*. Journal of Vacuum Science & Technology B: Microelectronics and Nanometer Structures, 19(6):2825, 2001.
- [13] T. Ivanov, T. Gotszalk, P. Grabiec, E. Tomerov, and I. W. Rangelow. *Thermally driven micromechanical beam with piezoresistive deflection readout*. Microelectronic Engineering, 68:550–556, 2003.
- [14] C. Ziegler. *Cantilever-based biosensors*. Analytical and Bioanalytical Chemistry, 379(7-8):946–59, August 2004.
- [15] Protiveris, <http://www.protiveris.com/>.
- [16] Concentris, <http://www.concentris.ch/>.
- [17] Bioscale, <http://www.bioscale.com/>.
- [18] F. Patolsky and C. M. Lieber. *Nanowire nanosensors*. Materials Today, April:20–28, April 2005.
- [19] F. Patolsky, G. Zheng, O. Hayden, M. Lakadamyali, X. Zhuang, and C. M. Lieber. *Electrical detection of single viruses*. Proceedings of the National Academy of Sciences of the United States of America, 101(39):14017–14022, September 2004.
- [20] E. Stern, R. Wagner, F. J. Sigworth, R. Breaker, T. M. Fahmy, and M. Reed. *Importance of the Debye screening length on nanowire field effect transistor sensors*. Nano Letters, 7(11):3405–3409, November 2007.
- [21] Z. Fan, J. C. Ho, Z. Jacobson, R. Yerushalmi, R. L. Alley, H. Razavi, and A. Javey. *Wafer-scale assembly of highly ordered semiconductor nanowire arrays by contact printing*. Nano letters, 8(1):20–5, January 2008.
- [22] J. Wang. *Nanomaterial-based electrochemical biosensors*. The Analyst, 130(4):421, 2005.
- [23] N. Sinha, J. Ma, and J. T. W. Yeow. *Carbon nanotube-based sensors*. Journal of Nanoscience and Nanotechnology, 6(3):573–590, March 2006.
- [24] F. Lisdat and D. Schäfer. *The use of electrochemical impedance spectroscopy for biosensing*. Analytical and Bioanalytical Chemistry, 391(5):1555–67, July 2008.
- [25] S. Duchateau, J. Broeders, D. Croux, J.-M. Rigo, P. Wagner, R. Thoelen, and W. De Ceuninck. *Cell proliferation monitoring by multiplexed electrochemical impedance spectroscopy on microwell assays*. Physica Status Solidi C, 2(5):882–888, 2013.

- [26] S. Schusser, M. Leinhos, M. Bäcker, A. Poghossian, P. Wagner, and M. J. Schöning. *Impedance spectroscopy: A tool for real-time in situ monitoring of the degradation of biopolymers*. *Physica Status Solidi A*, 210(5):905–910, 2013.
- [27] ACEA Bioscience, <http://www.aceabio.com/main.aspx>.
- [28] Applied BioPhysics, <http://www.biophysics.com/>.
- [29] M. C. Estevez, M. Alvarez, and L. M. Lechuga. *Integrated optical devices for lab-on-a-chip biosensing applications*. *Laser & Photonics Reviews*, 6(4):463–487, September 2011.
- [30] B. Liedberg, C. Nylander, and I. Lundstrom. *Surface plasmon resonance for gas detection and biosensing*. *Sensors and Actuators*, 4:299–304, 1983.
- [31] Biacore, <http://www.biacore.com>.
- [32] Xantec Bioanalytics, <http://www.xantec.com/>.
- [33] IBIS, <http://www.ibis-spr.nl/>.
- [34] Corning, <http://www.corning.com/lifesciences>.
- [35] A. Biosciences, <http://www.aceabio.com/>.
- [36] BioNavis, <http://www.bionavis.com/>.
- [37] V. Bronner, M. Edri, I. Zafir-Lavie, E. Rabkin, R. Luo, S. Nimri, and D. Shezifi. *The ProteOn HTE Sensor Chip: Novel Surface for Stable Capture of Histidine-Tagged Proteins for Protein-Small Molecule Interaction Analysis*. Technical report, Bio-Rad Laboratories, 2012.
- [38] J. Homola, S. S. Yee, and G. Gauglitz. *Surface plasmon resonance sensors: review*. *Sensors and Actuators B: Chemical*, 54(1-2):3–15, January 1999.
- [39] P. Debackere. *Nanophotonic Biosensor based on Surface Plasmon Interference*. PhD thesis, Ghent University, 2010.
- [40] G. Gupta and J. Kondoh. *Tuning and sensitivity enhancement of surface plasmon resonance sensor*. *Sensors and Actuators B: Chemical*, 122(2):381–388, March 2007.
- [41] A. A. Yanik, M. Huang, A. Artar, T.-Y. Chang, and H. Altug. *Integrated nanoplasmonic-nanofluidic biosensors with targeted delivery of analytes*. *Applied Physics Letters*, 96(021101):1–3, 2010.

- [42] J. Dostálek, J. Ctyroký, J. Homola, E. Brynda, M. Skalský, P. Někviňová, J. Spirková, J. Skvor, and J. Schröfel. *Surface plasmon resonance biosensor based on integrated optical waveguide*. Sensors and Actuators B, 76:8–12, 2001.
- [43] L. He, M. D. Musick, S. R. Nicewarner, F. G. Salinas, S. J. Benkovic, M. J. Natan, and C. D. Keating. *Colloidal Au-Enhanced Surface Plasmon Resonance for Ultrasensitive Detection of DNA Hybridization*. Journal of American Chemical Society, 122:9071–9077, 2000.
- [44] A. Suzuki, J. Kondoh, Y. Matsui, S. Shiokawa, and K. Suzuki. *Development of novel optical waveguide surface plasmon resonance (SPR) sensor with dual light emitting diodes*. Sensors and Actuators B: Chemical, 106:383–387, April 2005.
- [45] C. T. Campbell and G. Kim. *SPR microscopy and its applications to high-throughput analyses of biomolecular binding events and their kinetics*. Biomaterials, 28(15):2380–92, May 2007.
- [46] M. Piliarik and J. Homola. *Surface plasmon resonance (SPR) sensors: approaching their limits?* Optics express, 17(19):16505–17, September 2009.
- [47] R. G. Heideman and P. V. Lambeck. *Remote opto-chemical sensing with extreme sensitivity: design, fabrication and performance of a pigtailed integrated optical phase-modulated Mach-Zehnder interferometer system*. Sensors and Actuators B, 61:100–127, 1999.
- [48] F. Prieto, B. Sepúlveda, A. Calle, A. Llobera, C. Domínguez, and L. M. Lechuga. *Integrated Mach-Zehnder interferometer based on ARROW structures for biosensor applications*. Sensors and Actuators B: Chemical, 92:151–158, July 2003.
- [49] E. F. Schipper, A. M. Brugman, C. Domínguez, L. M. Lechuga, R. P. H. Kooyman, and J. Greve. *The realization of an integrated Mach-Zehnder waveguide immunosensor in silicon technology*. Sensors and Actuators B, 40:147–153, 1997.
- [50] B. H. Schneider, J. G. Edwards, and N. F. Hartman. *Hartman interferometer: versatile integrated optic sensor for label-free, real-time quantification of nucleic acids, proteins, and pathogens*. Clinical chemistry, 43(9):1757–63, September 1997.
- [51] X. Fan, I. M. White, S. I. Shopova, H. Zhu, J. D. Suter, Y. Sun, and J. D. Suter. *Sensitive optical biosensors for unlabeled targets: a review*. Analytica Chimica Acta, 620(1-2):8–26, July 2008.

- [52] A. Brandenburg and R. Henninger. *Integrated optical Young interferometer*. Applied Physics, 33(25):5941–5947, 1994.
- [53] A. Brandenburg. *Differential refractometry by an integrated-optical Young interferometer*. Sensors and Actuators B, 39:266–271, 1997.
- [54] Farfield Scientific, <http://www.farfield-group.com/>.
- [55] Silicon Kinetics, <http://www.siliconkinetics.com/>.
- [56] FortéBIO, <http://www.fortebio.com/>.
- [57] Biometrics. *Biometrics*.
- [58] B. Cunningham, P. Li, B. Lin, and J. Pepper. *Colorimetric resonant reflection as a direct biochemical assay technique*. Sensors and Actuators B, 81:316–328, 2002.
- [59] I. D. Block, N. Ganesh, M. Lu, and B. T. Cunningham. *A sensitivity model for predicting photonic crystal biosensor performance*. IEEE Sensors Journal, 8(3):274–280, 2008.
- [60] B. Cunningham and L. Laing. *Microplate-based, label-free detection of biomolecular interactions: applications in proteomics*. Expert Reviews of Proteomics, 3(3):271–281, 2006.
- [61] M. R. Lee and P. M. Fauchet. *Two-dimensional silicon photonic crystal based biosensing platform for protein detection*. Optics Express, 15(8):4530–4535, April 2007.
- [62] Sheffield Centre for Electron Beam Lithography, <http://sheffieldebeam.com/>.
- [63] M. Huang, A. A. Yanik, T.-Y. Chang, and H. Altug. *Sub-wavelength nanofluidics in photonic crystal sensors*. Optics Express, 17(26):24224–24233, December 2009.
- [64] B. T. Tung, D. V. Dao, T. Ikeda, Y. Kanamori, and K. Hane. *Investigation of strain sensing effect in modified single-defect photonic crystal nanocavity*. Optics Express, 19(9):8821–8829, 2011.
- [65] Y. Liu and H. W. M. Salemink. *Photonic crystal-based all-optical on-chip sensor*. Optics Express, 20(18):19912, August 2012.
- [66] O. Painter, A. Husain, A. Scherer, P. T. Lee, I. Kim, J. D. O’Brien, and P. D. Dapkus. *Lithographic tuning of a two-dimensional photonic crystal laser array*. IEEE Photonics Technology Letters, 12(9):1126–1128, September 2000.

- [67] H.-G. Park, S.-H. Kim, M.-K. Seo, Y.-G. Ju, S.-B. Kim, and Y.-H. Lee. *Characteristics of electrically driven two-dimensional photonic crystal lasers*. Ieee Journal of Quantum Electronics, 41(9):1131–1141, 2005.
- [68] Y. Chassagneux, R. Colombelli, W. Maineults, S. Barbieri, S. P. Khanna, E. H. Linfield, and A. G. Davies. *Predictable surface emission patterns in terahertz photonic-crystal quantum cascade lasers*. Optics Express, 17(12):9491–9502, June 2009.
- [69] F. Villa and J. Gaspar-Armenta. *Photonic crystal to photonic crystal surface modes: narrow-bandpass filters*. Optics Express, 12(11):2338–2355, May 2004.
- [70] E. Drouard, H. Hattori, C. Grillet, A. Kazmierczak, X. Letartre, P. Rojo-Romeo, and P. Viktorovitch. *Directional channel-drop filter based on a slow Bloch mode photonic crystal waveguide section*. Optics Express, 13(8):3037–3048, April 2005.
- [71] M. Davanço, A. Xing, J. W. Raring, E. L. Hu, and D. J. Blumenthal. *Compact Broadband Photonic Crystal Filters With Reduced Back-Reflections for Monolithic InP-Based Photonic Integrated Circuits*. IEEE Photonics Technology Letters, 18(10):1155–1157, 2006.
- [72] Y. Zhao, X. Zhao, and Z. Gu. *Photonic crystals in bioassays*. Advanced Functional Materials, 20(18):2970–2988, September 2010.
- [73] J. Voros, J. Ramsden, G. Csúcs., I. Szendro, S. D. Paul, M. Textor, and N. Spencer. *Optical grating coupler biosensors*. Biomaterials, 23:3699–3710, 2002.
- [74] P. Nellen, K. Tiefenthaler, and W. Lukosz. *Integrated optical input grating couplers as biochemical sensors*. Sensors and Actuators, 15:285–295, 1988.
- [75] W. Lukosz, D. Clerc, P. M. Nellen, C. Stamm, and P. Weiss. *Output grating couplers on planar optical waveguides as direct immunosensors*. Biosensors & bioelectronics, 6(3):227–32, January 1991.
- [76] M. Wiki and R. E. Kunz. *Wavelength-interrogated optical sensor for biochemical applications*. Optics Letters, 25(7):463–5, April 2000.
- [77] SRU Biosystems, <http://www.srubiosystems.com>.
- [78] D. Rabus. *Integrated ring resonators*, volume 127 of *Springer Series in Optical Sciences*. Springer Berlin Heidelberg, Berlin, Heidelberg, springer s edition, 2007.

- [79] W. Bogaerts, P. De Heyn, T. Van Vaerenbergh, K. De Vos, S. Kumar Selvaraja, T. Claes, P. Dumon, P. Bienstman, D. Van Thourhout, and R. Baets. *Silicon microring resonators*. *Laser and Photonics Reviews*, pages 1–27, September 2011.
- [80] B. E. Little, J. S. Foresi, G. Steinmeyer, E. R. Thoen, S. T. Chu, H. A. Haus, E. P. Ippen, L. C. Kimerling, and W. Greene. *Ultra-compact Si-SiO₂ microring resonator*. *IEEE Photonics Technology Letters*, 10(4):549–551, 1998.
- [81] F. Xia, L. Sekaric, and Y. Vlasov. *Ultracompact optical buffers on a silicon chip*. *Nature Photonics*, 1(1):65–71, January 2007.
- [82] B. R. Koch, A. W. Fang, O. Cohen, and J. E. Bowers. *Mode-locked silicon evanescent lasers*. *Optics Express*, 15(18):11225–33, September 2007.
- [83] Q. Xu, S. Manipatruni, B. Schmidt, J. Shakya, and M. Lipson. *12.5 Gbit/s carrier-injection-based silicon micro-ring silicon modulators*. *Optics Express*, 15(2):430–436, 2007.
- [84] R. W. Boyd and J. E. Heebner. *Sensitive disk resonator photonic biosensor*. *Applied Optics*, 40(31):5742–7, November 2001.
- [85] A. Ramachandran, S. Wang, J. Clarke, S. J. Ja, D. Goad, L. Wald, E. M. Flood, E. Knobbe, J. V. Hryniewicz, S. T. Chu, D. Gill, W. Chen, O. King, and B. E. Little. *A universal biosensing platform based on optical micro-ring resonators*. *Biosensors & Bioelectronics*, 23(7):939–944, February 2008.
- [86] C.-Y. Chao, W. Fung, and L. J. Guo. *Polymer microring resonators for biochemical sensing applications*. *IEEE Journal of Selected Topics in Quantum Electronics*, 12(1):134–142, January 2006.
- [87] K. De Vos, I. Bartolozzi, E. Schacht, P. Bienstman, and R. Baets. *Silicon-on-Insulator microring resonator for sensitive and label-free biosensing*. *Optics Express*, 15(12):7610–7615, June 2007.
- [88] K. De Vos, J. Girones, T. Claes, Y. De Koninck, S. Popelka, E. Schacht, R. Baets, and P. Bienstman. *Multiplexed antibody detection with an array of Silicon-on-Insulator microring resonators*. *IEEE Photonics Journal*, 1(4):225–235, 2009.
- [89] Genalyte, <http://www.genalyte.com/>.
- [90] M. S. Luchansky, A. L. Washburna, T. A. Martina, M. Iqbalb, L. Gunn, and R. C. Bailey. *Characterization of the evanescent field profile and bound mass sensitivity of a label-free silicon photonic microring resonator biosensing platform*. *Biosensors & Bioelectronics*, 26(4):1283–1291, 2010.

- [91] A. L. Washburn, L. C. Gunn, and R. C. Bailey. *Label-free quantitation of a cancer biomarker in complex media using silicon photonic microring resonators*. *Analytical Chemistry*, 81(22):9499–9506, 2009.
- [92] A. L. Washburn, M. S. Luchansky, A. L. Bowman, and R. C. Bailey. *Quantitative, label-free detection of five protein biomarkers using multiplexed arrays of silicon photonic microring resonators*. *Analytical Chemistry*, 82(1):69–72, 2011.
- [93] A. L. Washburn and R. C. Bailey. *Photonics-on-a-Chip: Recent advances in integrated waveguides as enabling detection elements for real-world, Lab-on-a-Chip biosensing applications*. *Analyst*, 136(2):227–236, 2011.
- [94] M. S. McClellana, L. L. Domierb, and R. C. Bailey. *Label-free virus detection using silicon photonic microring resonators*. *Biosensors & Bioelectronics*, 31(1):388–392, 2012.
- [95] A. J. Qavi, J. T. Kindt, M. A. Gleeson, and R. C. Bailey. *Anti-DNA:RNA antibodies and silicon photonic microring resonator arrays enable the ultrasensitive, multiplexed detection of microRNAs*. *Analytical Chemistry*, 83(15):5949–5956, 2011.
- [96] T. Claes. *Advanced silicon photonic ring resonator label-free biosensors*. PhD thesis, Ghent University, 2012.
- [97] K. De Vos. *Label-free Silicon Photonics Biosensor Platform with Microring Resonators*. Phd dissertation, Ghent University, Ghent, 2010.
- [98] J. E. Heebner, R. Grover, and T. Ibrahim. *Optical microresonators*. Springer Berlin Heidelberg, 2008.
- [99] L. B. Soldano and E. C. M. Pennings. *Optical Multi-Mode Interference devices based on self-imaging: principles and applications*. *Journal of Lightwave Technology*, 13(4):615–627, 1995.
- [100] S. K. Selvaraja, P. Jaenen, W. Bogaerts, D. V. Thourhout, P. Dumon, and R. Baets. *Fabrication of photonic wire and crystal circuits in Silicon-on-Insulator using 193nm optical lithography*. *Journal of Lightwave Technology*, 27(18):4076–4083, 2009.
- [101] S. K. Selvaraja. *Wafer-scale fabrication technology for silicon photonic integrated circuits*. PhD thesis, Ghent University, 2011.
- [102] K. Tiefenthaler and W. Lukosz. *Sensitivity of grating couplers as integrated-optical chemical sensors*. *Journal of the Optical Society of America B*, 6(2):209–220, 1989.

-
- [103] X. Li, Y. Su, Z. Zhang, M. Qiu, and S. Qin. *Label-free Biosensor Based on Silicon-On-Insulator Concentric Micro-Ring Resonators*. In 2008 IEEE PhotonicsGlobal, pages 1–3, Singapore, December 2008. IEEE.
- [104] M. Terrel, M. J. F. Digonnet, and S. Fan. *Ring-coupled Mach-Zehnder interferometer optimized for sensing*. Applied Optics, 48(26):4874–4879, September 2009.
- [105] L. Jin, M. Li, and J. He. *Highly-sensitive Silicon-on-Insulator sensor based on two cascaded micro-ring resonators with vernier effect*. Optics Communications, 284(1):156–159, January 2011.
- [106] M. La Notte and V. M. N. Passaro. *Ultra high sensitivity chemical photonic sensing by Mach-Zehnder Interferometer enhanced vernier-effect*. Sensors and Actuators B: Chemical, 176:994–1007, October 2013.

3

SOI microring resonator sensor integrated on the fiber facet

A lot of progress has been made to implement the label-free sensors mentioned in Chapter 2 in small and easy-to-use cartridges. However, many applications still require a sensor that can perform measurements at locations that are hard to reach.

Optical fiber sensors can be used to tackle difficult measurement situations where the use of conventional sensors is not appropriate. They are usually compact and lightweight, minimally invasive, and can be multiplexed effectively on a single fiber network. An additional advantage of optical fiber sensors is that they are insensitive to electromagnetic interference, since there are no electrical currents flowing at the sensing point.

The purpose of this chapter is to outline the basics of optical fiber biosensors and recent developments in the label-free biosensing technology. Specifically we will describe in detail an optical fiber probe sensor for label-free biosensing based on an SOI ring resonator as transducer of the sensing device. Its use as a medical device for imaging hard-to-reach locations and its ability to transport light to a remote convenient location make of it a suitable tool for in-vivo sensing applications, such as endoscopy.

In the first section we will introduce the most important fiber sensor technologies for label-free biosensing. After this we will start describing our fiber

probe. In Section 3.2, the design of the photonic circuit to be transferred to the fiber facet will be described in detail. Two different fabrication routes will be discussed in Section 3.3. We will characterize our device in Section 3.4 where the experiments performed and the results are analyzed and we will finalize the chapter with the conclusions.

3.1 Optical fiber sensors

The application of optical fiber technology for sensing has undergone tremendous growth and advancement over the last years and this is related to two of the most important scientific advances of the 1960s, the laser (1960) and modern low-cost optical fibers (1966) [1]. During the late 1960s and early 1970s some of these low-loss optical fibers were used in the development of the first chemical sensors; since then, their application has continued to progress and spread to very different areas, e.g. clinical, environmental, industrial, food, and military applications [2–5].

An optical fiber is a cylindrical waveguide made from silica or plastic that guides light along its axis, by the process of total internal reflection (TIR). A fiber consists of a dielectric material (the core) surrounded by another dielectric material with a lower refractive index (the cladding). For light propagation by TIR the refractive index of the core (n_1) must be larger than that of the cladding (n_2), i.e. $n_1 > n_2$. When a ray of light strikes the boundary interface between these transparent media of different refractive index and the angle of incidence is larger than the critical angle, defined by Snell's law, ($\theta_c = \arcsin(n_2/n_1)$), it will be totally internally reflected and propagated through the fiber (see Figure 3.1). However, its intensity does not abruptly decay to zero at the interface. A small portion of light penetrates the reflecting medium by a fraction of the wavelength, far enough to sense a change in refractive index. This electromagnetic field, called the evanescent wave, has an intensity that decays exponentially with distance, starting at the interface and extending into the medium of lower refractive index. The penetration depth, defined as the distance required for the electric field amplitude to fall to $1/e$ (0.37) of its value at the interface, increases with decreasing index contrast and is also a function of the wavelength of the light and the angle of incidence.

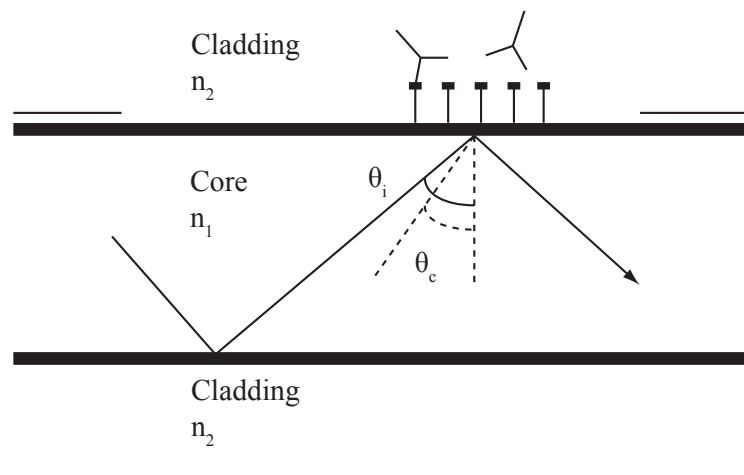


Figure 3.1: For light propagation by total internal reflection the refractive index of the core optical fiber core n_1 must be larger than that of the cladding n_2 . In tapered fibers, the evanescent field can interact with the surrounding environment, i.e. for detection of molecules.

In a standard fiber where the cladding is much thicker than the core, the evanescent field decays to near zero value at the fiber surface. However, if the fiber is tapered down to a diameter close to the core diameter, the light is no longer guided by the core but is guided by the cladding, and the evanescent field will interact with the surrounding environment, i.e. it can interact with molecules within the new penetration depth.

Optical fiber biosensors can be classified into two categories: intrinsic and extrinsic sensors. In an intrinsic sensor, the interaction with the analyte occurs within an element of the optical fiber whereas in an extrinsic sensor the optical fiber is only used to couple light. They can be used in combination with different types of optical techniques (e.g. absorbance, refractive index, fluorescence, chemiluminescence measurements and other spectroscopic techniques) [6]. In all instances light intensity, decay time, polarization or phase of the emitted radiation can be selected as the analytical property used to evaluate the concentration of the analyte.

Here we will only focus on optical fiber sensors used for label-free biosensing. For more details we refer to [7].

3.1.1 Fiber Bragg gratings

Fiber Bragg gratings (FBGs) are currently among the most popular of all fiber-based optical sensors for analyzing load, strain, temperature, vibration, and refractive index (RI) [8, 9].

They are periodic structures that are imprinted directly into the core region of optical fibers by UV radiation. Such structures consist of a periodically varying refractive index, typically over several millimeters of the fiber core. The specific characteristic of fiber Bragg gratings for sensing applications is that their periodicity causes them to act as wavelength sensitive reflectors. Light traveling down the fiber is partially reflected at each of the small refractive index variations. However, at a particular wavelength, called the Bragg wavelength, (λ_B) [10]:

$$\lambda_B = 2 \cdot n_{eff} \cdot \Lambda \quad (3.1)$$

where n_{eff} is the effective refractive index encountered by the fiber core mode and Λ the grating period, the reflections from each successive period are in phase (constructive interference) and light is reflected back up the fiber. By monitoring shifts of the Bragg wavelength, the device functions as a refractive index sensor, which can be used for biochemical sensing. The major advantages of the fiber Bragg grating technology are minimal size, ease of multiplexing and distributed sensing possibilities [9].

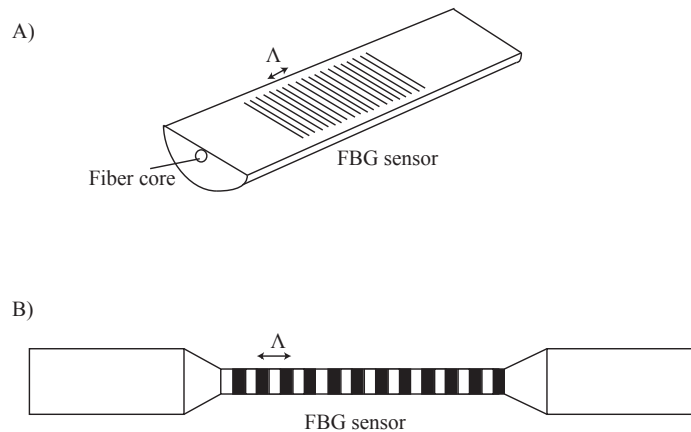


Figure 3.2: A) A surface grating is created on the side of the fiber. This usually requires bending and polishing until the fiber's core is exposed and then a grating is physically patterned on that surface. B) The optical fiber is chemically etched down to its core where the grating is patterned.

In order to expose the evanescent field from the FBG, several strategies have been pursued as illustrated in Figure 3.2. One approach is to create a surface grating on the side of the fiber [11–13]. This usually requires bending and polishing until the fiber's core is exposed, and then a grating is physically patterned on that surface. This design has yielded devices with a RI sensitivity as high as 340 nm RIU^{-1} and a LOD down to $2 \times 10^{-6} \text{ RIU}$ [13].

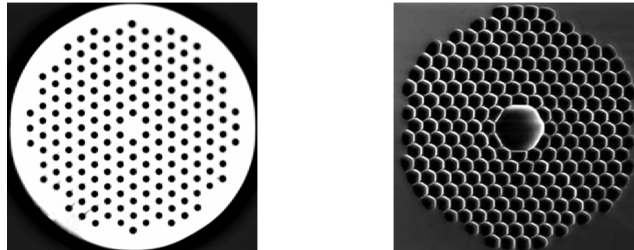


Figure 3.3: Photonic Crystal Fibers (PCF). The unique light-guiding mechanism of photonic crystal fibers ensures a strong light-matter interaction because of the large light-sample overlap since the air holes in the fiber can act as a simple fluidic channel to deliver the biological samples.

Another way of exposing the evanescent field involves chemically etching the optical fiber down to its core [14–17]. Chryssis et al. demonstrated a RI sensitivity of 1394 nm RIU^{-1} with a LOD of $7 \times 10^{-6} \text{ RIU}$ when the fiber was etched down to $3.4 \mu\text{m}$ in diameter [16]. Using the same sensor, $0.7 \mu\text{g mL}^{-1}$ target DNA was detected with 20 base pairs, which corresponds roughly to $0.1 \mu\text{M}$ [16]. This is still substandard for label-free DNA detection, but it appears to be only the first proof of concept on this work.

In another study, light-matter interaction was increased by inscribing FBGs into a microstructured fiber or Photonic Crystal Fiber (PCF) [18] (Figure 3.3). PCF is a promising sensing platform for two reasons. First, the air holes in the fiber can act as a simple fluidic channel to deliver the biological samples. Second, the unique light-guiding mechanism of photonic crystal fibers ensures a strong light-matter interaction because of the large light-sample overlap. The array of air holes may hold a sample volume of a few nL per cm of the fiber, which is a desirable advantage for biosensing applications. Phan Huy et al. has reported a detection of $6 \times 10^{-6} \text{ RIU}$ using this technique. [18]

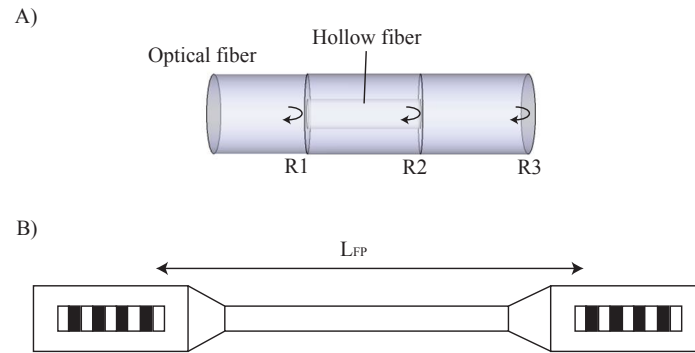


Figure 3.4: A) Fiber Fabry-Perot cavity sensor showing the hollow segment. B) A fiber Fabry-Perot cavity formed by two sets of FBGs.

Another structure of interest is a fiber Fabry-Perot cavity-based sensor formed by a short piece of hollow fiber, a slot sandwiched between two pieces of optical fiber, or a pair of FBGs [19–22]. It can also be formed by a piece of tapered fiber between a pair of FBGs (Figure 3.4). The spectral reflectance of these devices is sensitive to the RI near the fiber tip or the fiber taper. A RI sensitivity of 71.2 nm RIU^{-1} and a LOD of 1.4×10^{-5} RIU were demonstrated with a 5 mm long tapered fiber cavity [14].

3.1.2 Long-period gratings

Long-period gratings (LPGs), have attracted a great deal of attention in recent years for biochemical sensing applications although the advantages of LPGs have been known since the early 1990s [23, 24]. These devices are manufactured with a periodicity in the order of 100 μm to 1 mm, three or four orders of magnitude larger than traditional FBGs. In an LPG, core modes couple into the cladding modes of the fiber [25] so the characteristic resonance condition is expressed differently than for FBG [26]:

$$\lambda_B = (n_{eff_{core}} - n_{eff_{cladding}})\Lambda \quad (3.2)$$

where $n_{eff_{core}}$ is the effective RI encountered by core modes, and $n_{eff_{cladding}}$ is the effective RI encountered by cladding modes, which is affected by the external refractive index. Because of this increased field intensity in the cladding of the fiber, the spectral position of the reflection peak becomes more sensitive to the RI change in the surrounding medium [27]. These sensors therefore have the advantage of being able to sense the RI changes around the cladding without etching or complex structural design. Due to the large grating pitch, they are also far easier to manufacture.

LPGs can also be customized by chemically etching down the cladding material in order to enhance the sensitivity [25, 28]. For example, in [28], a sensitivity of 172 nm RIU^{-1} was reached by using this method.

Recently, Rindorf et al. demonstrated the detection of biomolecules using a long-period grating in a PCF [29, 30].

Coupled optical fibers or fiber couplers, shown in Figure 3.5, are another fiber-based biochemical sensor platform. In this case, two identical optical fibers are fused together and tapered to a diameter of 9 μm . The transmission spectrum is sinusoidal and shows a RI sensitivity close to 70 nm RIU^{-1} with a LOD of 4×10^{-6} RIU [31]. Tazawa et al. demonstrated this sensor's ability to detect streptavidin with concentrations between 0.5 and 2 $\mu\text{g mL}^{-1}$ using covalent surface chemistries.

3.1.3 SPR fiber sensors

In Chapter 2, we mentioned that prism coupling is the most convenient SPR configuration and generally has the best sensing LOD. However, the prism is bulky and difficult to integrate. Optical fibers offer a good alternative to the prism, providing a possibility for sensor miniaturization and an extremely simplified optical design. They are very attractive for remote sensing and in-vivo applications; therefore they have been extensively studied in recent years.

The use of optical fibers for SPR sensing was first proposed by Jorgenson and Yee et al. [32]. They used the wavelength interrogation technique and formed

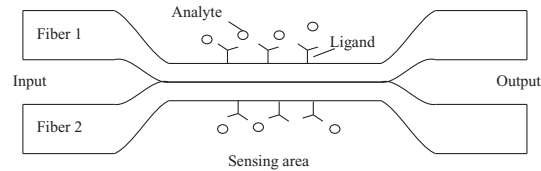


Figure 3.5: Coupled fibers are another fiber-based biochemical sensor platform. Two identical optical fibers are fused together and tapered [31].

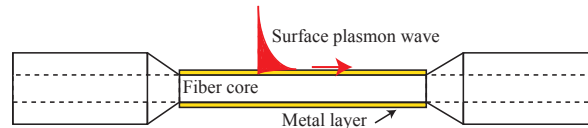


Figure 3.6: Jorgenson and Yee et al. [32] used a side polished fiber where a metal layer was deposited symmetrically around the exposed section of the fiber core.

an SPR-sensing structure by using a conventional polymer clad silica fiber with partly removed cladding and an SPR active metal layer deposited symmetrically around the exposed section of the fiber core (Figure 3.6). This approach allows the fabrication of miniaturized optical fiber SPR probes with limited interaction area. The fiber-optic SPR sensor is capable of detecting variations in the refractive index within the operating range between 1.2 and 1.4 RIU with a resolution of up to 5×10^{-5} RIU at higher refractive indices of analyte with a resonant wavelength resolution of 0.5 nm.

Several different fiber-optic SPR biosensor configurations have been developed based on side-polished single-mode fiber [32, 33], side-polished multi-mode fiber [34], polarization maintaining fiber [35] and D-shaped fiber [36], all with a typical LOD of around 10^{-5} to 10^{-6} RIU. This can be slightly improved by using additional Bragg gratings [37] or tapering of the fiber core [38].

There is a strong belief in literature [39, 40], that the key towards better fiber optic SPR biosensors is controlling the chemical interactions on the sensor surface. Pollet et al. [41] presented the first report on fiber optic SPR using DNA aptamers as bioreceptors based on the original design of Jorgenson and Yee [32].

Two years later, he presented the first real-time monitoring of DNA amplification using the same device [42].

3.2 Design of the optical circuit to be transferred on the fiber facet

FBG and LPG sensors are very attractive due to their simple design, low manufacturing costs, and high compatibility with standard optical fibers. Most applications, however, focus on physical and basic RI sensing, because they lend themselves so readily to these purposes. For biochemical detection, these sensors cannot compete with other types of optical sensors in terms of their LODs even though their sensitivities can exceed 100 nm RIU^{-1} .

The main motivation of this section is to combine the good performance of photonic biosensors on chip with the advantages that optical fibers offer, such as portability, flexibility, low cost, and an excellent light delivery to a remote convenient location, creating a so-called "lab-on-fiber".

We will transfer a photonic structure to the fiber tip which consists of two parts: the grating coupler and the sensing circuit. We will now discuss each of these components in more detail.

3.2.1 Grating couplers

We will start with an essential and non-trivial task for any silicon photonic sensor: how to couple the light from an optical fiber with a core diameter of about $10 \mu\text{m}$ into a typical waveguide dimension ($220\text{nm} \times 450\text{nm}$). The size mismatch of a few orders of magnitude between the fiber core and a photonic wire makes this coupling very inefficient. For years this problem has been investigated thoroughly in literature [43–49] and tackled with different mechanisms. The use of grating couplers is one of the most elegant methods.

Here we briefly overview the working principle of a one-dimensional grating coupler, since it is a substantial part of the optical circuit used in our sensor probe.

Waveguide gratings are structures having a periodic modulation of the refractive index, see Figure 3.7. According to the Bragg condition, this one-dimensional periodic structure will allow power exchange between particular modes of the structure. For each grating a K-vector along the direction of periodicity can be defined with magnitude:

$$K = \frac{2\pi}{\Lambda} \quad (3.3)$$

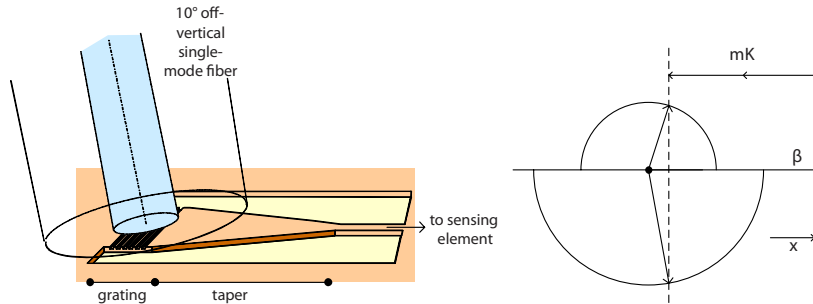


Figure 3.7: Left: Light is coupled from the fiber to the photonic circuit by means of the grating couplers from [50]. Right: Bragg condition for one-dimensional periodic structure.

in which Λ is the period of the grating. The fundamental waveguide mode with propagation constant β couples to other modes with k_x vectors given by the Bragg condition:

$$k_x = -\beta + mK \quad (3.4)$$

with $m = \dots, -2, -1, 0, 1, 2, \dots$. From the vector diagram it is clear that vertical coupling through a grating coupler will go hand in hand with a large second order reflection back into the waveguide. To avoid this, the gratings are designed for slightly off-vertical coupling. In order to optimize the coupling efficiency, the overlap between the field profiles of an optical fiber and the upwards diffracted field profile is maximized. An extensive analysis of the design of grating couplers is given by Taillaert in [44] and by Tamir in [43].

In [45], these gratings show 33% coupling efficiency at a 1.55- μm wavelength, 40-nm 1-dB bandwidth and 2- μm alignment tolerance for 1-dB excess loss. Typically these gratings measure 10 μm x 10 μm and are defined in a 10- μm wide waveguide, guaranteeing that most of the light is collected and changed from the vertical to the horizontal direction. However it still has to be converted from a 10- μm broad to a 450-nm broad waveguide. This is done by using an adiabatic taper, lengthening the structure with at least 150 μm .

This adiabatic transition determines the length of the coupling structure between fiber and chip. An alternative is to focus the light, which would alleviate the need for this long adiabatic transition and would result in a substantial length decrease, and hence a higher degree of integration. Additionally, light could be focused directly on an integrated component, without needing a waveguide. In [47] Van Laere demonstrates focusing grating coupler structures in SOI. The focusing grating couplers perform equally well compared to the previously mentioned linear gratings. The fiber-to-fiber loss is 10.5 dB, cor-

responding to a coupling efficiency of a single grating coupler around 30%. The most compact structure of this type has a total footprint of $18.5 \mu\text{m}$ (width of the grating) by $28 \mu\text{m}$ (grating + focusing section).

We will use these focusing grating couplers to couple the light from the fiber to the sensor circuit, since the space available is limited by the dimensions of a monomode fiber facet.

3.2.2 Sensing circuit

Our photonic device is composed of typically 220 nm high and 450 nm wide photonic wires with 2.7 dB/cm propagation loss, on top of $2 \mu\text{m}$ of silicon oxide and $750 \mu\text{m}$ silicon substrate.

In order to fit on the facet of a standard single-mode optical fiber, the photonic circuit is required to be compact. Therefore it is designed to be 'retro-reflective': using a dedicated light coupling scheme, light will be coupled in and out of the integrated circuit via the same grating coupler and under the same angle, similar to the work presented in [51].

Figure 3.8 shows a schematic of the top view of the optical fiber probe with the photonic integrated circuit aligned to the core of the optical fiber. The cladding of the fiber carries the rest of the integrated circuit comprising a 3dB multimode interference (MMI) splitter/combiner and a ring resonator biosensor. A focusing curved grating coupler focuses the light onto the SOI waveguide, which as already mentioned circumvents the need for space-consuming waveguide tapers. [47].

The 3-dB MMI coupler splits the incoupled light into two different waveguides which coincide with both access waveguides of an add-drop ring resonator. Two inverted tapers at the end of these waveguides prevent light not coupled in the ring from being reflected back in the waveguides and the ring.

The microring is a compact racetrack shape with $4 \mu\text{m}$ bend radius and $4 \mu\text{m}$ straight sections that are used as directional couplers with a gap of 180 nm between the waveguides. The ring supports modes that resonate at a wavelength λ_{res} (equation 2.5). At this wavelength, both the clockwise and the counter-clockwise resonance mode will be excited, causing light to be coupled back in the access waveguides.

The same MMI is used to combine the reflected light, i.e. only wavelengths near the resonance of the ring resonator, towards the grating coupler and the optical fiber. In this way, the circuit is retro-reflective for only the dropped wavelengths.

Light coupled back in the optical fiber will show sharp peaks in the spectrum corresponding to the resonance wavelengths. When biomolecular interaction takes place in the vicinity of the ring sensor, these resonances will shift,

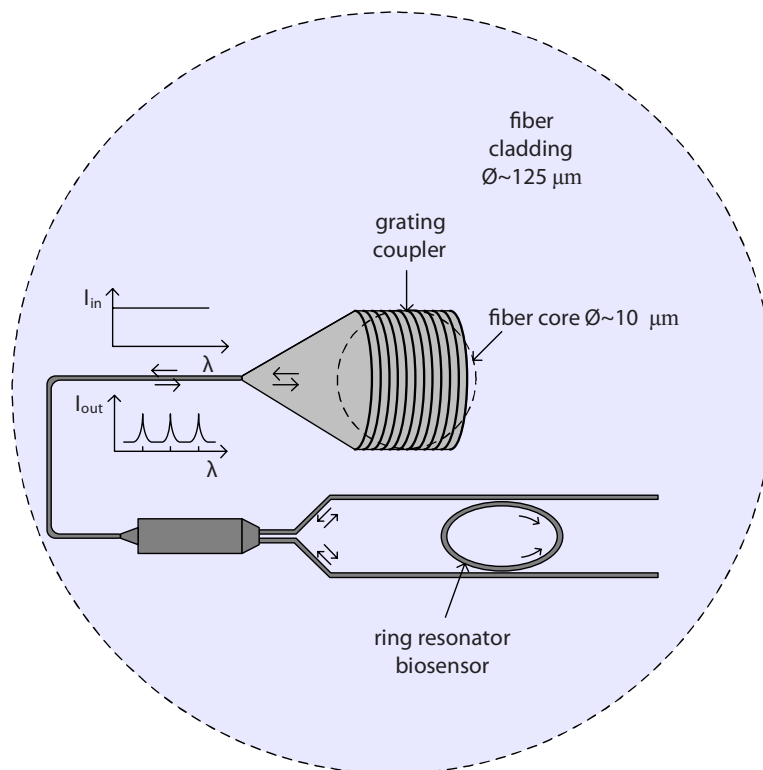


Figure 3.8: Schematic of the top view of the optical fiber probe with the photonic circuit aligned to the core of the fiber.

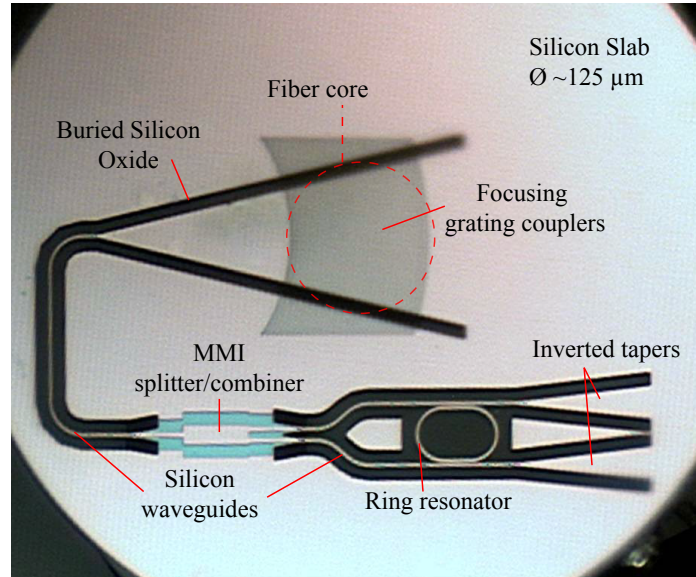


Figure 3.9: Microscope picture of the fiber probe facet with the photonic circuit aligned to the core of the fiber.

quantifying the number of binding events on the sensor surface.

3.3 Transfer of the photonic chip to the fiber facet

We investigated several routes for the fabrication of the device. Two main routes are described in detail in the following subsections.

3.3.1 Route 1: failed

This route consists basically of detaching a membrane with the photonic sensing circuit and gluing this membrane to the fiber. Figure 3.10 gives an overview of the fabrication steps followed in this route.

In order to create a membrane, first the photonic circuit needs to be coated with a photoresist, in this case, by making use of a thin spin-coated SU-8 layer, a commonly used epoxy-based negative photoresist. Subsequently a lithography step needs to be performed in order to open a window in the SU-8 layer to be able to access the buried oxide (BOX) underneath the photonic circuit, which is meant to be underetched.

The underetching process is done by wet etching. Wet etching of silicon dioxide can be done isotropically by using either concentrated hydrofluoric acid

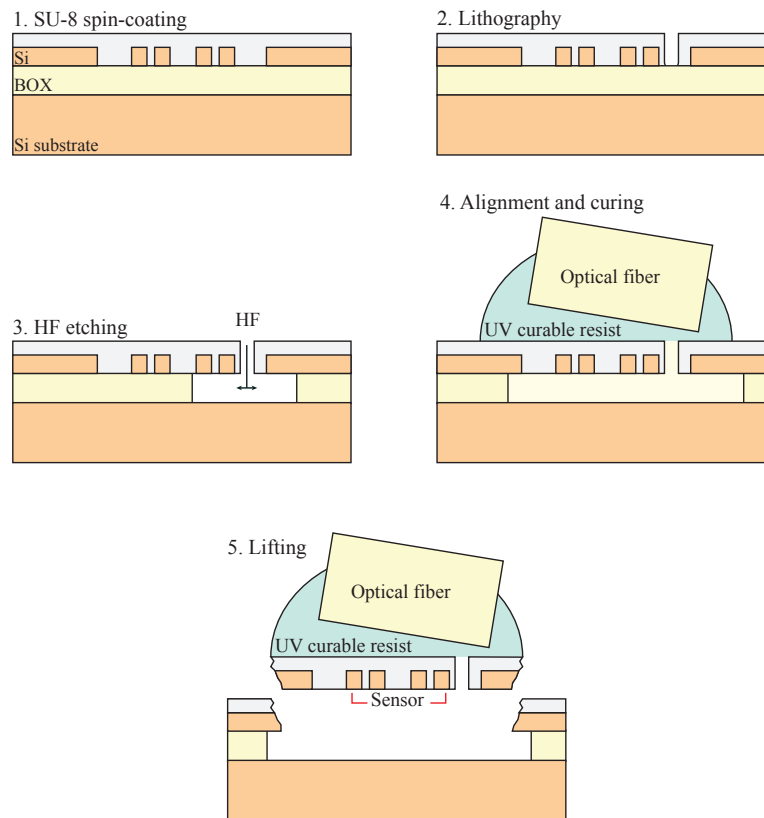


Figure 3.10: Route 1: Fabrication steps. All the illustrations represent the cross-section of the SOI chip and optical fiber. (1) A thin layer of SU-8 is spin-coated on the sensor surface. (2) Lithography is performed to open a window through the SU-8 layer. (3) The sample is immersed in HF. This will etch the buried silicon oxide (BOX) under the sensor through the SU-8 window. (4) The fiber is actively aligned with an angle of 10° off the vertical axis to obtain optimal coupling and an ultraviolet (UV) curable resist is used to glue fiber and chip together. (5) Lifting the fiber carefully, the SU-8 membrane breaks around the sensor under the weight of the remaining part of the photonic chip, leaving only the sensor circuit on the tip of the fiber.

(HF) (typically 49% HF in water) or buffered oxide etch (BOE) which is basically a mixture of a buffering agent such as ammonium fluoride (NH_4F) and HF (typically with a volume ratio 6:1). Logically, the etch rate of the first option is much higher than that of the second one, which instead offers a more controllable etching.

We make use of the first option, since our application does not require a precise control of the etching process. However, after 30 min of immersion in HF (time required to underetch the whole structure $\sim 125 \mu\text{m}$), we observe peeling of the SU-8 layer from the surface. This problem is solved by a short dip (5 seconds) of the SOI sample in HF before coating the SU-8 layer on top. With this previous step we etch away the native silicon oxide on top of the silicon structures, hence improving the adhesion of SU-8 to the surface and avoiding peeling of SU-8 in the wet etching step.

At this stage, the membrane is created and the photonic structure is suspended in air by the SU-8 layer. The optical fiber is aligned to the grating coupler in an active way applying PAK-01 (a curable resist by Toyo Gosei Co. with a refractive index very similar to SU-8) on the fiber tip. Since the light doesn't travel through an air layer anymore, the index contrast between the incident medium and SU-8 is decreased, optimizing the transmission.

In a final step, the PAK-01 is cured by exposing it to UV light. Fiber and membrane are glued together, but they are still attached to the photonic chip. By lifting the fiber carefully, the SU-8 membrane breaks around the sensor under the weight of the remaining part of the photonic chip, leaving only the sensor circuit on the tip of the fiber.

Numerous problems were encountered in the active alignment stage. It seemed difficult to maintain the membrane in a horizontal position and consequently also the 10° angle for optimal coupling efficiency between fiber and grating coupler.

In Figure 3.11 (top) an SEM picture shows the inclination of the grating couplers after being underetched, when the membrane is pending on air. At the bottom we observe the same structure, however, no air can be observed between the silicon grating couplers and the silicon substrate: the membrane has collapsed.

Two major difficulties arose using this process: first, the alignment of the fiber under the correct angle was a very tough task, second, if both, silicon substrate and silicon circuit, have stuck together like in Figure 3.11 (bottom), trying to detach them results in images like in Figure 3.12, where some parts of the photonic circuit are attached to the fiber facet (left) and some other parts remain on the SOI chip (right).

An exhaustive study on the optimal thickness of the SU-8 membrane to avoid the collapse was performed without success, and other alternative routes

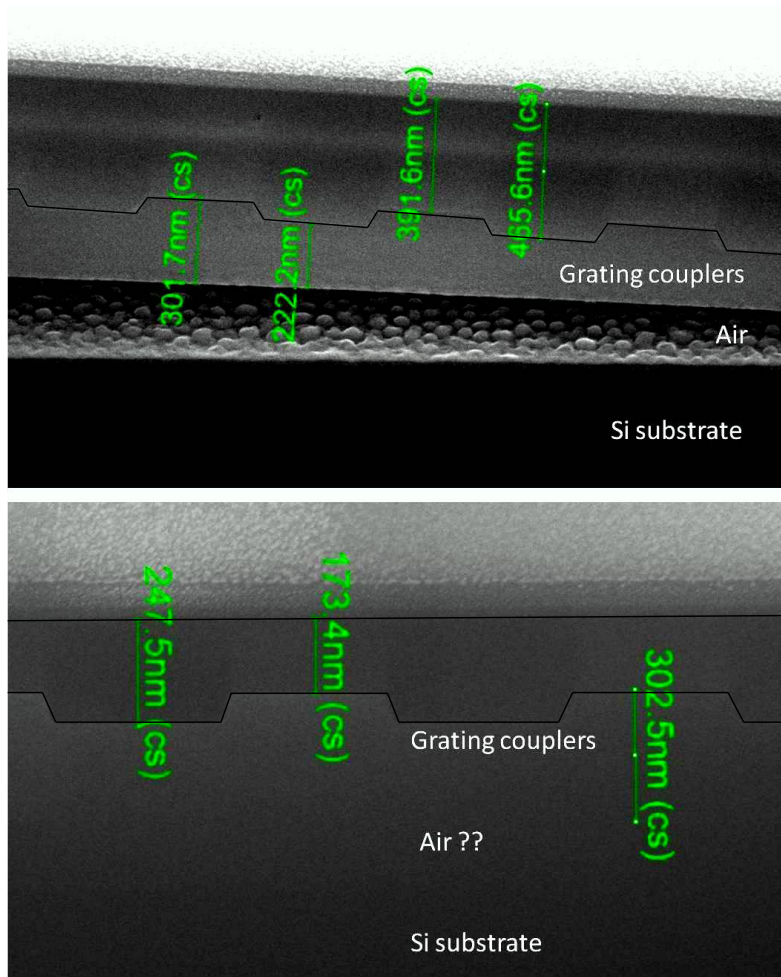


Figure 3.11: Top: Grating couplers membrane suspended in air on a silicon substrate. The membrane is tilted which makes the alignment at 10° between fiber and grating couplers very difficult. Bottom: The grating couplers membrane suspended in air has collapsed on the silicon substrate. No air can be observed anymore between the gratings and the silicon substrate.



Figure 3.12: Bad detachment of the photonic circuit membrane after collapse. Part of the photonic circuit is stuck to the fiber facet (left) while other part remains on the SOI chip (right).

were also investigated. For further details on this process and alternatives we refer to [52].

Only after exhausting the possibilities of this route, we decided to investigate other routes. Eventually we fabricated the fiber probe following one of these alternative routes which is described in the following subsection.

3.3.2 Route 2: successful

This second route consists of detaching the photonic circuit through the back side of the chip, instead of from the front (as tried in the first route). The idea is to remove every layer under the sensing device. An overview of the fabrication process is given in Figure 3.13.

First the sample is bonded upside down on a silicon carrier wafer by means of CrystalBond 509 wax from Electron Microscopy Science. This wax releases easily after processing and leaves only a little and easy-to-remove residue on the sensor surface.

In a next step the silicon substrate, which is $750\ \mu\text{m}$ thick, must be removed. This is not a straightforward task since many aspects must be taken into account. First, one must take care that the sample will be mechanically robust enough to be still manipulated after the process. Second, the optical circuit must remain intact to avoid any deterioration in the sensor performance.

Three different methods are used for this approach: First we use mechanical grinding to reduce the substrate to $100\ \mu\text{m}$. This is done by mounting the wafer on a chuck after which the substrate is pressed down against a rotating pad while a chemical slurry is flown over the pad. The silicon is removed by a

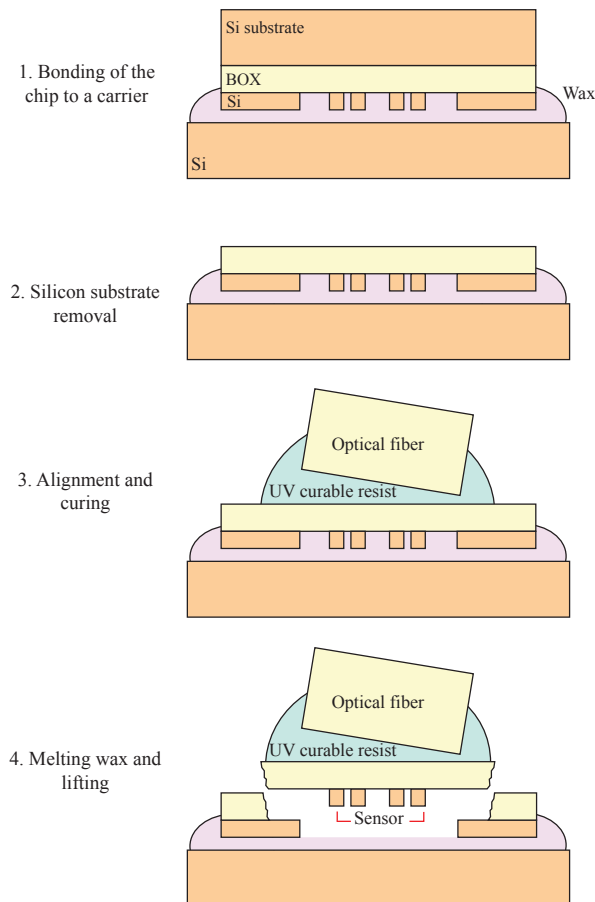


Figure 3.13: Fabrication process. All the illustrations represent the cross-section of the SOI chip and optical fiber. (1) Upside-down bonding of the SOI chip to a silicon carrier wafer by means of wax. (2) Removal of the silicon substrate by subsequent mechanical grinding, dry etching and wet etching. (3) Gluing of the photonic circuit to the tip of a fiber after active alignment of the fiber core to the grating coupler under an angle of 10° off the vertical axis to obtain optimal coupling. (4) The wax that bonds the sensor to the silicon carrier wafer is melted and by lifting the fiber, the thin layer of silicon dioxide around the sensor breaks under the weight of the remaining part of the photonic chip, leaving only the sensor circuit on the tip of the fiber.

combination of abrasive lapping and chemical etching.

The remaining 100 μm of silicon substrate are removed by dry and wet etching. Dry etching of silicon is mainly done using a combination of a fluorine-based gas (like SF_6 or CF_4) and other gases (like O_2 or N_2O). The principle of this etching method is based on generating a plasma of the precursor gasses that comes into contact with silicon. Fluorine ions are responsible for the main mechanism of etching silicon while the oxygen prevents recombination of fluorine ions with fluorosulphur radicals, thus increasing the net amount of fluorine ions and as a consequence, the etch rate [53]. With this method we reduce the thickness of silicon to 50 μm , leaving the rest to be removed by wet etching.

Wet etching of silicon can be done either isotropically (using a mixture of HF , HNO_3 , CH_3COOH and water) or anisotropically where the most commonly used etchants are KOH and tetramethylammoniumhydroxide (TMAH).

At first sight it seems logical to opt for KOH and TMAH, which are both anisotropic etchants and show a high selectivity of etching silicon compared to silicon dioxide [54]. The buried oxide layer of our chip thus acts as an etch stop layer, guaranteeing the integrity of our sensing device located under this layer. However, these etchants require a temperature of $70^\circ - 90^\circ\text{C}$ to achieve a typical etch rate of 0.1-1 $\mu\text{m}/\text{min}$. As a consequence, the wax used to bond the die to the carrier melts, releasing the 50 μm -thick membrane in the etching solution.

After discarding the previous option, we can only use isotropic etching. This has one main disadvantage: due to the fact that the mixture contains HF , once the substrate has been removed, the etch will not stop at the buried oxide layer. This implies that not only the silicon dioxide layer will be removed but the 220 nm thin top silicon layer will also be etched in an instant. Therefore very precise timing is required and an optimized solution rate had to be investigated.

The etching solution used is a mixture of acetic, nitric and hydrofluoric acid ($\text{CH}_3\text{COOH}:\text{NH}_3:\text{HF}$, 4:5:1) at 20°C . After precise removal of the rest of the silicon substrate, a thorough rinse of the dye with DI water is required.

At this point only the silicon circuit and the 2 μm -thick silicon dioxide layer are left on top of the wax bonded to the carrier wafer.

In an optical setup, the optical fiber core is actively aligned to the grating coupler through the silicon dioxide layer. This top cladding layer on the grating coupler will not significantly change the absolute value of the coupling efficiency but will cause a shift in the wavelength spectrum. From the grating period condition:

$$\Lambda = \frac{\lambda_0}{n_{eff} - n_{incident}\sin(\theta)} \quad (3.5)$$

where Λ is the period of the grating, λ_0 the wavelength of the incident light in vacuum, n_{eff} the effective index of the optical mode, θ the incident angle

with the normal to the grating surface and $n_{incident}$ the refractive index of the medium of incidence, we can expect that the wavelength spectrum will shift towards shorter wavelengths when increasing the refractive index of the top cladding layer (from 1.0 of air to 1.44 of silicon dioxide).

For the active alignment, the ultraviolet (UV) curable resist PAK-01 is applied on the fiber tip, which decreases the index contrast between the incident medium and the silicon dioxide, thereby optimizing the transmission.

After the alignment is performed, the fiber is glued to the chip by exposing the PAK-01 to UV light. Note that the chip and the fiber form an angle of 10° , corresponding to the angle of optimal efficiency and low reflection of the grating.

Subsequently, the wax that holds the sensor to the silicon carrier wafer is melted by heating the carrier wafer to 110°C with a hot plate. By lifting the fiber carefully, the thin layer of silicon dioxide around the sensor breaks under the weight of the remaining part of the photonic chip, leaving only the sensor circuit on the tip of the fiber.

To facilitate breaking the silicon dioxide layer around the circuit, we found it necessary to selectively thin down that layer from $2\ \mu\text{m}$ to $700\ \text{nm}$. This was achieved by dry etching over a circular area around the circuit (Figure 3.14), while the sensing circuit was protected by a thin SU-8 layer. This partial etching is performed prior to the bonding of the sample to the carrier wafer.

Finally, the residue of the wax on the sensing surface is removed by immersing the fiber in acetone for 5 minutes at 75°C .

3.4 Characterization of the fiber probe sensor

To measure the transmission of the sensor integrated on the fiber tip, light from a tunable laser source is coupled into our sensor fiber and this is coupled out and detected by a photodetector. The bi-directional transmission through the sensor fiber is achieved using a fiber-optic circulator as illustrated in Figure 3.15. The polarization is optimized for maximal coupling to the quasi-transverse electric (quasi-TE) mode of the SOI circuit using a fiber polarization controller.

When the sensing device is immersed in a sample solution, the change of the refractive index in that solution leads to a shift in the resonance wavelength that can be calculated using equation 2.26. This shift is monitored by repeatedly scanning the spectrum.

Figure 3.16 displays a measured resonance peak of the resonator integrated on the fiber tip. By fitting a Lorentzian function to this spectrum, the quality factor of this resonance was determined to be 2350, which is the same as before bonding. Note that this is lower than that of optimal SOI ring resonators in

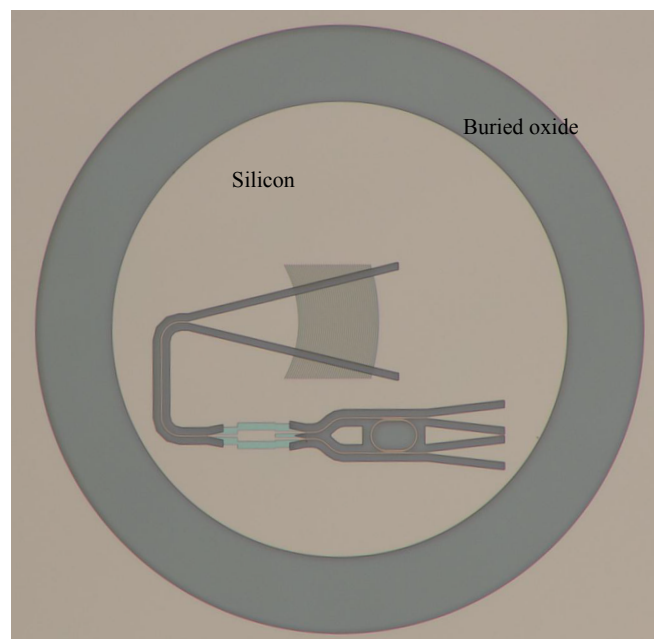


Figure 3.14: The optical circuit is surrounded by a ring structure which exposes the buried oxide layer. This is locally and partially etched to facilitate the breaking of this layer in the final step.

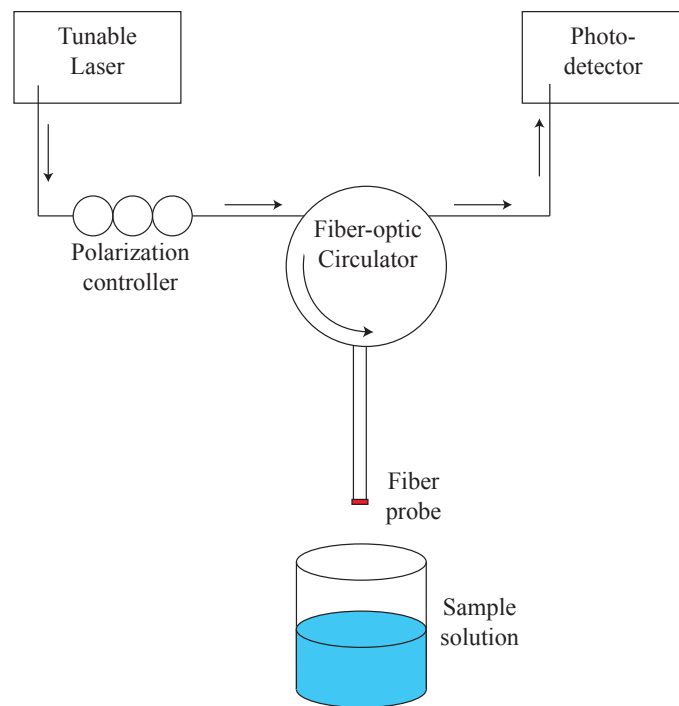


Figure 3.15: Read-out: The optical fiber probe is connected to a tunable laser source and a photodetector through a fiber-optic circulator. The polarization is optimized using a fiber polarization controller.

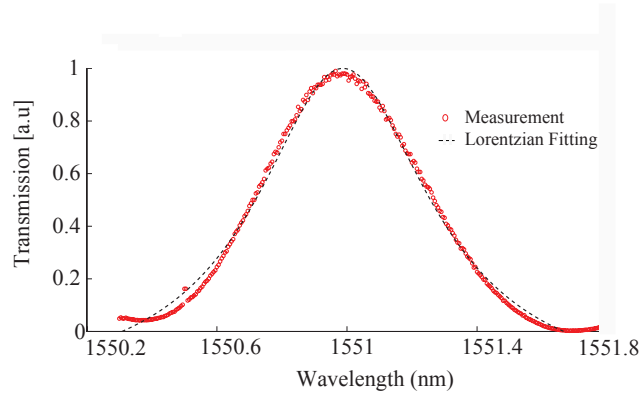


Figure 3.16: Fiber probe resonance. In red a measured resonance peak of the resonator integrated on the fiber tip. By fitting a Lorentzian function (dashed black line) the quality factor was determined to be 2350.

water, which could be over 10000. We can expect a significant improvement of the quality factor by optimizing the coupling sections of the resonator and by increasing its bend radius to reduce the bend loss. This can be done by making more efficient use of the available space on the fiber tip.

As a proof-of-principle experiment to show the capabilities of the fiber probe, we measured the sensitivity for refractive index changes of aqueous solutions and compared it to the one we had previously measured for a similar silicon-on-insulator ring resonator sensor that was not integrated on a fiber tip [55]. We used aqueous ethanol solutions with different concentrations, which refractive indices were derived from [56]. No surface chemistry was applied to the sensor surface.

Figure 3.17 illustrates the measured resonance wavelength shift of our sensor as a function of the refractive index change of the solution. The mean wavelength shift values over 3 measurements on the same device are shown with weighted variance error bars. As expected we observe a linear correlation between the wavelength shifts and the change of refractive index.

The sensitivity is determined to be 72 nm RIU^{-1} , which corresponds to the value we previously measured in [55]. This shows that the entire fabrication process has no detrimental effect on the performance of the device.

In order to compensate for temperature variations in a real environment, a second fiber probe sensor is required, which must be shielded from refractive index changes by a cladding, providing then a reference for the measurement.

After this work, a similar approach has been performed by Shambat in [57] where a semiconductor photonic crystal membrane is transferred to a fiber

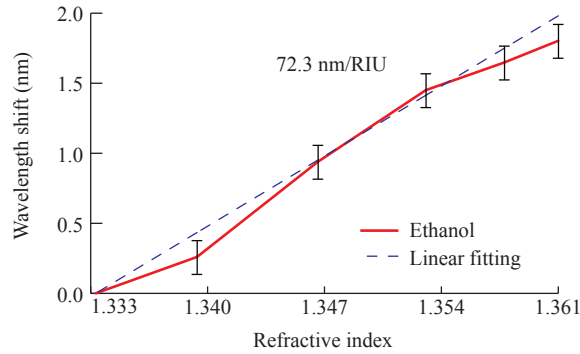


Figure 3.17: Measured resonance wavelength shift due to the change in refractive index of various aqueous solutions. The mean wavelength shifts over three measurements on the same device are shown with weighted variance error bars. The resonance wavelength shifts linearly with the refractive index of the solution with a sensitivity of 72.3 nm RIU^{-1} .

facet using a different fabrication process, and maintaining as well the performance of the sensor.

3.5 Conclusions

We have given an overview of the most common types of optical fiber sensors used for label-free biosensing. Apart from the literature study, we have also presented a novel implementation for a fiber probe that combines the good performance of silicon-on-insulator sensors with the high mobility of optical fibers. In this implementation an integrated SOI circuit is transferred to the facet of a single mode optical fiber. The fabrication of the device has been described in detail and its characterization using bulk sensing experiments has shown no degradation when comparing to the same sensor on SOI chip, i.e. not integrated on a fiber tip. Future work involves chemical modification of the sensor surface for specific sensing which can lead to a robust and portable device for in-vivo label-free biosensing applications such as an endoscopy.

References

- [1] K. T. V. Grattan and T. Sun. *Fiber optic sensor technology: an overview*. Sensors and Actuators A-Physical, 82(1):40–61, 2000.
- [2] O. S. Wolfbeis and X.-D. Wang. *Fiber-optic chemical sensors and biosensors*, volume 85. Analytical Chemistry, January 2000.
- [3] E. Squillante. *Applications of fiber-optic evanescent wave spectroscopy*. Drug Dev. Ind. Pharmac, 24:1163–1175, 1998.
- [4] K. R. Rogers and E. J. Poziomek. *Fiber optic sensors for environmental monitoring*. Chemosphere, 33:1151–1174, 1996.
- [5] W. L. Wise DL. *Biosensors with Fiberoptics*. Humana Press New Jersey, 1991.
- [6] M. E. Bosch, A. J. R. Sánchez, F. S. Rojas, and C. B. Ojeda. *Recent development in optical fiber biosensors*. Sensors, 7(6):797–859, June 2007.
- [7] X. Fan, I. M. White, S. I. Shopova, H. Zhu, J. D. Suter, Y. Sun, and J. D. Suter. *Sensitive optical biosensors for unlabeled targets: a review*. Analytica Chimica Acta, 620(1-2):8–26, July 2008.
- [8] A. Kersey, M. Davis, H. Patrick, M. LeBlanc, K. Koo, C. Askins, M. Putnam, and E. Friebele. *Fiber grating sensors*. Journal of Lightwave Technology, 15:1442, 1997.
- [9] A. Cusano, A. Cutola, and J. Albert, editors. *Fiber Bragg Grating sensors: research advancements, industrial applications and market exploitation*. Bentham Ebooks, 2011.
- [10] B. S. Kawasaki, K. O. Hill, D. C. Johnson, and Y. Fujii. *Narrow-band Bragg reflectors in optical fibers*. Optics Letters, 3(2):66–8, August 1978.
- [11] W. Sorin and H. Shaw. *A single-mode fiber evanescent grating reflector*. Journal of Lightwave Technology, 3:1041–1043, 1985.
- [12] M. Farries, C. Ragdale, and D. Reid. *Broadband chirped fibre Bragg filters for pump rejection and recycling in erbium doped fibre amplifiers*. IEEE Electronic Letters, 28(5):487 – 489, 1992.
- [13] K. Schroeder, W. Ecke, R. Mueller, R. Willsch, and A. Andreev. *A fibre Bragg grating refractometer*. Measurement Science and Technology, 12:757–764, 2001.
- [14] W. Liang, Y. Huang, Y. Xu, R. K. Lee, and A. Yariv. *Highly sensitive fiber Bragg grating refractive index sensors*. Applied Physics Letters, 86(15):151122, 2005.

- [15] A. N. Chryssis, S. B. M. Lee, S. S. Saini, and M. Dagenais. *High sensitivity evanescent field fiber bragg grating sensor*. IEEE Photonics Technology Letters, 17(6):1253–1255, 2005.
- [16] A. N. Chryssis, S. S. Saini, S. M. Lee, H. Yi, W. E. Bentley, and M. Dagenais. *Detecting hybridization of DNA by highly sensitive grating sensors*. IEEE Journal of Quantum Electronics, 11(4):864–872, 2005.
- [17] S. S. Saini, C. Stanford, S. M. Lee, J. Park, P. Deshong, W. E. Bentley, and M. Dagenais. *Monolayer detection of biochemical agents using etched-core fiber bragg grating sensors*. IEEE Photonics Technology Letters, 19(18):1341–1343, 2007.
- [18] M. C. Phan Huy, G. Laffont, V. Dewynter, P. Ferdinand, P. Roy, J.-L. Auguste, D. Pagnoux, W. Blanc, and B. Dussardier. *Three-hole microstructured optical fiber for efficient fiber Bragg grating refractometer*. Optics Letters, 32(16):2390–2, August 2007.
- [19] Y. Zhang, H. Shibru, K. L. Cooper, and A. Wang. *Miniature fiber-optic multicavity Fabry-Perot interferometric biosensor*. Optics Letters, 30(9):1021–3, May 2005.
- [20] X. Wang, K. L. Cooper, A. Wang, J. Xu, Z. Wang, Y. Zhang, and Z. Tu. *Label-free DNA sequence detection using oligonucleotide functionalized optical fiber*. Applied Physics Letters, 89(16):163901, 2006.
- [21] Y. Zhang, X. Chen, Y. Wang, K. L. Cooper, and A. Wang. *Microgap multi-cavity Fabry-Pérot biosensor*. Journal of Lightwave Technology, 25(7):1797–1804, 2007.
- [22] T. Wei, Y. Han, Y. Li, H.-L. Tsai, and H. Xiao. *Temperature-insensitive miniaturized fiber inline Fabry-Perot interferometer for highly sensitive refractive index measurement*. Optics Express, 16(8):5764–5769, April 2008.
- [23] K. Hill, B. Malo, K. Vineberg, F. Bilodeau, D. Johnson, and I. Skinner. *Efficient mode conversion in telecommunication fibre using externally written gratings*. IEEE Electronic Letters, 26(16):1270–1272, 1990.
- [24] X. Chen, K. Zhou, L. Zhang, and I. Bennion. *Dual-peak long-period fiber gratings with enhanced refractive index sensitivity by finely tailored mode dispersion that uses the light cladding etching technique*. Applied Optics, 46(4):451–452, 2007.
- [25] X. Shu, L. Zhang, and I. Bennion. *Sensitivity characteristics of Long-Period Fiber Gratings*. Journal of Lightwave Technology, 20(2):255, 2002.

- [26] N. Burani and J. Lægsgaard. *Perturbative modeling of Bragg-grating-based biosensors in photonic-crystal fibers*. Journal of the Optical Society of America B, 22(11):2487–2493, 2005.
- [27] B. H. Lee, Y. Liu, S. B. Lee, S. S. Choi, and J. N. Jang. *Displacements of the resonant peaks of a long-period fiber grating induced by a change of ambient refractive index*. Optics Letters, 22(23):1769–71, December 1997.
- [28] N. Chen, B. Yun, and Y. Cui. *Cladding mode resonances of etch-eroded fiber Bragg grating for ambient refractive index sensing*. Applied Physics Letters, 88(13):133902, 2006.
- [29] L. Rindorf and O. Bang. *Highly sensitive refractometer with a photonic-crystal-fiber long-period grating*. Optics Letters, 33(6):563–5, March 2008.
- [30] L. Rindorf, J. B. Jensen, M. Dufva, L. H. Pedersen, P. E. Høiby, and O. Bang. *Photonic crystal fiber long-period gratings for biochemical sensing*. Optics Express, 14(18):8224–8231, September 2006.
- [31] H. Tazawa, T. Kanie, and M. Katayama. *Fiber-optic coupler based refractive index sensor and its application to biosensing*. Applied Physics Letters, 91(11):113901, 2007.
- [32] R. Jorgenson and S. Yee. *A fiber-optic chemical sensor based on surface plasmon resonance*. Sensors and Actuators B: Chemical, 12(3):213–220, April 1993.
- [33] R. Slavík, J. Homola, J. Čtyroký, and E. Brynda. *Novel spectral fiber optic sensor based on surface plasmon resonance*. Sensors and Actuators B, 74:106–111, 2001.
- [34] H. Lin, W. Tsai, Y. Tsao, and B. Sheu. *Side-polished multimode fiber biosensor based on surface plasmon resonance with halogen light*. Applied Optics, 46(5):800–806, 2007.
- [35] M. Piliarik, J. Homola, Z. Maníková, and J. Čtyroký. *Surface plasmon resonance sensor based on a single-mode polarization-maintaining optical fiber*. Sensors and Actuators B: Chemical, 90(1-3):236–242, April 2003.
- [36] M. Chiu, S. Wang, and R. Chang. *D-type fiber biosensor based on surface-plasmon resonance technology and heterodyne interferometry*. Optics Letters, 30(3):233–235, 2005.
- [37] B. Spackova and J. Homola. *Theoretical analysis of a fiber optic surface plasmon resonance sensor utilizing a Bragg grating*. Optics Express, 17(25):199–203, 2009.

- [38] R. Jha, R. K. Verma, and B. D. Gupta. *Surface Plasmon Resonance-Based Tapered Fiber Optic Sensor: Sensitivity Enhancement by Introducing a Teflon Layer Between Core and Metal Layer*. *Plasmonics*, 3(4):151–156, September 2008.
- [39] D. G. Myszka. *Improving biosensor analysis*. *Journal of Molecular Recognition*, 12(5):279–84, 2000.
- [40] D. Ravi Shankaran and N. Miura. *Trends in interfacial design for surface plasmon resonance based immunoassays*. *Journal of Physics D: Applied Physics*, 40(23):7187–7200, December 2007.
- [41] J. Pollet, F. Delpoort, K. P. F. Janssen, K. Jans, G. Maes, H. Pfeiffer, M. Wevers, and J. Lammertyn. *Fiber optic SPR biosensing of DNA hybridization and DNA-protein interactions*. *Biosensors & Bioelectronics*, 25(4):864–9, December 2009.
- [42] J. Pollet, K. P. F. Janssen, K. Knez, and J. Lammertyn. *Real-time monitoring of solid-phase PCR using fiber-optic SPR*. *Small (Wiley-VCH)*, 7(8):1003–6, April 2011.
- [43] T. Tamir and S. Peng. *Analysis and design of grating couplers*. *Applied Physics*, 14(3):235–254, 1977.
- [44] D. Taillaert. *Grating couplers as interference between optical fibers and nanophotonic waveguides*. PhD thesis, Ghent University, 2005.
- [45] D. Taillaert, F. Van Laere, M. Ayre, W. Bogaerts, D. Van Thourhout, P. Bienstman, and R. Baets. *Grating couplers for coupling between optical fibers and nanophotonic waveguides*. *Japanese Journal of Applied Physics*, 45(8A):6071–6077, August 2006.
- [46] F. Van Laere, G. Roelkens, M. Ayre, J. Schrauwen, D. Taillaert, D. Van Thourhout, T. F. Krauss, and R. Baets. *Compact and highly efficient grating couplers between optical fiber and nanophotonic waveguides*. *Journal of Lightwave Technology*, 25(1):151–156, 2007.
- [47] F. Van Laere, T. Claes, J. Schrauwen, S. Scheerlinck, W. Bogaerts, D. Taillaert, L. O’Faolain, D. Van Thourhout, R. Baets, F. V. Laere, L. O’ Faolain, and D. V. Thourhout. *Compact focusing grating couplers for Silicon-on-Insulator integrated circuits*. *IEEE Photonics Technology Letters*, 19(23):1919–1921, 2007.
- [48] F. Van Laere, W. Bogaerts, P. Dumon, G. Roelkens, D. Van Thourhout, and R. Baets. *Focusing polarization diversity grating couplers in Silicon-on-Insulator*. *Journal of Lightwave Technology*, 27(5):612–618, 2009.

- [49] D. Vermeulen, K. V. Acoleyen, S. Ghosh, S. Selvaraja, W. A. D. D. Cort, N. A. Yebo, E. Hallynck, K. D. Vos, P. P. P. Debackere, P. Dumon, W. Bogaerts, G. Roelkens, D. V. Thourhout, and R. Baets. *Efficient tapering to the fundamental Quasi-TM mode in asymmetrical waveguides*. In ECIO, pages 1–2, 2010.
- [50] D. Taillaert, P. Bienstman, and R. Baets. *Compact efficient broadband grating coupler for silicon-on-insulator waveguides*. Optics Letters, 29(23):2749–51, December 2004.
- [51] M. Verbist, W. Bogaerts, J. Schrauwen, and R. Baets. *Silicon-on-Insulator-based retroreflective optical marker chips for simultaneous identification*. IEEE Journal of Selected Topics in Quantum Electronics, 15(5):1427–1431, 2009.
- [52] C. Lerma Arce. *Optical fiber probe sensors for portable and in-vivo detection of biomolecules*. Master thesis, Ghent University, 2009.
- [53] Y. Tzeng and T. H. Lin. *Dry etching of silicon materials in SF₆ based plasmas*. Journal of Electrochemical Society, 134(9):2304–2309, 1987.
- [54] H. Seidel, L. Csepregi, A. Heuberger, H. Baumgärtel, and H. Baumgartel. *Anisotropic Etching of Crystalline Silicon in Alkaline Solutions - Influence of Dopants*. Journal of Electrochemical Society, 137(11):3626–3622, 1990.
- [55] K. De Vos, I. Bartolozzi, E. Schacht, P. Bienstman, and R. Baets. *Silicon-on-Insulator microring resonator for sensitive and label-free biosensing*. Optics Express, 15(12):7610–7615, June 2007.
- [56] R. Belda, J. Herraiez, and O. Diez. *A study of the refractive index and surface tension synergy of the binary water/ethanol: influence of concentration*. Physics and Chemistry of Liquids, 43(1):91–101, 2005.
- [57] G. Shambat, J. Provine, K. Rivoire, T. Sarmiento, J. Harris, and J. Vuckovic. *Optical fiber tips functionalized with semiconductor photonic crystal cavities*. Applied Physics Letters, 99(19):191102, 2011.

4

Digital microfluidic platform for photonic biosensors

Analyte delivery is one of the key factors of any label-free biosensor platform. Typically a fluidic component is required to be placed on top of the sensor which allows for continuous delivery of the sample to the sensor surface. The most standard form is often a flow cell glued onto the sensor surface through which microchannels bring the analyte in contact with the sensor. However, this offers little flexibility in terms of scalability and reconfigurability and often implies an additional degree of integration and complexity to the system.

In this chapter we introduce the use of microdroplets, instead of continuous flows, in a digital microfluidic system to characterize a silicon ring resonator biosensor platform. The main advantage of this system is that it avoids possible leaks, channel clogging and cross-talk between samples or reagents and allows fluid plugs to be manipulated on reconfigurable paths, which cannot be achieved using the more established and more complex technology of microfluidic channels where samples can only be manipulated sequentially. It has great potential for high-throughput liquid handling, while avoiding on-chip cross contamination.

In the first section of this chapter, we will describe the principles of these digital microfluidics based on electrowetting. Later, we will introduce the basic toolkit for a digital microfluidic platform by studying the state-of-the art of this

technology. In section 4.2 we will present all the details on the digital microfluidic platform used for the integration of the photonic ring resonator biosensors described in section 4.3. The integration of both technologies as well as the proof-of-principle experiments and result analysis will be presented in the sections after that.

The work presented here was performed in close collaboration with the MeBioS research group (prof. Lammertyn, KU Leuven) which has a great deal of experience in digital microfluidics.

4.1 Digital microfluidics

An alternative to continuous flow devices is to manipulate the liquid as unit-sized discrete microdroplets. Due to the architectural similarities with digital microelectronic systems (i.e. either a drop is present or not), this approach is often referred to as "digital" microfluidics. Digital microfluidic systems have several advantages over continuous-flow systems, the most important being re-configurability and scalability of the architecture [1].

Electrowetting [1] and dielectrophoresis [2] are the two most commonly used techniques for microdroplet actuation, although other methods have been demonstrated, such as thermocapillary actuation [3] and surface acoustic wave actuation [4]. In this chapter we will only focus on electrowetting which is primarily a contact line phenomenon, and refers to electric field-induced interfacial tension changes between a liquid and a solid conductor. Before proceeding and for a better understanding of the electrowetting mechanism in the following sections, we will first spend some lines in this section introducing some basic concepts of the theory of surface effects in microfluidics.

4.1.1 Basic concepts

4.1.1.1 Surface tension

Surface tension is a force created by intermolecular cohesive forces between materials in two different aggregation states. Figure 4.1 shows the interface between a gas and a liquid. A molecule in the bulk of the liquid forms (non-permanent) chemical bonds with its neighbors. At the surface/interface, the molecules cannot form as many bonds since the density of a gas is very low. This lack of chemical bonds results in a higher energy for the surface molecules. It costs energy to create a surface, thus a liquid will try to minimize its energy by minimizing the surface area. The force that minimizes the area is called surface tension, expressed as a force per length unit [$\text{N/m} = \text{J/m}^2$]. A typical value for a water/air interface at 20°C is 72.9 mJ/m^2 . Mercury has a relatively high value of

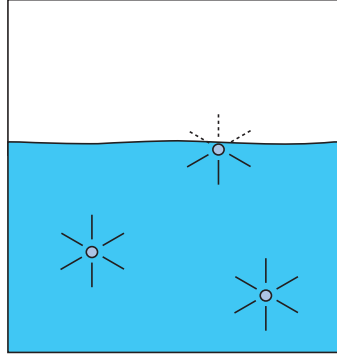


Figure 4.1: A molecule in the bulk of the liquid forms (non-permanent) chemical bonds with its neighbors. However, a molecule at the surface misses the chemical bonds in the direction of the surface (dashed lines). Consequently the energy of the surface molecules is higher than that of the bulk molecules and the formation of such an interface costs energy.

486.5 mJ/m² at the same temperature [5].

An important consequence of the surface tension is the so-called Young-Laplace pressure drop, defined as the pressure drop over a gas/liquid interface, and it is given by:

$$\Delta p_{surf} = \left(\frac{1}{R_1} + \frac{1}{R_2} \right) \gamma \quad (4.1)$$

Here, γ is the surface tension and R_1 and R_2 [m] are the curvature radii in the two orthogonal tangent directions at a point on the surface. We see that the curvature of the interface determines the force.

4.1.1.2 Contact angle

Another fundamental concept in the theory of surface effects is the contact angle that appears when a droplet is resting on a solid: a situation where we take into account three different phases, typically a solid, a liquid and a gas. The contact angle θ is defined as the angle between the solid/liquid interface and the liquid/gas interface at the contact line where the three immiscible phases meet and is given by the the following equation [5]:

$$\cos \theta = \frac{\gamma_{sg} - \gamma_{sl}}{\gamma_{lg}} \quad (4.2)$$

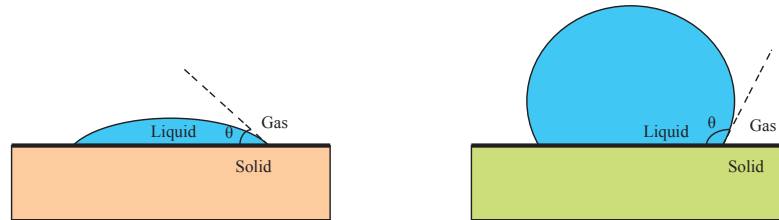


Figure 4.2: A contact angle is formed at the point where three phases (solid, liquid and gas) come together. The value of this angle θ depends on the different material parameters. The left droplet is placed on a hydrophilic surface ($\theta < 90^\circ$) and the right droplet on a hydrophobic surface ($\theta > 90^\circ$).

where γ_{sg} is the surface tension between gas and solid, γ_{lg} the surface tension between gas and liquid and γ_{sl} the interface tension (the tension between two non gaseous substances) between solid and liquid phases.

The shape of a small liquid droplet on a homogeneous substrate is usually a spherical cap. However, depending on the surface of the solid the contact angle will change, reflecting the type of interaction between liquid and solid. In Figure 4.2 we can see the difference between a hydrophilic (left) and hydrophobic (right) surface. A surface is called *hydrophilic* for a certain liquid when the contact angle θ is smaller than 90° ; it is called *hydrophobic* when the contact angle is greater than 90° . On surfaces where for certain liquids the contact angle is approximately 0° we say that *complete wetting* occurs.

Typically, water on a glass surface shows complete wetting, i.e. the contact angle is approximately 0° . However, when changing to a Teflon surface the contact angle increases considerably to 115° .

Another concept that we will mention later is the *hysteresis contact angle*, which is defined as the difference between the advancing (or maximal) and receding (or minimal) contact angles of a droplet as illustrated in Figure 4.3 for a droplet on tilted surface.

Now that the two fundamental concepts of surface effects in microfluidics have been explained, we can proceed to introduce the basic principles of electrowetting itself.

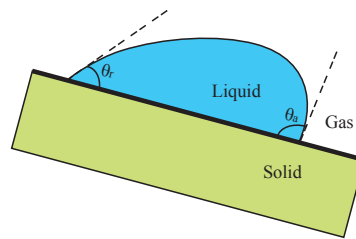


Figure 4.3: The difference between the advancing contact angle and receding contact angle of this droplet on a tilted surface is defined as the hysteresis contact angle.

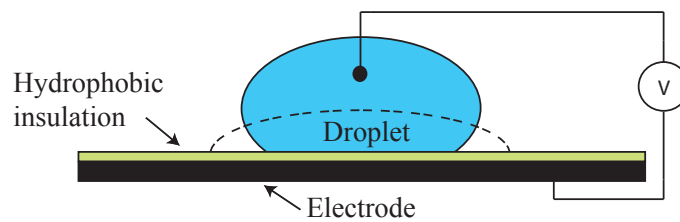


Figure 4.4: A droplet is initially at rest on a hydrophobic insulated electrode. Application of a voltage potential reduces the solid-liquid interfacial tension, resulting in improved wetting of the surface by the droplet.

4.1.2 Electrowetting principle

The basic electrowetting mechanism was discovered over a century ago by Lippmann [6] who observed that electrostatic charge can modify capillary forces. This concept was introduced to microfluidics by Congage et al. in [7].

The basic principle is illustrated in Figure 4.4 where a polarizable and conductive liquid droplet is initially at rest on a hydrophobic surface. When an electrical potential is applied between the droplet and an insulated counter-electrode underneath the droplet, improved wetting occurs through a reduction in the droplet's contact angle with the surface. The improved wetting is a consequence of the lowering of the effective solid-liquid interfacial energy through electrostatic energy stored in the capacitor, formed by the droplet-insulator-electrode system. The dependence of the effective solid-liquid interfacial tension, γ_{sl} , on the applied voltage, V , is given by Lippmann's equation [6]:

$$\gamma_{sl} = \gamma_{sl}^0 - \frac{1}{2}cV^2 \quad (4.3)$$

where V is the voltage difference, γ_{sl}^0 is the surface tension at zero voltage and c the capacitance per unit area. Considering γ_{lg} and γ_{sg} independent of the applied potential and consequently constant and neglecting gravity, we can use Young's equation of equilibrium at the 3 interfaces line (equation 4.2) to get

$$\cos\theta = \cos\theta_0 + \frac{cV^2}{2\gamma_{gl}} \quad (4.4)$$

where θ_0 is the zero-voltage contact angle. We note the strong dependence of the contact angle on the voltage which can lead to a switch between a hydrophobic and hydrophilic surface, and also its independence on whether the voltage is AC or DC.

We will call the above equation 4.4 the Young-Lippmann equation which, based on minimization of energy, is given by:

$$\cos\theta - \frac{\gamma_{sg} - \gamma_{sl}}{\gamma_{lg}} - \epsilon_s \frac{V^2}{2\gamma_{gl}h} = 0 \quad (4.5)$$

where ϵ_s is the dielectric constant of the solid and h its thickness.

There exist three forms of electrowetting.

Continuous Electrowetting (CEW) which uses metal droplets (e.g. mercury) in a filler liquid. CEW exploits changes in the surface tension of the liquid-metal-liquid (electrolyte) system at the liquid-solid-gas interface. Flow motion is induced due to the different surface tension at the two menisci caused by the electric potential [8].

Two other forms are Electrowetting (EW) and Electrowetting-On-Dielectric (EWOD), which are illustrated in Figure 4.5. They exploit changes in the solid-liquid surface tension, which in turn changes the contact angle. In EW an electrical double layer (EDL) is formed in between the electrode and the electrolyte droplet which typically is between 1 and 10 nm thick. Applying a voltage difference (around 1V) can cause an initially hydrophobic layer to act as a hydrophilic one. In essence the electric energy counterbalances the free surface energy and lowers the surface tension γ_{sl} . In EWOD there is no electric double layer but the balance of energy takes place in a hydrophobic dielectric layer between the electrode and the droplet, typically a Teflon layer of about $1\mu\text{m}$. The voltage required in this kind of system is much higher than that in EW, due to the relatively thick Teflon dielectric layer. For a layer thickness of $1\mu\text{m}$ about 100 Volts are required. However, an advantage of EWOD is that it can use any kind of aqueous (polar) liquids including most of water-based biofluids and chemical

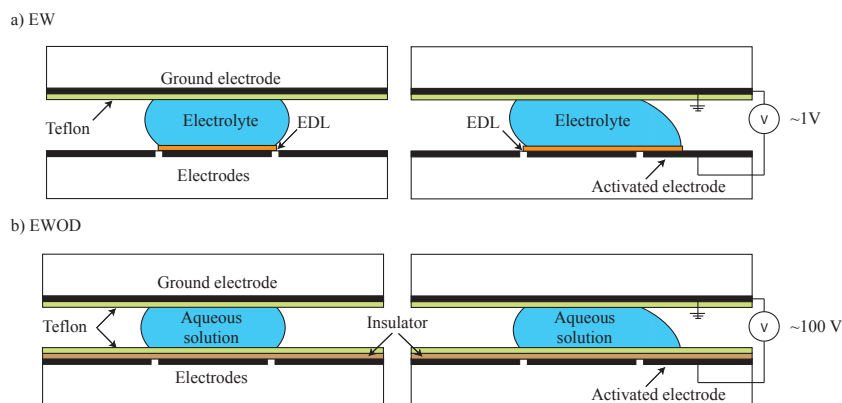


Figure 4.5: a) Electrowetting (EW): An electrical double layer (EDL) is formed between the electrodes and the droplet, which is an electrolyte. As a potential is applied, surface energy is balanced as electrical energy and the solid-liquid surface tension is lowered accordingly. b) Electrowetting-on-dielectric (EWOD): The balance of energy here takes place in a hydrophobic dielectric layer between the electrode and the droplet. Reproduced from [8].

solutions, while EW can only manipulate electrolytes. From now on we will focus on EWOD, since we will use this kind of digital microfluidics to characterize our silicon photonic biosensors.

4.1.3 Electrowetting-on-dielectric

A cross-section of a typical EWOD platform is shown in Figure 4.6.

The application of a voltage to a series of adjacent electrodes that can be turned on or off creates an interfacial tension gradient that can be used to manipulate droplets. Droplets are usually sandwiched between two parallel plates: the bottom being the chip surface, which contains the addressable electrode array, and the top surface being a continuous ground plate. When an interfacial tension gradient is created by applying a voltage across a droplet partially overlapping an electrode, the droplet will move to the most stable position, which is generally centered on the activated electrode. Droplets can be dispensed from reservoirs using electrodes adjacent to the reservoir and can be produced with a small variance in volume. This actuation can also be used to split large droplets as well as merge and rapidly mix droplets. For a theoretical study on how these operations are performed we refer to [9].

Generally, a typical EWOD device consists of a conductive material serving

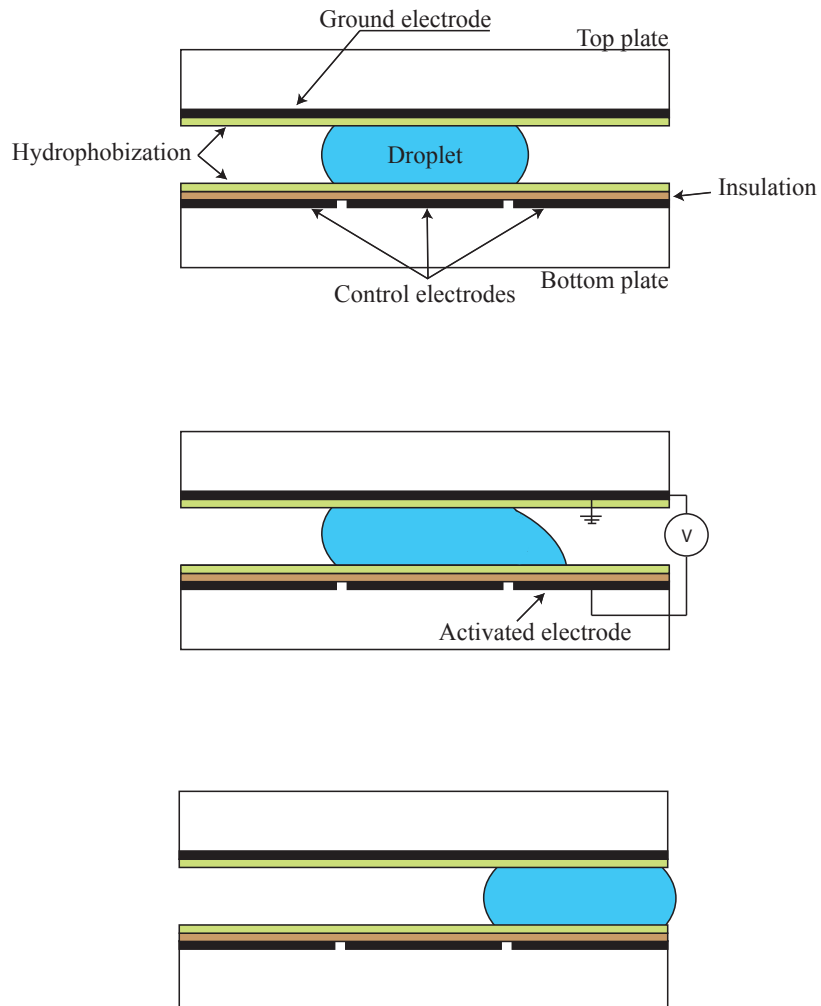


Figure 4.6: The application of a voltage to a series of adjacent electrodes can be turned on or off, creating an interfacial tension gradient which attracts the droplet towards the activated region.

as the electrodes and a dielectric material providing both the capacitance between liquid and electrode, and hydrophobicity of its surface at the solid-liquid interface (some dielectrics require an additional coating of a thin hydrophobic material due to inadequate hydrophobicity of their natural surface). However, these components with different intrinsic material properties influence the performance of an EWOD device in different ways. Hence there are two essential criteria for EWOD design when referring again to the Young-Lippmann equation 4.5 for EWOD:

$$\cos\theta = \cos\theta_0 + \frac{\epsilon_r\epsilon_0 V^2}{2\gamma_{gl}h} \quad (4.6)$$

where θ is the contact angle under an applied voltage V , θ_0 is the contact angle without externally applied potentials, ϵ_r is the dielectric constant of a dielectric layer of thickness h and ϵ_0 is the permittivity of vacuum. First, the inherent contact angle (without externally applied voltage) should be large enough to obtain a maximum contact angle variation; second, the thickness of the dielectric layer should be as small as possible to reduce the required voltages. To obtain a large contact angle (normally larger than 90°) at zero potential, one can either use highly hydrophobic insulators or hydrophilic insulators on which one deposits a very thin hydrophobic layer without blocking the electrical connection. However, minimizing the dielectric thickness may give rise to poor dielectric strength, and may cause dielectric breakdown at a much lower applied voltage. Besides these considerations, the applied potential should be minimized when operating the devices/systems but at the same time it must be big enough to activate the electrowetting mechanism which is defined by the threshold voltage, V_T [9]:

$$V_T = \sqrt{\frac{2h\gamma_{gl}}{\epsilon_r\epsilon_0 2}} [\tan\alpha(\sin\theta + \sin\theta_0)] \quad (4.7)$$

where α is the hysteresis contact angle. We observe that the threshold voltage is determined by the dielectric-thickness-to-dielectric-constant ratio, $\sqrt{h/\epsilon}$. Thus, to reduce the actuation threshold voltage, it is required to reduce $\sqrt{h/\epsilon}$.

Other considerations, such as mechanical, thermal and charge stability are important for reproducibility and biocompatibility. Minimal biomolecular adsorption of materials must be taken into consideration when handling bio- and physiological fluids.

The electrowetting phenomenon has been observed for mixtures of salt solutions (NaCl or Na₂SO₄) with other chemicals such as glycerol [10], ethanol [11] and methanol [12], without any degradation of EWOD performance. On the other hand, the transport of fluids containing proteins, such as enzyme-laden

reagents and human physiological fluids is not as straightforward. This is because most proteins tend to adsorb irreversibly to hydrophobic surfaces, and contaminate them. In addition to contamination, protein adsorption can also render the surface permanently hydrophilic. This is detrimental to transport, since electrowetting works on the principle of modifying the wettability of a hydrophobic surface. Since more and more research interests on EWOD have been driven by its biomedical applications, researchers have been investigating the applicability of EWOD devices in the presence of biomolecules and physiological fluids. Yoon et al. [13] showed that EWOD occurred with biofluids containing proteins, DNA and adult bovine whole serum of a biomolecule concentration of $4 \mu\text{g/ml}$, although the performance was degraded by the adsorption of biomolecules into the insulation layer giving rise to the reduced contact angle change and hysteresis. The compatibility of EWOD with physiological fluids such as insulin, cytochrome, myoglobin etc. has been demonstrated by Wheeler et al. [14] using an EWOD-based chip. The most recent popular applications of EWOD are bio-assays such as DNA extraction and amplification [15], cell-based assays [16, 17], enzymatic assays [18–21] and immunoassays [22]. EWOD actuation of human physiological fluids containing human whole blood, serum, plasma, urine, saliva sweat and tears was demonstrated at 20 Hz and less than 65 V by Srinivasan et al. [18] using an integrated digital microfluidic chip. All these experimental results show that an EWOD is indeed applicable to bio-assays.

4.2 Electrowetting-on dielectric platform for photonic biosensors

In the rest of the chapter we will demonstrate how digital microfluidics can be used for effective fluid delivery to photonic microring resonator sensors fully constructed in SOI. Combination of both technologies offers unique advantages and shows great potential for performing label-free biosensing, as cross-contamination, microchannel clogging and air bubble formation are avoided, while minimal sample waste is generated. Moreover, since digital microfluidics is inherently an array-based technique and photonic ring resonator sensors are commonly used in arrays as well, the proposed combined system is ideal for array-based biochemical applications. We will start this section by describing in detail the digital microfluidic system used for this approach.

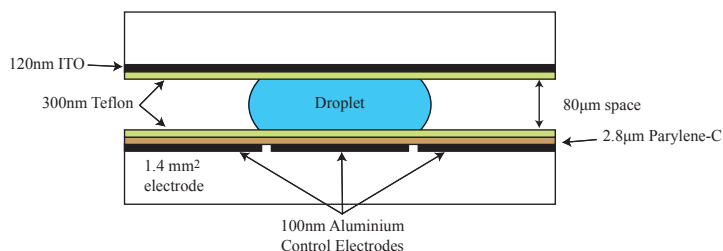


Figure 4.7: The cross-section of an electrowetting-on-dielectric (EWOD) lab-on-a-chip and the electrowetting principle. When a voltage is applied to an actuation electrode, the droplet is attracted toward this activated region owing to the imbalance generated in the interfacial tension near the surface above the actuated electrode [20].

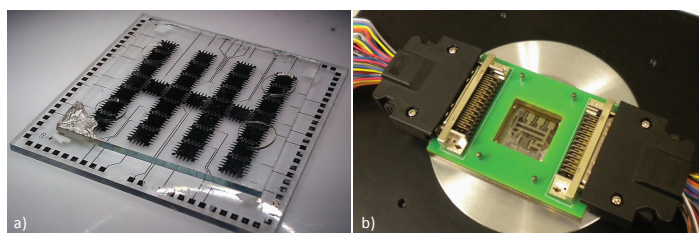


Figure 4.8: a) Photograph of the digital microfluidic chip with a standard ITO top plate, visualizing the sandwiched droplets. b) Assembled EWOD platform demonstrating the chip holder with electrical connections.

4.2.1 Digital microfluidic system

The cross-section of the EWOD lab-on-a-chip is shown in Figure 4.7. Many EWOD lab-on-a-chip device configurations exist, mainly differing in the actuation electrode architecture and the type of dielectric material used. This dielectric layer is a crucial element in the EWOD lab-on-a-chip configuration, as it isolates the liquid droplet from the actuation electrodes, thereby preventing electrolysis when a voltage is applied across the droplet [23, 24]. Below, we describe the fabrication process for the EWOD lab-on-a-chip from KU Leuven based on the protocol of [1].

The digital microfluidic platform is produced by means of standard photolithographic techniques. For the bottom part of the chip, a 100-nm thick aluminum layer is sputtered on a glass wafer and subsequently patterned. All electrodes are $1.4 \times 1.4 \text{ mm}^2$. The aluminum layer is covered by a $2.8 \text{ }\mu\text{m}$ dielec-

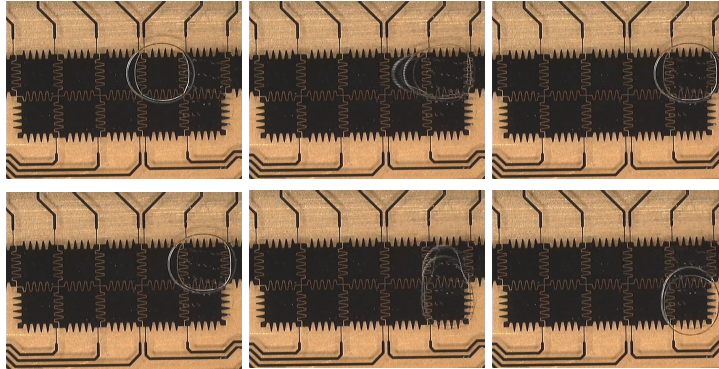


Figure 4.9: When a voltage is applied to the system, a surface tension gradient at the droplet surface is evoked which attracts the droplet towards the activated region. Thus, the droplet movement can be freely controlled along a pattern of electrodes.

tric Parylene-C layer deposited using chemical vapor deposition. This insulating layer is rendered hydrophobic by spin-coating a layer of Teflon-AF (300 nm thickness) on top. The top part of the digital lab-on-a-chip consists of a glass plate coated with a 120-nm thin layer of transparent indium tin oxide (ITO) which is also made hydrophobic with a Teflon-AF layer of approximately 300 nm. Standard tape with a thickness of 80 μm (3M) is used as a spacer between the top and bottom plates. Figure 4.8 shows this digital microfluidic platform. Droplets are sandwiched between the two plates. To activate the electrowetting-on-dielectric mechanism, a 130 V DC actuation voltage is used, while the electrode actuation sequence, activation time and relaxation time are controlled by means of homemade programs in MATLAB (The MathWorks) [25] and LabView (National Instruments Corp.) [26]. When a voltage is applied to the system, a surface tension gradient at the droplet surface is evoked which attracts the droplet towards the activated region. As such, the droplet movement can be freely controlled along a pattern of electrodes, as illustrated in Figure 4.9.

4.3 Photonic biosensors

The photonic biosensors used for this approach are the earlier described ring resonators. The photonic chip was fabricated in silicon-on-insulator with 2 μm buried oxide and a 220-nm silicon top layer using CMOS-compatible 193-nm optical lithography and dry etching [27]. The resonators consist of 450-nm-wide single-mode waveguides, with 5 μm bend radius, 2 μm long directional couplers and a gap of 180 nm between the waveguides. The layout of the chip is

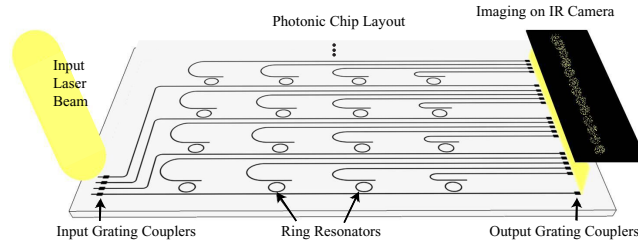


Figure 4.10: Chip layout top view. A SANTEC TSL-510 tunable laser was used as a light source. The input waveguides are simultaneously addressed through vertical grating couplers with a 2 mm-wide collimated beam from a tunable laser source. The output signals of the ring resonators are near-vertically coupled to free space by means of integrated grating couplers and are imaged with an infrared camera.

illustrated in Figure 4.10. Four rings are connected to one common input waveguide, each of them having a dedicated drop signal port. Five of these four ring series are placed independently next to the other. The five input waveguides are simultaneously addressed through vertical grating couplers [28] with a 2 mm-wide collimated beam from a tunable laser source. The output signals of the ring resonators are near-vertically coupled to free space by means of integrated grating couplers and are imaged with an infrared camera.

We use the shallow-etched gratings described in Chapter 3 which have a maximum coupling efficiency of 31% at 1.55 μm wavelength (40-nm 1-dB bandwidth) for 10° off-vertical coupling angle. Because the bandwidth of the grating couplers is larger than the free spectral range of the resonators, the grating couplers do not limit the number of resonators placed in series. This optical setup allows for very high alignment tolerances, measures the spectrum of all the ring resonators in parallel and therefore forms no limitation for high-throughput sensing. A SANTEC TSL-510 tunable laser is used as a light source. The transmitted light is detected by a XenICs infrared camera. The input power is chosen so that the intensity of the resonance peaks corresponds to the pixel saturation level to obtain a maximum signal-to-noise ratio. We have developed a Python-based software that captures the image from the infrared camera for every wavelength step of the laser sweep, and stores the maximum intensity values within each dedicated area that overlaps with an output grating coupler spot. This software has been developed and optimized by Sam Werquin, PhD student in our group. Post-processing consists of fitting the spectra to a Lorentzian function and tracking the peaks over time using MATLAB [25].

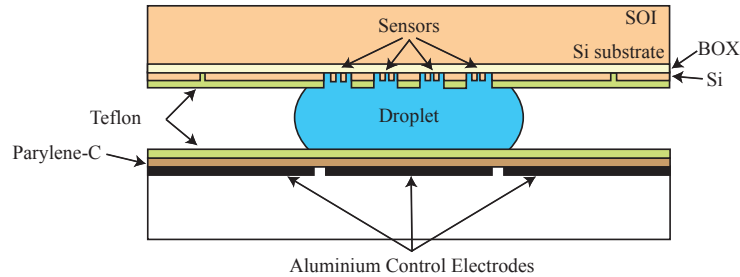


Figure 4.11: Incorporation of the silicon-on-insulator (SOI) chip containing an array of microring resonator sensors into the digital microfluidic system by replacing the top glass plate of the platform.

4.4 Integration of both technologies: digital microfluidic platform and photonic biosensors

The SOI chip containing the array of ring resonator sensors described above is incorporated into the digital microfluidic system by replacing the top glass plate of the platform. Figure 4.11 illustrates how the chip is placed up-side down, squeezing the liquid droplets against the bottom plate containing the buried electrodes. In order to guarantee the hydrophobicity of the SOI chip surface, which is crucial for performing droplet manipulations efficiently, and at the same time ensure the contact of the sensors with the droplets, a layer of Teflon-AF (300 nm thickness) needs to be coated on the SOI chip and subsequently patterned. For that reason, the Teflon-AF surface is activated with O_2 -plasma to allow photoresist to be spincoated on top. This thin layer of photoresist is then patterned by using standard photolithography to uncover the ring resonators. Next, the Teflon-AF covering the ring resonators is locally removed with reactive ion etching using O_2 -plasma. Some ring resonators are left covered with Teflon-AF in order to provide a reference to compensate for environmental drift.

Figure 4.12b shows how the SOI chip containing arrays of microring resonator sensors (Figure 4.12a) is aligned on top of the digital microfluidic chip so that the sensor array coincides with the electrode pattern underneath in the bottom plate of the microfluidic chip, thereby ensuring contact of the ring resonators with the liquid droplets.

As described in Section 4.3, grating couplers are used to couple the light from a tunable laser into the chip and couple it out to be detected by an infrared

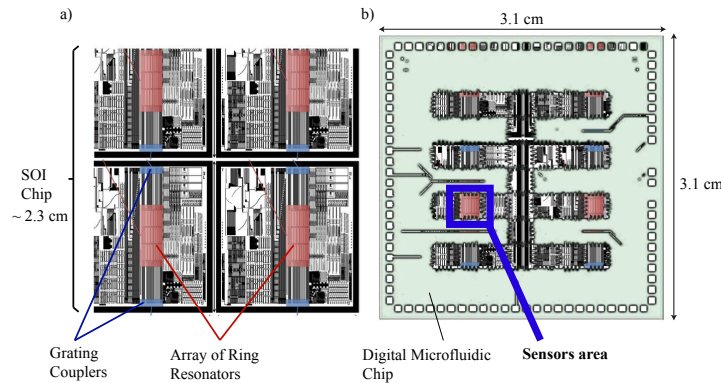


Figure 4.12: a) SOI chip containing arrays of microring resonator sensors. The relevant microring sensor arrays and grating couplers are indicated in red and blue, respectively. b) Alignment of the SOI chip on the digital microfluidic chip. The SOI chip was aligned so that one of sensor arrays coincided with the electrode pattern underneath, thereby ensuring contact of the ring resonators with the liquid droplets.

camera. A new aspect with respect to our previous work [29] is that now, since the chip is placed up-side down, light needs to be coupled in and out through the 750- μm thick silicon substrate. Silicon is considered practically transparent for the wavelength used (1.55 μm). However, to reduce the scattering of the rough substrate surface and to facilitate the alignment of the laser beam and the detection of the light coupled out from the chip, a few simple processing steps are done in advance: the silicon substrate is thinned down to 300 μm by chemical mechanical lapping and afterwards a chemical mechanical polishing step is performed in order to attain a smooth surface. The material removal occurs as a consequence of a combination of chemical reaction of the slurry chemicals with the silicon wafer surface and the repeated mechanical interaction between a pad or plate and the silicon substrate. Figure 4.13 shows an image from the IR camera where the chip is placed up-side down on a chuck that uses vacuum to keep the sensor fixed in place. The different photonic circuits of the SOI chip, the laser beam and even the vacuum holes of the chuck at the other side of the chip are clearly visible.

4.5 Experiments

As a proof-of-principle to show the capabilities of the combined system, we measured the sensitivity for refractive index changes of aqueous solutions and

	Volume (μm)	Sodium chloride		Glucose		Ethanol	
		Mass concentration (%)	Refractive index	Mass concentration (%)	Refractive index	Mass concentration (%)	Refractive index
Droplet 1	5	0	1.3105	0	1.3119	0	1.333
Droplet 2	5	1.01	1.3122	0.097	1.4559	10	1.3395
Droplet 3	5	1.84	1.3137	1.97	1.6044	20	1.3469

Table 4.1: Different concentrations and refractive indices of the droplets used in the experiments. For each chemical compound (sodium chloride, glucose, ethanol) three droplets of 5 μl with different concentrations were prepared. The refractive indices of sodium chloride and glucose were derived from [30] and the refractive index of ethanol was derived from [31].

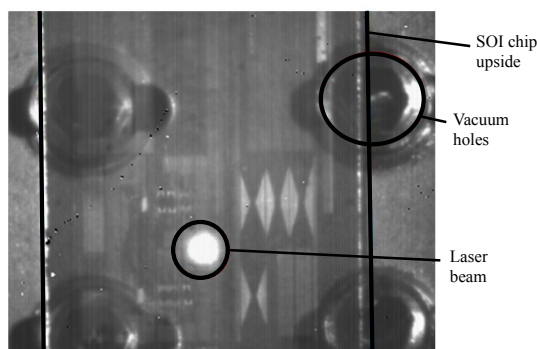


Figure 4.13: IR camera image. The chip is placed up-side down on a vacuum chuck. The laser beam and the vacuum holes of the chuck at the other side of the chip are clearly visible. The different photonic circuits on the SOI chip are distinguished as dark and lighted areas.

compared it with previous measurements for the same array of sensors using typical microfluidics based on microchannels [32] and simulations for bulk refractive index changes done in Fimmwave (Photon Design).

To demonstrate the proof-of-principle of on-chip sensing, three different sets of experiments were performed, each with a different chemical compound whose concentration in deionized (DI) water was to be determined. For this purpose, we chose sodium chloride, glucose and ethanol. For each of these compounds, 3 different droplets with different concentrations were prepared (Table 4.1). For this proof-of-principle experiment, droplets were pipetted manually on the chip surface. However, dilutions of these compounds can also be automated on-chip by executing multiple merging and splitting steps [19]. For each droplet, we performed simultaneous measurements with 12 different ring resonators in the array under the droplet. Finally, each of these measurements was repeated 3 times. In total, this represents $3 \times 3 \times 12 \times 3 = 324$ measurements, from which the sensor sensitivity and sensor variability can be derived. In each array, four ring resonators were left covered with Teflon-AE, to isolate them from external interaction and to provide a reference for each measurement. The refractive index of sodium chloride and glucose was derived from [30] and the refractive index of ethanol from [31].

The measurements were performed as follows, e.g. for the sodium chloride solutions: a droplet of DI-water was transported on the digital microfluidic platform to the sensors area. Our system started measuring. Subsequently, the droplet of water was moved, leaving a free route for the second droplet with a first sodium chloride concentration. Since the read-out system performs

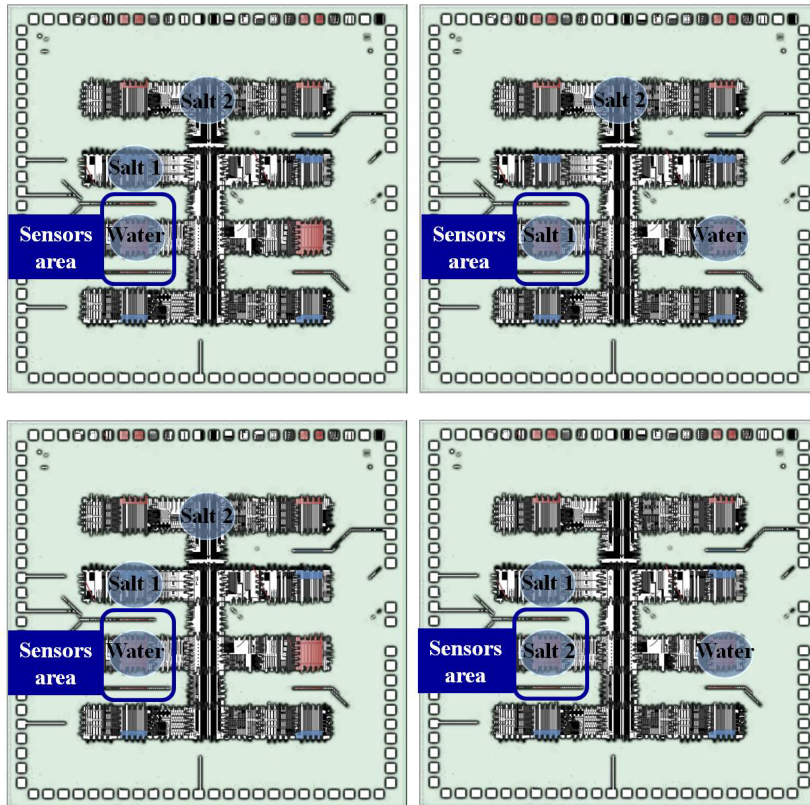


Figure 4.14: Measurement process. Our system started measuring when a droplet of deionized water was transported in the digital microfluidic platform to the sensor area. Subsequently, that droplet was switched for a droplet with a certain sodium chloride concentration which was measured once it reached the sensing area. This process was repeated by measuring again the water droplet and a third droplet with a different sodium chloride concentration.

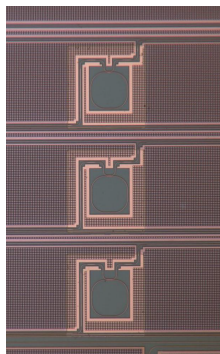


Figure 4.15: The SOI chip surface was coated with a 125 nm layer of Teflon AF and consequently patterned in order to guarantee the hydrophobicity of the SOI chip surface and at the same time ensure contact of the sensors with the droplets.

continuous measurements in time, we measured in air during the switching of droplets, causing a big shift in the resonance wavelength, which was discarded. When the second droplet reached the sensing area, the measured signal shifted again to a similar wavelength as measured during the previous droplet, since the refractive index of different watery solutions does not differ to a large extent. This process was repeated by measuring again the water droplet and a third droplet with a different sodium chloride concentration, as illustrated in Figure 4.14.

This same process was repeated for measuring glucose and ethanol concentrations in DI-water in order to confirm the behavior of the system for different refractive index materials and samples, while guaranteeing reproducibility. One photonic chip was used to perform the three repetitions of the measurement of each solution. Thus, three different photonic chips (one per each solution) were used in total to perform the experiments, while the digital microfluidic platform was reused.

4.6 Results

The Teflon-AF pattern on the array of ring resonator sensors is shown in Figure 4.15. It is a crucial aspect for the experiments performed, since it guarantees the hydrophobicity of the SOI chip surface and at the same time ensures the contact of the sensors with the droplets. In each array of sensors, four ring resonators were left covered with Teflon-AF to isolate them from external drifts. The measured signal of these rings shows a standard deviation smaller than 2%, providing thus an excellent reference for each measurement. Another impor-

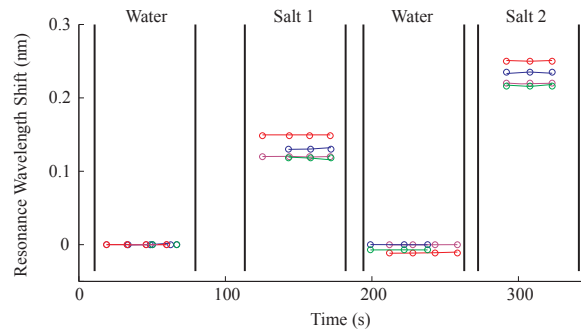


Figure 4.16: Evolution in time of the resonance wavelength shift of the ring resonators during the measurements of different sodium chloride concentrations. Each color corresponds to one sensor. When we change from water to salt solution and vice versa, the shift of the resonance wavelength is easily measurable.

tant aspect on these measurements is that the SOI is placed up-side down, so light needs to be coupled in and out through the silicon substrate.

Figure 4.16 shows the evolution in time of the resonance wavelength shift of the ring resonators during the measurements with different sodium chloride concentrations. Each color corresponds to one sensor. The shift of the resonance wavelength is easily measurable when changing from water to salt solution and vice versa. The variability between sensors was determined to be smaller than 8%. During the switch of droplets the measurement had to be done in air (as explained in previous section) which explains the absence of data points in the graph since the change of refractive index from aqueous solutions to air implies a big shift in the resonance wavelength.

Analyzing these shifts as a function of the refractive index unit (RIU) of the droplets, we observed a very close correspondence between the simulations and the measurement results (Figure 4.17). 78 nm/RIU is the sensitivity that these ring resonators show for refractive index change simulations, which was also measured and proved in [32] using the typical microfluidics system based on microchannels. The measurements performed in this digital microfluidics system show a sensitivity of 77 ± 0.6 nm/RIU, which shows that the performance of the transducer does not suffer from being integrated in a digital microfluidics system.

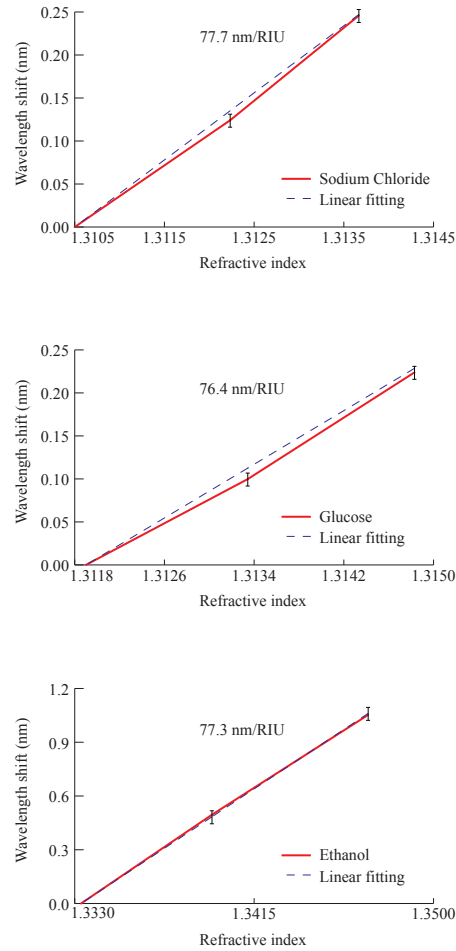


Figure 4.17: Three experiments with different sodium chloride, glucose, and ethanol concentrations were performed. Each line corresponds to one of these experiments. Error bars indicate the standard deviations based on three repetitions. Three photonic chips (one per solution) were used to perform the three experiments. A sensitivity of 77 ± 0.6 nm per refractive index unit (RIU) is determined taking into account the slope of the linear fitting for the three lines, showing a perfect match with simulations and previous measurements of the same sensors using the typical more complex microfluidic system [32].

4.7 Conclusions

In this chapter we have studied the basics of digital microfluidics, an emerging technology able to perform all the fluidic lab-on-a-chip operations (dispensing, transport, mixing, splitting, merging, storing) in a single platform without contamination.

We have presented the combination of this promising technology with the well-known label-free silicon photonic microring resonator sensors fabricated in SOI, providing an alternative to the typically costly and complex microfluidic system based on microchannels used for liquid sample delivery to microring resonators. This alternative provides a cheap and flexible method for the integration of photonic sensors and microfluidics, which enables plug-and-play ease of use, as no physical connection is needed between the optical chips and the light source and detection unit, while SOI chips can be fabricated in mass production volumes. This enhances disposability of the chips which is beneficial for performing bio-assays where cross contamination is of great concern.

We have proved the excellent performance and compatibility of this combined system, showing no degradation of the sensor performance with respect to simulations or previous measurements of the same sensors using the typical, more complex microfluidic system [32]. This combination allows for multiplexed real-time detection and analysis. Its great flexibility, portability and disposability make it ideal for easy and fast use in any laboratory.

Future work would consist of biofunctionalization of the microring sensor surface by using silane chemistry, which we were unable to perform ourselves due to time constraints. These experiments would allow us to functionalize the sensor surface with specific capture molecules without affecting the surface hydrophobicity and hence the sensor performance. This will open up many possibilities for performing multiplexed antibody detection and bio-assays on the proposed system, and further exploit its potential for performing miniaturized analysis. This can pave the way for a novel integrated platform for diagnostics and life sciences in general, as the platform can be exploited for assessing molecular interactions and cell-based studies in a multiplexed high-throughput context.

References

- [1] M. Pollack, A. Shenderov, and R. Fair. *Electrowetting-based actuation of droplets for integrated microfluidics*. *Lab on a Chip*, 2(2):96–101, 2002.
- [2] J. A. Schwartz, J. V. Vykoukal, and P. R. C. Gascoyne. *Droplet-based chemistry on a programmable micro-chip*. *Lab on a Chip*, 4(1):11–17, 2004.
- [3] A. A. Darhuber, J. P. Valentino, S. Member, S. M. Troian, and S. Wagner. *Thermocapillary actuation of droplets on chemically patterned surfaces by programmable microheater arrays*. *Journal of Microelectromechanical Systems*, 12(6):873–879, 2003.
- [4] A. Renaudin, P. Tabourier, V. Zhang, C. Druon, and J.-c. Camart. *Microgouttes plateforme saw dédiée à la microfluidique discrète pour applications biologiques Handling of SAW actuated droplets for biological applications Microgouttes*. *La Houille Blanche*, 3(1):1–5, 2006.
- [5] H. Bruus. *Theoretical Microfluidics*. Oxford University Press, 2008.
- [6] M. G. Lippmann. *Relations entre les phenomenes electriques et capillaires*. *Ann. Chim. Phys.*, 5(11):494–549, 1875.
- [7] E. Colgate and H. Matsumoto. *An investigation of electrowetting-based microactuation*. *Journal of Vacuum Science & Technology A: Vacuum, Surfaces and Films*, 8(4):3625 – 3633, 1990.
- [8] J. Lee, H. Moon, J. Fowler, T. Schoellhammer, and C.-J. Kim. *Electrowetting and electrowetting-on-dielectric for microscale liquid handling*. *Sensors and Actuators A: Physical*, 95(2-3):259–268, January 2002.
- [9] J. H. Song, R. Evans, Y.-Y. Lin, B.-N. Hsu, and R. B. Fair. *A scaling model for electrowetting-on-dielectric microfluidic actuators*. *Microfluidics and Nanofluidics*, 7(1):75–89, November 2008.
- [10] A. Klingner, J. Buehrle, and F. Mugele. *Capillary bridges in electric fields*. *Langmuir The Acs Journal Of Surfaces And Colloids*, 20:6770–6777, 2004.
- [11] M. Vallet, M. Vallade, and B. Berge. *Limiting phenomena for the spreading of water on polymer films by electrowetting*. *European Physical Journal B*, 11:583–591, 1999.
- [12] T. N. Krupenkin, J. A. Taylor, T. M. Schneider, and S. Yang. *From rolling ball to complete wetting: the dynamic tuning of liquids on nanostructured surfaces*. *Langmuir The Acs Journal Of Surfaces And Colloids*, 20:3824–3827, 2004.

- [13] J.-Y. Yoon and R. L. Garrell. *Preventing biomolecular adsorption in electrowetting-based biofluidic chips*. *Analytical Chemistry*, 75(19):5097–5102, October 2003.
- [14] A. R. Wheeler, H. Moon, C. Kim, J. A. Loo, and R. L. Garrell. *Electrowetting-based microfluidics for analysis of peptides and proteins by matrix-assisted laser desorption / ionization mass spectrometry laser desorption / ionization mass spectrometry*. *Analytical Chemistry*, 76(16):4833–4838, 2004.
- [15] M. Abdelgawad, S. Freire, H. Yang, and A. R. Wheeler. *All-terrain droplet actuation*. *Lab on a Chip*, 8(5):672–677, 2008.
- [16] D. Witters, N. Vergauwe, S. Vermeir, F. Ceyskens, S. Liekens, R. Puers, and J. Lammertyn. *Biofunctionalization of electrowetting-on-dielectric digital microfluidic chips for miniaturized cell-based applications*. *Lab on a Chip*, 11:2790–2794, 2011.
- [17] I. Barbulovic-Nad, H. Yang, P. Park, and A. R. Wheeler. *Digital microfluidics for cell-based assays*. *Lab on a Chip*, 8:519, 2008.
- [18] V. Srinivasan, V. K. Pamula, and R. B. Fair. *An integrated digital microfluidic lab-on-a-chip for clinical diagnostics on human physiological fluids*. *Lab on a Chip*, 4:310–315, 2004.
- [19] N. Vergauwe, D. Witters, Y. T. Atalay, B. Verbruggen, S. Vermeir, F. Ceyskens, R. Puers, and J. Lammertyn. *Controlling droplet size variability of a digital lab-on-a-chip for improved bio-assay performance*. *Microfluidics and Nanofluidics*, 11(1):25–34, January 2011.
- [20] N. Vergauwe, D. Witters, F. Ceyskens, S. Vermeir, B. Verbruggen, R. Puers, and J. Lammertyn. *A versatile electrowetting-based digital microfluidic platform for quantitative homogeneous and heterogeneous bio-assays*. *Journal of Micromechanics and Microengineering*, 21(5):054026, May 2011.
- [21] D. Witters, N. Vergauwe, R. Ameloot, S. Vermeir, D. De Vos, R. Puers, B. Sels, and J. Lammertyn. *Digital microfluidic high-throughput printing of single metal-organic framework crystals*. *Advanced materials*, 24(10):1316–1320, March 2012.
- [22] R. Sista, Z. Hua, P. Thwar, A. Sudarsan, V. Srinivasan, A. Eckhardt, M. Pollack, and V. Pamula. *Development of a digital microfluidic platform for point of care testing*. *Lab on a Chip*, 8(Dec):2091–2104, 2008.

- [23] H. Liu, S. Dharmatilleke, D. K. Maurya, and A. a. O. Tay. *Dielectric materials for electrowetting-on-dielectric actuation*. *Microsystem Technologies*, 16(3):449–460, November 2009.
- [24] Y.-y. Lin, R. D. Evans, E. Welch, B.-n. Hsu, A. C. Madison, and R. B. Fair. *Low voltage electrowetting-on-dielectric platform usign multi-layer insulators*. *Sensors and Actuators B: Chemical*, 150(1):465–470, 2011.
- [25] MATLAB, <http://www.mathworks.com>.
- [26] National Instruments, <http://www.ni.com/>.
- [27] S. K. Selvaraja, P. Jaenen, W. Bogaerts, D. V. Thourhout, P. Dumon, and R. Baets. *Fabrication of photonic wire and crystal circuits in Silicon-on-Insulator using 193nm optical lithography*. *Journal of Lightwave Technology*, 27(18):4076–4083, 2009.
- [28] W. Bogaerts, R. Baets, S. Member, P. Dumon, S. Member, V. Wiaux, S. Beckx, D. Taillaert, B. Luyssaert, and J. V. Campenhout. *Nanophotonic waveguides in Silicon-on-Insulator fabricated with CMOS technology*. *Journal of Lightwave Technology*, 23(1):401–412, 2005.
- [29] K. De Vos, J. Girones, T. Claes, Y. De Koninck, S. Popelka, E. Schacht, R. Baets, and P. Bienstman. *Multiplexed anitbody detection with an array of Silicon-on-Insulator microring resonators*. *IEEE Photonics Journal*, 1(4):225–235, 2009.
- [30] H. Su and X. G. Huang. *Fresnel-reflection-based fiber sensor for on-line measurement of solute concentration in solutions*. *Sensors and Actuators B: Chemical*, 126(2):579–582, October 2007.
- [31] R. Belda, J. Herraiez, and O. Diez. *A study of the refractive index and surface tension synergy of the binary water/ethanol: influence of concentration*. *Physics and Chemistry of Liquids*, 43(1):91–101, 2005.
- [32] K. De Vos, I. Bartolozzi, E. Schacht, P. Bienstman, and R. Baets. *Silicon-on-Insulator microring resonator for sensitive and label-free biosensing*. *Optics Express*, 15(12):7610–7615, June 2007.

5

Reaction tubes as a platform for photonic sensors

In this chapter, we will investigate whether we can integrate photonic biosensors in the standard reaction tubes commonly used in hospitals and labs to perform any kind of bioassays. The goal is to provide a new biosensor device combining the good performance of photonic biosensors and the convenience of the handy format of a reaction tube. In the first section we will explain the motivation for this investigation. Later we will present the device and its key parts: the biosensors, the fluidic system, and how the integration can be performed. At the end of the chapter, we will describe the setup required to carry out the experiments and we will present the results of these experiments. The work in this chapter was published in [1].

5.1 Motivation

In 1963 Eppendorf introduced the first microtube into laboratories and created a standard that to the present day is used in all research and diagnostic laboratories throughout the world. They are essential to perform bioassays which serve as a diagnostic tool in medicine and plant pathology, as well as a quality-control checking in various industries (Figure 5.1).

Those handy and disposable platforms for small fluid volumes have received



Figure 5.1: Microtest tube introduced in laboratories by Eppendorf in 1963. Nowadays this tube is used in all research and diagnostic laboratories throughout the world.

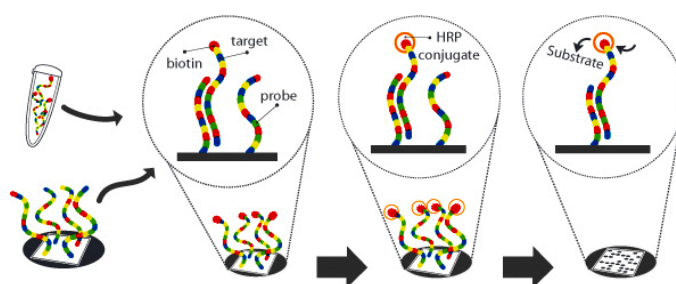


Figure 5.2: Mobidiag assay principle: detection of the result is based on DNA hybridization to capture oligos on the chip. The reaction is visualized by inducing a color reaction in the label [2].

large investments to achieve automatic and efficient handling, optimizing the bioassays' performance. Nowadays all lab instrumentation related to sample-liquid handling, such as centrifugators, mixers, pipette arrays, etc. is compatible with this kind of tube.

However, this platform only allows for labeled detection assay techniques which are labour intensive and costly and can only be performed in an 'end-point' fashion so that no kinetic information on the biomolecular interaction can be obtained.

As discussed in Chapter 2, quantification of the detection is a difficult task in labeled assays. In an attempt to simplify this quantification, Mobidiag [2] has incorporated a microchip at the bottom of a reaction tube where a microarray is defined. The result is based on DNA hybridization to capture oligos on the microarray and the reaction is visualized by inducing a color reaction in the label (Figure 5.2).

Following the same concept but bringing the advantages of label-free technology without giving up the handy and disposable format that Eppendorf introduced in labs more than half a century ago, our goal is to integrate a photonic chip with an array of ring resonator biosensors at the bottom of these re-

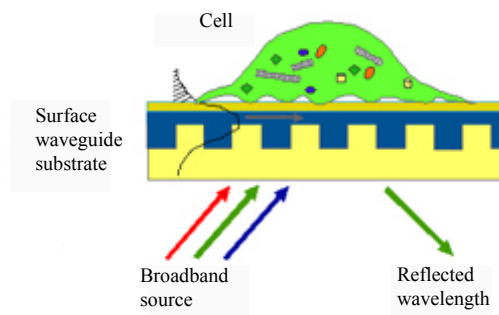


Figure 5.3: The Corning Epic System is based on waveguide grating optical biosensors at the bottom of a microtiter plate. When illuminated with broadband light, the biosensor reflects a specific wavelength of light that is a sensitive function of the index of refraction close to the sensor surface. Binding events on the surface produce a wavelength shift in the reflected light [3].

action tubes. This would enable numerous advantages: on one hand, all the advantages of photonic label-free ring resonators that we mentioned in Chapter 2, i.e. high performance biosensors, disposable chips due to mass fabrication and label-free assays with kinetic information and real time monitoring; on the other hand, all the advantages of the handy, user-friendly, portable and compatible format of the 'eppendorf' tube used by most lab professionals nowadays.

In the common procedure for label assays (Chapter 1), long analysis times must be considered to allow the analyte to reach the receptors by diffusion, and a washing step must be performed every time a new solution is inserted in the tube. In our approach instead, a flow will be created over the sensors' surface, so a combination of convection and diffusion will transport the analyte to the surface of the sensor. The whole process of detection will be faster and more efficient and no washing steps will be required.

A related, but diffusional approach is already made available to the market by Corning Inc. [3]: the Corning Epic System. This product is based on refractive waveguide grating optical biosensors at the bottom of another common format used in labs: microtiter plates. When illuminated with broadband light, the biosensor reflects a specific wavelength of light that is a sensitive function of the index of refraction close to the sensor surface. Binding events or intracellular protein movements in cells cause wavelength shifts in the reflected light that can be measured (Figure 5.3). Bindings of 300Da compounds to 70kDa targets can be detected. However Corning's device still relies on the 'pipette-wait-and-rinse' method of labeled assays.

5.2 The device: photonic ring resonator sensors integrated at the bottom of a reaction tube

In this section we will analyze every part of the device in detail.

5.2.1 Photonic chip and reaction tubes

The photonic chip used for this approach consists of an SOI chip with an array of 20 microring resonator biosensors. The resonators consist of 450-nm wide single-mode waveguides, with 5 μm bend radius, 2 μm long directional couplers and a gap of 180 nm between the waveguides. The configuration of this sensors is the one described in Chapter 4. Four rings are connected to one common input waveguide, each of them having a dedicated drop signal port. Five of these four ring series are placed independently next to the other. The five input waveguides are simultaneously addressed through vertical grating couplers [4] with a 2-mm wide collimated beam from a tunable laser source. The output signals of the ring resonators are near-vertically coupled to free space by means of integrated grating couplers and are imaged with an infrared camera.

Eppendorf® provided the tubes we worked with (Figure 5.1). They are 1.5 ml polypropylene microtest tubes.

5.2.2 Integration

The photonic chip is incorporated at the bottom of the reaction tube, once its original bottom is mechanically removed. The attachment of the chip to the bottom of the tube is done permanently using a UV curable adhesive which allows us to precisely align the array of sensors in the center of the reaction tube. Figure 5.4 shows a picture of the final device.

5.2.3 Embedded microfluidic system

5.2.3.1 Fabrication

Our purpose is to create a flow across the chip surface where the sensors are placed so the analyte to be detected is able to reach the vicinity of the sensor in a fast way. In order to create this flow, different possibilities were studied among which the main idea was to perforate the chip so the fluid introduced in the tube will find its way out, creating at the same time a flow on the surface of the sensors. Figure 5.5 shows a schematic of the device with this fluidic system.

The perforations through the silicon-on-insulator chip can be made in two possible ways. The first route considered was developed in the course of the PhD of Hallynck [5] and served as inspiration to this work. It basically consists

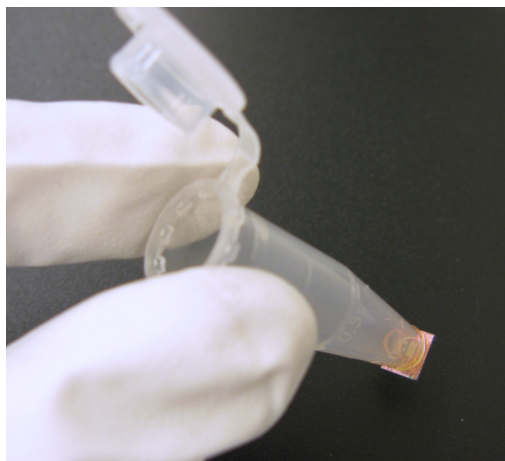


Figure 5.4: The photonic chip is attached at the bottom of the reaction tube using a UV curable adhesive.

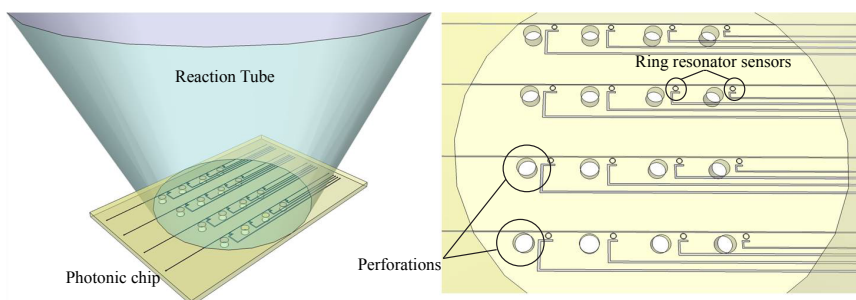


Figure 5.5: a) Schematic of the assembled device. The silicon-on-insulator chip is incorporated at the bottom of a reaction tube. b) Layout of the chip. The array of ring resonators sensors is accompanied by an array of perforations next to them. The flow within the tube is guided through these apertures. The solution inserted in the tube will flow through these openings which work as exit channels. The resulting flow will accelerate the detection process.

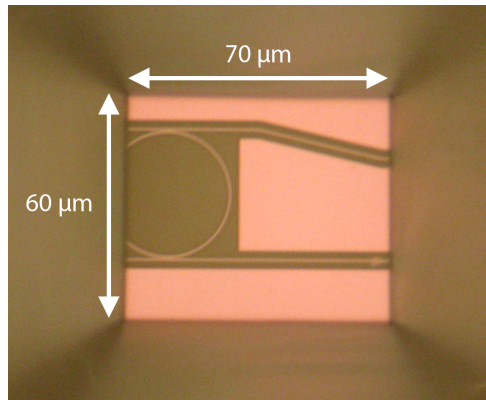


Figure 5.6: Microscope image of part of a silicon ring resonator where the silicon substrate is locally etched away (seen from the substrate side) [5].

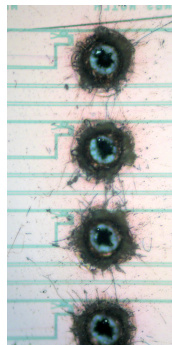


Figure 5.7: Microscope picture of the residues induced by the laser perforation. To avoid damaging the surface of our sensors, the sample was covered earlier with a photoresist, which was afterwards easily removed with acetone in an ultrasonic bath.

of locally removing the silicon substrate and etching the buried oxide to create a silicon membrane. As one can imagine, this fabrication process requires a considerable number of process steps, although the result is accurate and precise, as can be seen in Figure 5.6 where a silicon membrane is still left.

The lack of time to optimize this process for our approach made us explore a more efficient route which was possible thanks to the collaboration of the Centre for Microsystems Technology (CMST) at Ghent University which has a Duetto pulsed laser source from Time-Bandwidth Products AG available. Indeed, silicon can be removed by laser ablation in the form of fine vapor, liquid

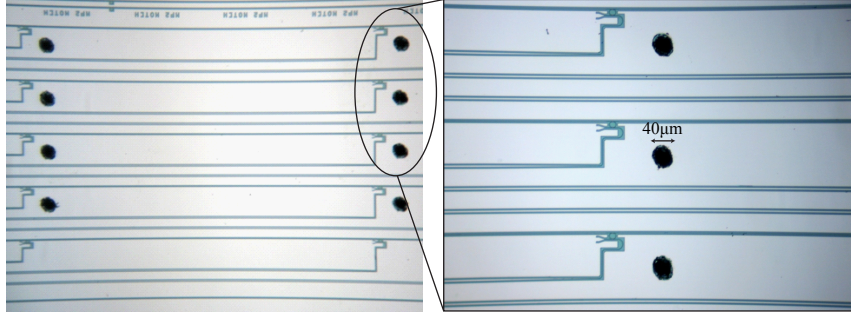


Figure 5.8: Microscope picture of the perforation configuration. Each perforation will create a flow over its closest sensor.

droplets, or solid flakes due to evaporation, hydrodynamic instability, exfoliation, and explosive boiling depending on the laser irradiance [6, 7]. An understanding of the relationship between the quantity and size of the ablated particles versus the laser irradiance is crucial in selecting optimal process parameters. Operating at 355 nm with 1000 ps pulses with a repetition rate of 50 kHz, we managed to perforate an SOI chip with a 200 μm Si substrate. However, some residue remained on the surface. Figure 5.7 shows the result and the effects of the laser on the SOI chip. To avoid damaging the surface of our sensors, the sample was covered earlier with a photoresist, which was afterwards easily removed with acetone in an ultrasonic bath. Figure 5.8 shows the perforations after the cleaning process. The size and position of the openings can be easily optimized by tuning the laser parameters.

5.2.3.2 Simulations

The configuration of perforations on the chip was designed so that each one was creating a flow near its closest sensor. In order to study the conditions for this flow, we performed some basic 2D simulations in COMSOL [8].

We considered a system where an aqueous fluid was driven through a circular channel by imposing a pressure difference between an input and output. In this channel the volumetric flow rate is defined by the Hagen-Poiseuille equation [9]:

$$Q = \frac{\pi r^4}{8\mu} \cdot \frac{dP}{dz} \quad (5.1)$$

where r is the radius of this cross-section, μ is the dynamic viscosity of the fluid and dP the pressure drop along the length dz of the channel. The mean velocity of the flow can then be calculated by:

$$V_{mean} = \frac{Q}{A} = \frac{r^2}{8\mu} \cdot \frac{dP}{dz} \quad (5.2)$$

where A is the area of the cross-section of the channel.

We assume now that we have the geometry illustrated in Figure 5.9. A water-based fluid is introduced in the first part of this geometry (i.e. the reaction tube), with a null-velocity, while a negative pressure is applied at the bottom of the geometry, creating an underpressure that drives the fluid through the different apertures (i.e. the perforations through the SOI chip) towards the exit of the channel. Considering that the fluid introduced in the system is water, with a dynamic viscosity 1.002 mPa-s, the maximum velocity of the flow in the perforations was calculated to be 0.5 m/s when applying a 1kPa pressure difference, which was confirmed by the simulations performed in COMSOL.

The pressure applied on the system not only generates the transport of the fluid from the reaction tube to the exit. When looking in detail into the streamlines in the surroundings of one aperture (Figure 5.10), we discover the presence of vortices. Vortices are a natural effect of turbulent flows that can be also provoked in laminar flows. Normally, in laminar flows the mixing between different species relies heavily on mass diffusion, while when the vortices are generated the mixing performance is enhanced by convection. During the last two decades different methods for the fabrication of micromixers have been reported [10, 11] among which vortex generators stand [12]. We can say that the geometry of our model together with the pressure applied to the system stimulates the generation of vortices in the surroundings of the apertures which confirms that the transportation of the analyte to the surface of our sensors is done through convection. These vortices are stimulated every time that pressure is applied at the bottom of the system, making sure that the fluid on the chip is in continuous movement and delivering the analyte in an efficient way.

In conclusion, the perforations made through the SOI chip establish a flow through the sensors' surface. Depending on the position of these perforations the analyte will be brought to the sensor's surface by the main stream, which goes directly to the perforation and its very close vicinity, or by the vortices, a bit further from these perforations. In any of these cases the analyte will be transported in a fast and efficient way through a combination of convection and diffusion.

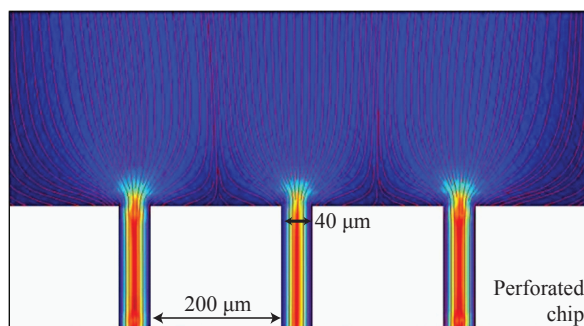


Figure 5.9: Simulation of a water-based fluid flow in our device configuration. Streamlines in red confirm us the existence of a flow across the apertures and its vicinity.

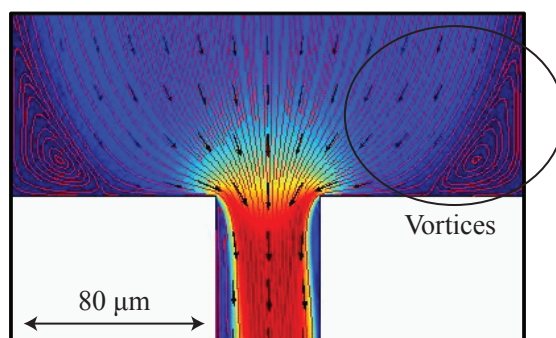


Figure 5.10: Simulation detail of one of the apertures. Streamlines in red indicate the presence of vorticity flow near the aperture.

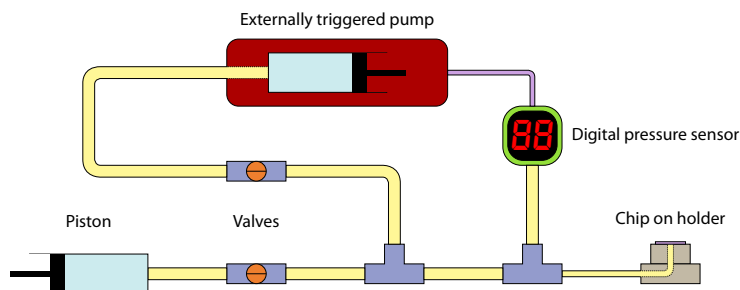


Figure 5.11: The initial pressure difference is achieved by means of a piston. Due to imperfections in the setup or chuck, the pressure difference will decrease over time. By adding a feedback loop between the pump and the digital pressure sensor, the desired pressure level can be maintained [5].

5.3 Experiments

5.3.1 Setup

To perform the experiments, the device was fixed on a tiny vacuum chuck with a connection to a pump, where pressure can be applied roughly by a piston after which it can be fine-tuned using a syringe in a NE 1000 syringe pump [13]. Using a SUNX DP-101 digital pressure sensor [14], we were able to monitor the applied pressure difference with an accuracy of 1 kPa. Due to imperfections in the chip substrate and the pressure circuit, small leaks can occur which will cause the pressure difference to drop over time. To compensate for this, we can use the built-in comparator of the DP-101: when the pressure difference drops below a certain set value, a digital output signal of the sensor changes value. Since the NE 1000 has the capability of being externally triggered, we can use the digital output signal of the pressure sensor as a trigger for the pump. The resulting feedback loop ensures that the pressure level remains fixed over time with an accuracy of about 1 kPa. This pressure setup was developed by Hallynck during his PhD work [5]. The entire pressure setup is illustrated in Figure 5.11.

This setup allows us to apply positive or negative pressure, pushing or sucking any gas of fluid applied in a specific area of the chuck. The reaction tube with the photonic chip integrated at its bottom was carefully aligned, so the perforations of the chip coincide with this area. Any fluid in contact with the chip will flow through the holes and be sucked down and/or pushed up again by the pump. Figure 5.12 shows the device fixed on this chuck.

As in Chapter 3, grating couplers were used to couple the light from a tunable laser into the chip and couple it out again to be detected by an infrared

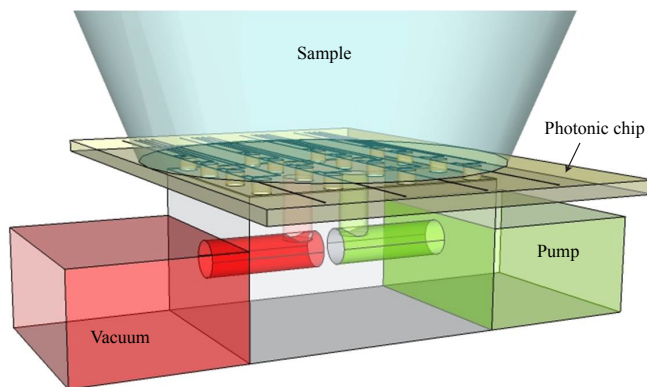


Figure 5.12: Device mounted on a vacuum chuck with an additional pump to move the fluid across the chip surface. The detail of this pump is illustrated in Figure 5.11.

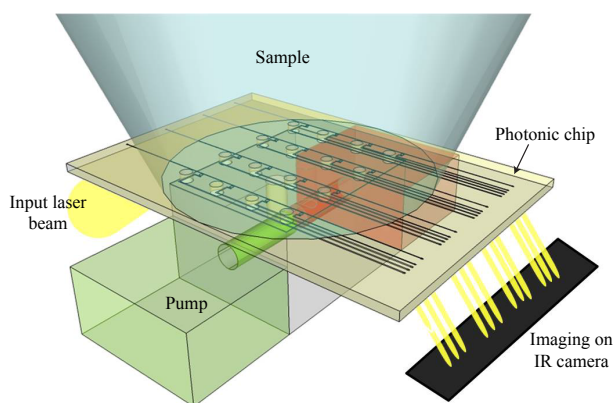


Figure 5.13: Device mounted on a vacuum chuck, while measurements are being performed from the bottom of the chip. Light is coupled in and out from underneath, through the chip substrate.

camera. Here again we couple light in and out from the bottom of the chip through the 200- μm thick silicon substrate, as shown in Figure 5.13.

Silicon features high transparency at the wavelength used (1.55 μm). However, to reduce the scattering from the rough substrate surface and to facilitate both the alignment of the laser beam and the detection of the light coupled out from the chip, the silicon substrate was thinned down to 300 μm and planarized by chemical-mechanical lapping (CML) and polishing (CMP) in order to attain a smooth surface.

5.3.2 Results

As a proof-of-principle and in order to show the capabilities of the combined device, we measured the response of the device when aqueous solutions with different sodium chloride concentrations were flown through the device. Small volumes of different solutions were manually pipetted into the tube, and they were sucked out through the perforations on the bottom of the tube while being measured. The change of refractive index in those solutions causes the shifts in wavelength observed in Figure 5.14.

When analyzing these shifts as a function of the refractive index unit (RIU) the sensitivity measured for these biosensors is 78.8 nm/RIU which corresponds once more with the measurements performed and proved in our previous work [15], where these sensors were also used. This confirms that the transducer does not suffer any degradation when being integrated into the device.

Additionally, different steps of the high-affinity couple biotin-streptavidin assay were measured. The actual surface chemistry used in this experiment was far from optimized, but this does in no way detract from the main point of this work, which is about showing the working principle of the new combined device. The experiment consisted of the following three individual steps:

1. Silanization of the surface: a 2% aminosilane solution of (3-Aminopropyl) triethoxysilane (APTES) was flown, both preceded and followed by rinsing with ethanol.
2. Immobilization of biotin: a solution 3 mg/ml of biotin in phosphate buffered saline (PBS) was flown, both preceded and followed by rinsing with PBS pH 7.
3. Binding of streptavidin: a solution of 0.1 mg/ml streptavidin in PBS was flown, both preceded and followed by rinsing with PBS pH 7.

Here again, all the volumes were manually pipetted into the tube, and they were sucked out through the perforations at the bottom of the tube while being measured. The time to perform each of these steps was less than one hour.

Figure 5.15 shows three different graphs corresponding to each one of the steps of the assay. They show the evolution in time of the resonance wavelength

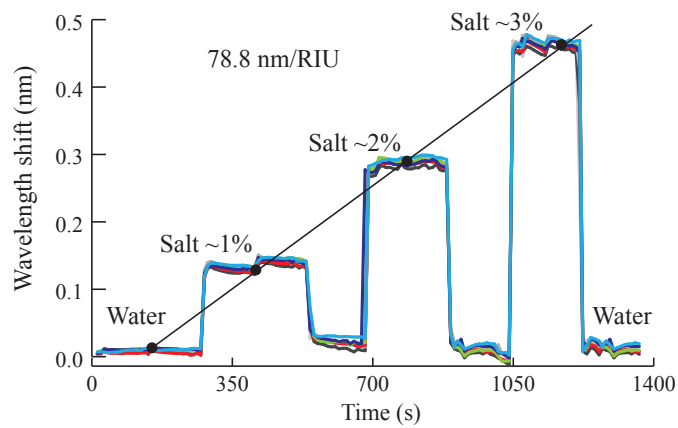


Figure 5.14: Evolution in time of the resonance wavelength shift of the ring resonators during the measurements of different sodium chloride concentrations. Each color corresponds to one sensor. The shift of the resonance wavelength is easily measurable when changing from water to salt solution and vice versa. The sensitivity measured for these sensors is 78.8 nm/RIU, which confirms that the transducer does not suffer any degradation when being integrated into the device. Small variations of the signal can be observed in different points of the graph, specifically in the measurement of salt 1% and 3%. This is the effect of the introduction of extra solution in the reaction tube during the measurements.

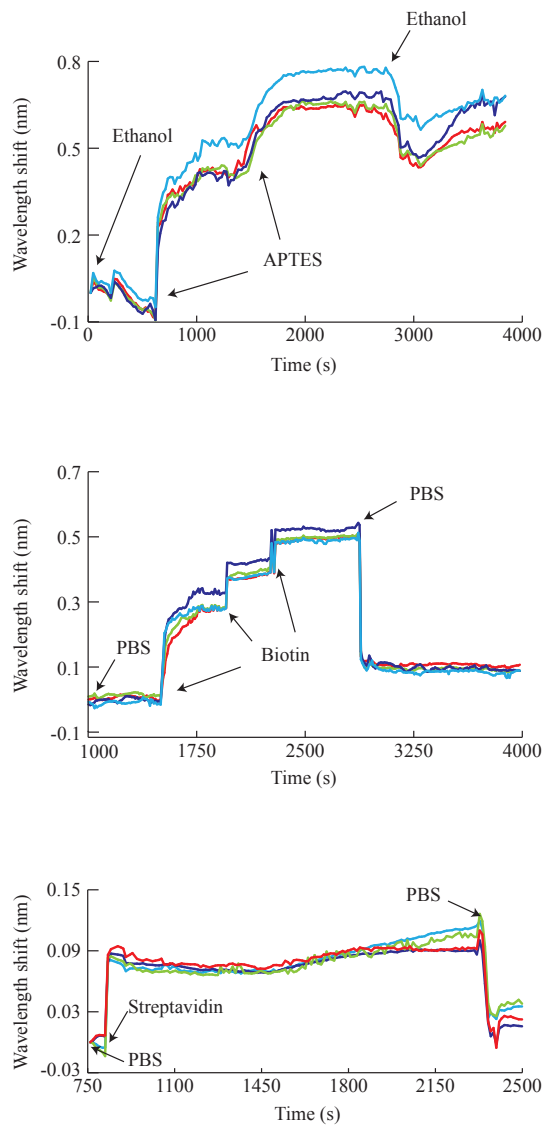


Figure 5.15: Three different steps of the bioassay were measured: a) Silanization of the surface with APTES (ethanol - APTES - ethanol); b) Immobilization of the biotin (PBS - biotin - PBS); c) Binding of streptavidin to biotin (PBS - streptavidin - PBS).

shift of the ring resonators during the measurements with different solutions. Each color corresponds to one sensor. The association and disassociation of APTES in the sensor is easily quantifiable in Figure 5.15a. Figure 5.15b shows the binding of biotin after flowing 3 mg/ml solution of biotin in PBS and its disassociation when it is rinsed with PBS. In these two graphs, some intermediate discrete bulk shifts can be observed during the flow of APTES and biotin, which were provoked by the injection of new solution in the reaction tubes. In Figure 5.15c a shift of 30 pm is measured when streptavidin is flown through the chip indicating the binding of this to biotin.

5.4 Conclusions

We have presented a new platform for silicon photonic ring resonators: reaction tubes.

We have combined the simplicity and portability of the reaction tube format with the performance and throughput of silicon photonic ring resonator biosensors by embodying them in a single flow-through device. An embedded microfluidic system based on perforations of the SOI chip attached to the tube provides an alternative to the typically costly and complex microfluidic system based on microchannels. The disposability of the combined device is enhanced by the mass fabrication of SOI chips and the cheap and user friendly format of reaction tubes which are used every day in labs and hospitals, two factors that benefit their use for performing label-free bioassays. We have proved no degradation of the sensors by bulk sensing experiments and the good performance of the device by showing the binding of streptavidin to avidin on the surface of the sensors.

The device allows for real-time detection and analysis. Its portability and disposability make it ideal for easy and fast use in any laboratory.

References

- [1] C. Lerma Arce, S. Van Put, A. Goes, E. Hallynck, K. Komorowska, and P. Bienstman. *Reaktionsgefäße als neue Plattform für Sensoren mit nanophotonischen Silizium-Ringresonatoren*. *BioPhotonik*, 6(2):40–42, 2013.
- [2] Mobidiag, <http://www.mobidiag.com/default.aspx>.
- [3] Corning, <http://www.corning.com/lifesciences>.
- [4] W. Bogaerts, R. Baets, S. Member, P. Dumon, S. Member, V. Wiaux, S. Beckx, D. Taillaert, B. Luyssaert, and J. V. Campenhout. *Nanophotonic waveguides in Silicon-on-Insulator fabricated with CMOS technology*. *Journal of Light-wave Technology*, 23(1):401–412, 2005.
- [5] E. Hallynck. *Applications of integrated photonic structures on membranes fabricated by locally etching the silicon substrate*. Phd dissertation, Ghent University, 2013.
- [6] M. Von Allmen. *Laser Beam Interactions with Materials*. Springer, Heidelberg, 1987.
- [7] J. C. Miller and R. F. Haglund. *Laser Ablation Mechanisms and Applications*. Springer, Heidelberg, 1991.
- [8] COMSOL, <http://www.comsol.com/>.
- [9] H. Bruus. *Theoretical Microfluidics*. Oxford University Press, 2008.
- [10] V. Hessel, H. Löwe, and E. Schönfeld. *Micromixers - a review on passive and active mixing principles*. *Chemical Engineering Science*, 60(8-9):2479–2501, April 2005.
- [11] L. Capretto, W. Cheng, M. Hill, and X. Zhang. *Micromixing within microfluidic devices*. Springer, topics in edition, 2011.
- [12] K.-Y. Hsiao, C.-Y. Wu, and Y.-T. Huang. *Fluid mixing in a microchannel with longitudinal vortex generators*. *Chemical Engineering Journal*, 235:27–36, January 2014.
- [13] New Era Pump Systems Inc., <http://www.syringepump.com/>.
- [14] SUNX, <http://www.panasonic.com/>.
- [15] K. De Vos, I. Bartolozzi, E. Schacht, P. Bienstman, and R. Baets. *Silicon-on-Insulator microring resonator for sensitive and label-free biosensing*. *Optics Express*, 15(12):7610–7615, June 2007.

6

Conclusions and perspectives

6.1 Conclusions

Nowadays, biosensor technology platforms must meet certain requirements: on one hand, they must be user-friendly, portable and low cost. Sample preparation must be minimized and the sample analysis fast. On the other hand, they must offer exceptional LOD with high specificity, quantitative and multiplexed measurements and high throughput.

One step closer to meet these requirements is achieved by label-free biosensing (Chapter 1) which requires almost no sample preparation and simplifies the assay, reducing costs. In Chapter 2 we gave a broad overview on the most relevant label-free biosensing technologies, and highlighted the promising SOI ring resonators for highly-multiplexed and high-throughput biosensing. The fact that they can be mass-produced in a cost-effective way enhances their disposability which is also beneficial for such a platform.

Also important in this content are the so-called 'lab-on-a-chip' devices, which integrate the transducer, in our case ring resonators, in a user-friendly platform where the delivery of the sample to the surface of the sensor is done in a very efficient and almost automated manner that reduces the need for often expensive laboratory equipment that performs simple sample preparation tasks. Smaller sample requirement, reduced reagent consumption and decreased analysis time are extra advantages of these miniaturized devices that

are normally low cost and offer a portable format.

In the course of this PhD work, we have proposed three novel integrated platforms for such lab-on-a-chip devices:

Fiber probe Many applications require performing measurements in remote locations that are hard to reach. For these cases a similar concept has been created, lab-on-fiber. Optical fiber technology constitutes a valuable platform that can enable the implementation of complex multifunction sensing systems with all the advantages of miniaturization, lightweight, cost-effectiveness, robustness, portability, flexibility and low power consumption. We have made use of this platform to integrate an SOI ring resonator sensor on the facet of a single-mode optical fiber. In this implementation the integrated SOI circuit is transferred to the facet by detaching it from the substrate of the SOI chip. The fabrication of the device has been described in detail in Chapter 3. We have characterized the device by bulk sensing experiments, which have shown no degradation when comparing to the same sensor on an SOI chip, i.e. not integrated on the fiber tip.

Digital microfluidic platform A lot of effort is being spent to implement lab-on-a-chip devices in small and easy-to-use cartridges and new emerging microfluidic technologies are being developed and competing against the well-established microchannel technology. This is the case for digital microfluidics which is able to perform all the fluidic lab-on-a-chip operations (dispensing, transport, mixing, splitting, merging, storing,...) on micro-sized droplets in a single platform without contamination. In Chapter 4 we have presented the combination of this promising technology with the well-known label-free SOI ring resonator sensors, providing an alternative to the typically costly and complex microfluidic system based on microchannels used for liquid sample delivery to microring resonators.

We have proved the excellent performance and compatibility of this combined system, showing no degradation of the sensor performance with respect to simulations or previous measurements of the same sensors using the typical, more complex microfluidic system. This combination allows for multiplexed real-time detection and analysis. Its great flexibility, portability and disposability make it ideal for easy and fast use in any laboratory.

Reaction tubes platform A final device is presented in Chapter 5 as the integration of ring resonators photonic sensors with reaction tubes. Reaction tubes are commonly used in hospitals and labs to perform labeled bioas-

says. We have proposed this platform which is compatible with all lab instrumentation related to automated sample-liquid handling, to perform label-free bioassays with the help of our ring resonator photonic sensors.

We have combined the simplicity and portability of the reaction tube format with the performance and throughput of silicon photonic ring resonator biosensors by embodying them in a single flow-through device. An embedded microfluidic system based on perforations of the SOI chip attached to the tube provides an alternative to the typically costly and complex microfluidic system based on microchannels. The disposability of the combined device is enhanced by the mass fabrication of SOI chips and the cheap and user friendly format of reaction tubes which are used every day in labs and hospitals, two factors that benefit their use for performing label-free bioassays. We have shown no degradation of the sensors by bulk sensing experiments and the good performance of the device by showing the binding of streptavidin to avidin on the surface of the sensors.

6.2 Perspectives

Most of the biosensing experiments in this work were a proof-of-principle, meaning that there exists some room for improvement. First and foremost, the biosensors should be characterized using appropriate surface chemistry with low-concentration analytes. Only then the potential of the proposed devices can be completely discovered.

Temperatures drifts were monitored by reference sensors in the case where we had an array of sensors (digital microfluidic platform and reaction tube platform). However, in the fiber probe case, only one ring resonator is exposed to the sensing area, which makes us unable to monitor temperature drifts. In future generations, a more appropriate design must be able to fit at least another ring resonator on the fiber tip, or measurements must be done using two fibers, one as a sensor and one as a reference.

In the case of the digital microfluidic platform, measurements can be optimized by making use of the automated dispensing feature that the platform can offer, however at the moment of the measurements, this was not possible since an optimization of the microfluidic chip was required. Future versions can enable automatic dispensing and mixing in order to optimize the experiments. The biofunctionalization of the SOI chip could pave the way for a novel integrated platform for diagnostics and life sciences in general in a multiplexed high-throughput context.

Also in the reaction tube device offers room for a lot of improvement. Start-

ing from the optimization of the integration itself, the fabrication, measurements and design of the fluidic perforations. The perforations made by laser ablation are not completely uniform and perhaps another more elaborate method could define them in a more precise manner. The pump parameters used to transport the droplet in this work are the result of a short optimization process and could be further improved.

The SOI ring resonators used as transducers of all three devices can be also optimized. During this PhD work, the design of single rings has been optimized in our group and Tom Claes proved that the Vernier configuration of ring resonators shows a significant improvement in sensitivity and LOD of the sensors. Future generations could be implemented using these optimized designs and/or configurations.

